UNIVERSIDADE DE LISBOA
FACULDADE DE CIÊNCIAS
DEPARTAMENTO DE FÍSICA

Blinking Lights in Taurus:
Long-term Variability of Young Stars and Brown Dwarfs

Afonso Manuel Ribeiro Guerreiro do Brito do Vale

Mestrado em Física
Área de Especialização em Astrofísica e Cosmologia

Dissertação orientada por:
Koraljka Muzic
Karolina Kubiak

2021

Abstract

Young stellar and substellar objects are known to change their apparent brightness in an irregular way. By studying this variability from the optical to mid infrared it is possible to uncover information on the underlying physics. Several effects are imprinted in the light curves, from change of extinction, spot activity and accretion phenomena. The Taurus star forming region is one of the closest star forming regions to the Solar System, containing a rich population of newly formed stellar and substellar sources. We present an analysis of long-term variability for a set of 491 spectroscopically confirmed young sources in Taurus. We use multi-epoch photometry optical data from the Zwicky Transient Facility (ZTF) and mid-infrared data from AllWISE survey. Using various variability indices, we selected 304 (79%) optical variables based on ZTF data and 279 (62%) mid-infrared variables from AllWISE. In the optical data we visually classify the light curves and find that most present visual bursts. To infer the possible origins of variability, we study the trajectories of the sources in color-magnitude diagrams and determine their properties. By comparison with the properties obtained from simple toy models, we can explain much of the observed variability as being due to accretion, hot spots, as well as changes in the amount of extinction. Using AllWISE data we also find that the observed variability causes changes in the determination of the YSO class and observe that 80 sources (32%) experience a change in class. This means that the number of sources in a particular class can change over time due to their variability, which can impact important physical parameters such as the star formation rate, or studies of the protoplanetary disk evolution with time.

Keywords: Stars: variables: T Tauri; Stars: low-mass; Stars: pre-main sequence

Resumo

Apresentamos um estudo da variabilidade de longa duração dos membros da região de formação estelar do Touro. Escolhemos esta região dado ser uma das regiões de formação estelar mais próximas ($\sim$ 140pc) e jovens ($\sim$ 3Myr) na vizinhança do sistema solar. Criámos um catálogo de 491 estrelas que foram confirmadas espectroscopicamente como membros jovens da região do Touro. Usando dados do Gaia eDR3 pudemos observar que os membros escolhidos poderão ter propriedades cinemáticas distintas, consistentes com a possibilidade the várias populações diferentes de estrelas jovens nas nuvens da região do Touro. Descobrimos também que os membros escolhidos têm diferentes classificações no General Catalog of Variable Stars, desde variáveis irregulares a variáveis periódicas.

Usando o catálogo de membros, colecionámos fotometria multi-temporal no ótico, bandas g e r, pela 6ª Data Release da Zwicky Transient Facility (ZTF) e no infravermelho médio (MIR) (bandas W1 e W2) pelo survey AllWISE. O ZTF fornece dados a cada 1-3 dias e o survey publico que usamos tem dados fotométricos desde aproximadamente 2018 até 2020 e continua atualmente a adicionar mais medições ao catalogo. O survey AllWISE fornece dados com cadência de algumas horas ao longo de dois dias separados por 6 meses. O primeiro dia de dados é referente ao período original de medições do survey WISE (Wide-Field Infrared Survey Explorer) e o segundo dia de observações é referente à fase em que o sistema de arrefecimento do satélite deixou de funcionar e o instrumento passou a ter uma performance pior, mas ainda assim cientificamente robusta. Infelizmente os dados dos diferentes surveys não têm sobreposição e como tal a sua análise é realizada separadamente. Estudámos a forma das curvas de luz no ótico e repáramos em alguns padrões emergentes, como tal, dividimos as curvas de luz em quatro classes observacionais: burst visual (VB) (239), dip visual (VD) (139), quasi-periódico (5) e longa-duração (11). A classificação VB é aplicada se a curva de luz exibir um aumento do brilho com um posterior retorno ao valor média de brilho. A classificação VD é aplicada se a curva de luz exibir uma diminuição do brilho com um posterior retorno ao valor média de brilho. A classificação quasi-periódico é aplicada se, localmente na curva de luz, a estrela exibir um fenómeno quasi-sinusoidal. Finalmente a classificação de longa-duração é aplicada se for observado ou um aumento gradual do brilho ao longo da curva de luz ou uma diminuição também gradual do brilho ao longo da curva de luz. Algumas curvas de luz não permitem uma classificação devido a variações muito rápidas da luz ou porque o conjunto de possíveis origens das variações pode afetar a estrela **simultaneamente**, criando padrões extremamente irregulares nas curvas de luz. Para as curvas de luz no MIR observámos quantas estrelas exibem saltos no brilho maiores que 0.5 mag nas bandas W1 (7) e W2 (4), do conjunto de dados pre-cryo para post-cryo (separação temporal de 6 meses).

De forma a descobrir o conjunto de estrelas variáveis nos dados no ótico e no MIR, aplicamos um conjunto de 5 indices estatísticos para a deteção de variabilidade nas curvas de luz obtidas. Para fotometria em cada uma das bandas disponíveis usamos χ^2_{red}, σ_w, A_{burst}, A_{dip} e o Stetson J e para o conjunto de duas bandas em cada survey usamos o WSI. A aplicação de cada um destes indices nas curvas de luz resulta em diferentes determinações do número de variáveis. Isto é devido a limitações na aplicabilidade e sensitividade dos diferentes indices e também às

propriedades dos dados em si. Como tal, combinámos os resultados de cada indice criando 3 regras para a seleção de variáveis:

- Todos os membros selecionados pelo indice WSI são selecionados como variáveis.
- Todos os membros não selecionados pelo indice WSI, se selecionados por 5 dos 10 indices disponíveis, são também selecionados como variáveis.
- Todos os membros com dados em apenas uma das bandas, em cada survey, se selecionados por 3 dos 5 indices disponíveis, são selecionados como variáveis.

Ao fim e ao cabo, selecionámos 304 (79%) variáveis no ótico e 279 (62%) variáveis no MIR; 188 variáveis são selecionadas em ambos os conjuntos. Estudando cada um dos conjuntos de variáveis verificamos que nenhum apresenta preferencia por intervalos de brilho ou tipo espectral.

Primeiro estudamos as possíveis amplitude de brilho e cor nas bandas disponíveis e descobrimos que é esperado que as principais origens para a variabilidade observada nos nossos dados sejam devido a *hot spots*, *cold spots*, variações no valor da extinção e também variações na taxa de acreção, caso um disco protoplanetário esteja presente. Estudando as variações da cor g-r e W1-W2 descobrimos que *cold spots* não podem ser a principal origem para a variabilidade que observamos quer nas curvas de luz no ótico quer nas curvas de luz no MIR. De seguida tentamos inferir a possível origem primária para a variabilidade observada através do seu brilho, cor, classificação de YSO e através de como estes se correlacionam entre si.

Utilizando as 4 bandas disponíveis nos dados pre-cryo do survey AllWISE determinamos as classes de YSO, como definidas em Teixeira et al. (2012). Obtemos 42 YSO classe III (*naked photosphere* no original), 68 YSO com discos evoluídos (*Aneamic Disk* no original), 167 YSO com discos espessos (Thick Disk no original), 25 YSO de espectro plano (Flat Spectrum no original) e finalmente 5 YSO Class I. De seguida, estudamos as possíveis mudanças na determinação da classe de YSO e descobrimos que 80 (32%) das estrelas mudam de classe ao longo da duração das curvas de luz do survey AllWISE. Concluímos que estas variações devem ser atribuídas primariamente a variações no valor da extinção ou ainda fenómenos relacionados com o disco de acreção, dado que a nossa análise das variações de cor demonstra que *cold spots* não devem ser a origem primária para nenhum dos sets de dados (ZTF ou AllWISE) e porque variações devido a hot spots não devem ser detetáveis no MIR.

Verificamos também que as mudanças de brilho induzem mudanças na cor, que podem ser mapeadas num diagrama de cor-magnitude (CMD). Examinando as trajetórias em CMD aplicamos um método de regressão linear baseado em quadrados mínimos de modo obter o declive destas trajetórias. Comparando os declives obtidos com os declives esperados, baseados em modelos teóricos simples, observamos que a grande maioria dos membros do Touro exibem declives menores que o esperado para uma origem em mudanças de extinção quer nos dados do ZTF quer nos dados do AllWISE. Utilizando as classificações de YSO para separar membros do Touro com e sem discos de acreção, descobrimos que 154 destes membros devem ter uma origem de variabilidade em *hot spots* e *acreção variável*, 16 apenas em *hot spots* e 32 são consistentes com variações devido a mudanças no valor da extinção.

Sumarizando, neste trabalho analisámos as variações do brilho dos membros da região de formação estelar do Touro quer no ótico quer no infravermelho médio. Observámos que a grande maioria dos membros são identificados como variáveis em ambos os sets de dados.

Vimos que no ótico as curvas de luz apresentam padrões emergentes e que bursts visuais são os mais comuns do conjunto. Estudando as possíveis origens para a variabilidade estelar destas estrelas, observamos que a maioria deve estar relacionada com *hot spots*, mudanças no valor da extinção ou acreção. Destas possíveis origens, ao estudar o mapeamento das trajetórias em CMDs observamos que a maior parte dos membros do Touro, dado estarem associados com discos de acreção, devem ter uma origem na sua variabilidade primariamente devido a *hot spots* e acreção.

Palavras-Chave: Estrelas: variáveis: T Tauri; Estrelas: pequena massa; Estrelas: jovens

Para a minha avó, Maria Gertrudes Cruz Ribeiro Guerreiro, a estrela mais cintilante que alguma vez pude observar

Acknowledgments

Quero agradecer em primeiro lugar à minha mãe, Cláudia Cristina Ribeiro Guerreiro do Brito do Vale, porque ela o merece. Depois ao resto da minha família: o meu irmão Guilherme, o meu pai Joaquim, o meu avô Manel e o meu cão Doby.

Em segundo lugar quero deixar um especial agradecimento a ambas as minhas coordenadoras, Koraljka Muzic e Karolina Kubiak. Não seria possível eu sequer ponderar fazer um trabalho desta magnitude sem a vossa contínua atenção e ajuda e estou-vos eternamente agradecido pela oportunidade de trabalhar neste tema ao longo do último ano e meio.

Por fim quero agradecer a todos os meus amigos que me ajudaram durante todo o último ano. Eles sabem quem são inumerá-los seria redundante.

Por fim quero também agradecer a todos os membros do grupo de investigação que me acompanhou no último ano, YoBD.

Contents

List of Figures

List of Tables

Abbreviations

δ Cep - Delta Cephei
A_{burst} - Burst Amplitude
A_{dip} - Dip Amplitude
AD - Anno Domini
AGB - Asymptotic Giant Branch
ALMA - Atacama Large Milimiter Array
BC - Before Christ
BD - Brown Dwarfs
CMD - Color-Magnitude Diagram
Gaia DR2 - Gaia Data Release 2
Gaia eDR3 - Gaia Early Data Release 3
GCVS - General Catalog of Variable Stars
GMC - Giant Molecular Cloud
HRD - Hertzsprung–Russell Diagram
IMF - Initial Mass Function
ISM - Interstellar Medium
IRSA - Infrared Science Archive
MEP - AllWISE Multiepoch Photometry Database
MJD - Modified Julian Date
MS - Main Sequence
MIR - Mid Infrared
NIR - Near Infrared
NEO - Near Earth Objects
PMS - Pre-Main-Sequence
PTF - Palomar Transient Factory
RA - Right Ascension
SED - Spectral Energy Distribution
SFR - Star Formation Rate
Taurus SFR - Taurus Star Forming Region
VB - Visual Burst
VD - Visual Dip
WISE - Wide-field Infrared Survey Explorer
WSI - Welch-Stetson I
YSO - Young Stellar Object
ZTF - Zwicky Transient Facility
ZTF DR6 - ZTF Data Release 6

Chapter 1

Historical Background

Astronomy is one of the oldest sciences that we have record of. During its first early stages, contributing to it was as simple as observing the bright sources in the sky and taking records of their positions and apparent movement. This is what we now call astrometry, a scientific field related to astronomy which deals with precise measurements of the positions and motions of celestial bodies. In these early times, however, precise measurements were very difficult and much was done intuitively by simply observing the stars night after night with only the aid of a skilled human eye. If we define astronomy as the qualitative pursuit of understanding the constituents of the cosmos and their evolution, then it follows that related fields of study such as astrometry came into being in order to help fill the absence of astronomical knowledge; i.e. even though one could not know by instinct what a bright source exactly was, knowing its position and/or motions would provide a sense of safety. Another important field of study in these early times, not of scientific nature, was astrology. Astrology also helped fill the ignorance felt by ancient civilizations, mainly by imposing beliefs with roots in mythology and religion into the celestial bodies observed and astronomical events experienced. Because of this, most of the astronomers, which were astrologist at this time, studied the apparent motions of the brightest celestial bodies such as the Sun, the Moon, planets, and comets against the fixed sources in the sky plane. In astrology the fixed sources were grouped in constellations, which denoted mythological figures and also helped astrologists refer to specific celestial bodies more easily. Even though these astrometric exercises had some scientific merit, there was an important advancement made when people started trying to classify the bright sources of light that filled the night sky according to something more than fictional figures. The first efforts to do so started by researching their most obvious trait: brightness (or better yet their apparent brightness, which is the brightness of a source as seen from Earth).

Astronomers of old used their naked eyes to classify the apparent brightness of sources in the sky. One of the first people thought to have started classifying stars into different numerical "classes" was Manilius , which was an ancient Roman poet from the first century AD (Cunningham, 2020). Manilius wrote a didactic poem of astrological nature, called *Astronomica*, in which he describes a system of six different classes where he would group stars according to their apparent brightness. Earlier than Manilius, around 135 BC, Hipparchus had created a catalog of astronomical sources in which he devised a simpler method to categorize stars. In his catalog Hipparchus looked at the stars in each constellation and classified all the sources relative to the brightest one; he used three different classes to do this which vaguely translate to bright, dimmer and faint (Cunningham, 2020). The work of Manilius thus improves upon his predecessors since he actually devised a more mathematical approach to the problem of classifying stars than Hipparcus. These numerical classes were called *forma* in the original text in Latin and Manilius explains that the brightest stars belong to the first *forma* and the faintest to the 6th. In a passage of Astronomica, Manilius even goes further and says that the class with the most stars in it is the lowest order one (6th); additionally he also provides an interesting departure from the classical astrology of his contemporaries as Manilius writes that it is the stars which influence human life, not the planets (having even said that they hold the secret of how much time we have to live; Cunningham 2020). *Astronomica* stands as an interesting early accomplishment for proto-astronomy, so to speak. Not only does its author write on the many wonders of the cosmos and celestial bodies which permeate it, but he also engages in the proto-scientific endeavor of trying to classify such celestial bodies in 6 classes based on their brightness, which was not yet a mathematical concept at the time. Following Manilius, Ptolemy [1] was also able to devise a similar numerical system, now with 8 different classes, and use it to improve upon the star catalog created by his ancestor Hipparchus almost three centuries before. It is impossible to know whether Ptolemy could have been influenced by the work of Manilius, specially because there is no direct reference to it in his works, however it also seems unlikely given the astronomical nature of the subjects discussed in *Astronomica*. Regardless, Ptolemy improved upon the semi-scientific poetry of Manilius, mainly by introducing 2 more classes: one to denote nebulae and another to refer to dark stars, which were stars that could not be seen but he was sure were there in the sky. Ptolemy also created a very important nomenclature in his work, *megethos*, which he used to refer to stellar brightness. When translated from Greek to Latin it becomes, *magnitudo*, which is much more similar to its modern English form, magnitude.

The reason why astrophysicists use a logarithmic scale called magnitudes to classify the brightness of astrophysical sources arises from these early astronomers. Because of them, the 6 class method of classifying stars and the term *megethos*, then *magnitudo*, then magnitude dispersed through the community of astronomers that succeeded them. When photometric measurements became possible, even before photographic plates, astronomers were able to discover that a magnitude 1 source was roughly 100 times brighter than a source of magnitude 6! This was achieved by using an artificial light to mimic an astrophysical source through the lens of a telescope. It was only in 1856 that the modern definition of magnitude as we know it was defined by Norman Pogson (Pogson, 1856):

$$m - m_{ref} = -2.5 \log_{10} \left(\frac{F}{F_{ref}} \right) \tag{1.1}$$

Pogson created this definition to pay homage to these early astronomers. He did this by incorporating into his modern definition that a 5 magnitude difference would equate to a change in brightness of about a factor of 100. Nowadays, we are so used to the magnitude system and its formal definition that it may seem strange that there was a point in time when the physics behind the tides and the motions of the planets orbiting the Sun were known but astronomers simply looked to the sky and "guessed" the magnitude of a bright source with simply their eyesight. Interestingly, one thing that Pogson was well aware of while devising the modern magnitude scale that Manilius probably never thought of, was that this sort of classification was not straightforward for all sources in the sky. In fact, it was possible for a source to change its brightness over time, be it in an orderly way or in a rather chaotic fashion: **these are variable sources.**

---

[1] Cunningham 2020; more info: https://en.wikipedia.org/wiki/Ptolemy

1.1 The Discovery of Variable Sources

It is difficult to know exactly which was the first variable source to be discovered. Very likely, nova and supernova events were observed by very ancient civilizations, given that they are very easy to detect with the naked eye due to their peak brightness being close to a star or galaxy, respectively. A nova is an event triggered by the fall of gas from a star into its companion white dwarf, which is the core left by a star with less than $\sim 8\ M_\odot$ due to its outer layers having been ejected at the end of its evolutionary sequence. A supernovae can happen when the white dwarf in the previous example exceeds the Chandrasekhar limit ($\sim$1.44 $M_\odot$ through accretion; Chandrasekhar 1931), for example, but it can also happen due to core collapse of massive stars - stars with masses exceeding 8 $M_\odot$. Some circumstantial evidence suggests that ancient Indian, Chinese and Roman communities could have witnessed and recorded some of these events.
In a survey of pretelescopic astronomical records from Europe, China, Korea, Japan, Babylon, and the Arab countries, Clark and Stephenson (1982) found records on the sightings of about 7 supernova events; these sightings range from the year 185 AD to 1604 AD and were mostly confined by oriental observations. SN1054 is one of these supernova and was observed in 1054 AD by Arab and Chinese astronomers (Clark and Stephenson, 1982); it spawned a nebula now known as the Crab Nebula (see Figure 1.1), which is a supernova remnant, a leftover of the event. It is interesting to note that this nebula is also the reason why Charles Messier decided to create his famous Messier catalog. In 1759, Messier was trying to find the Halley comet, which was due to re-appear in the Taurus constellation[2], but in fact made an observation of the Crab Nebula because he thought it had a similar shape to that of a comet; in order to not make this mistake again, he started compiling a catalog of such comet-like objects now known as the Messier catalog. He named the first entry in his catalog M1, which corresponds to the Crab Nebula; the remaining objects would later be associated to not only nebula, but also star clusters and even galaxies.

As we have mentioned, supernova events were probably the first type of variable sources detected. However, no records of such events are found before 185 AD, which means that the very first recorded discovery of a variable source in the night sky was Algol[3] “The Raging one” by the ancient Egyptians in 1224 BC (Jetsu et al., 2013). Interestingly, ancient Egyptians also looked up to the sky for answers to their own personal enigmas: their scribes used to compile calendars of good and bad days of the year which were based on very accurate observations of sources in the night sky; in part, they were so accurate because they also had imposed religious and mythological meaning to astronomical events. In the case of Algol, they must have thought it had major mythological importance since its period was imprinted in the cycles of lucky and unlucky days of the Cairo Calendar, the best preserved ancient Egyptian calendar to this day (Jetsu et al., 2013). Through this record, Jetsu et al. (2013) found that the period of the variability of Algol increased from 2.850 days in 1224 BC, to 2.867328 days in 2013. This increase is predicted by physical models that describe the variability of Algol, known to be caused by

---

[2] Date and additional information regarding the 1759 sighting of the Halley comet can be found in the following website: `https://www.messier.seds.org/xtra/history/50comets.html`

[3] Algol is an eclipsing binary, meaning that it has a companion which creates the changes in the apparent brightness that we observe on earth.

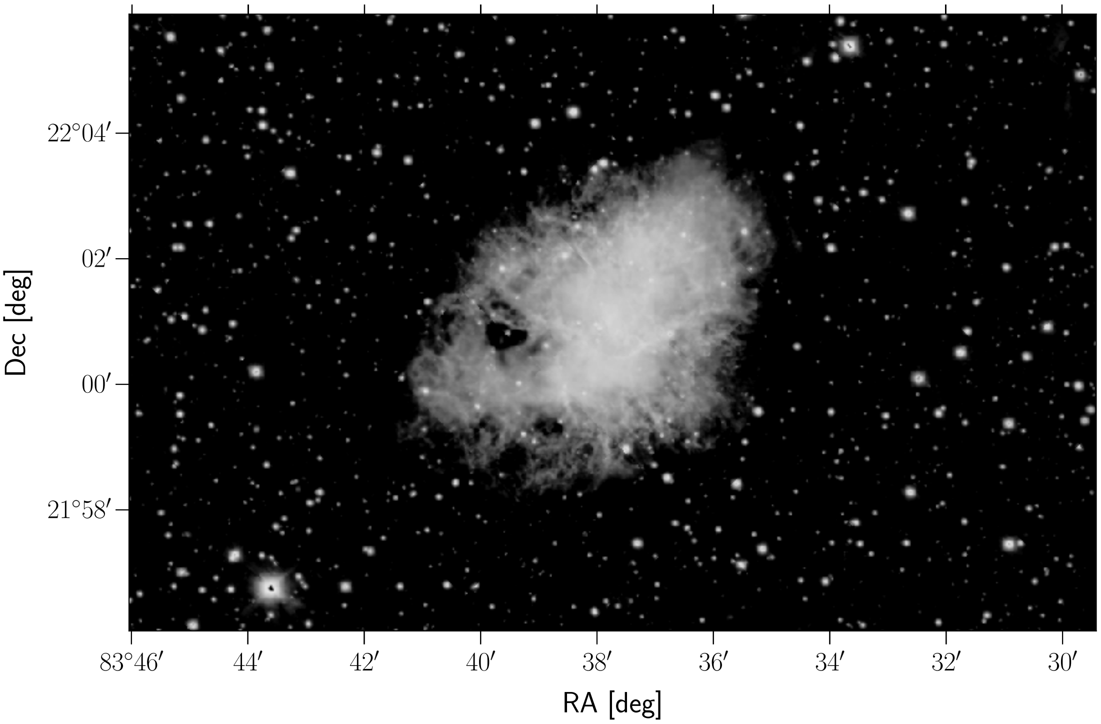

Figure 1.1: *Pan-STARRs DR1 i-r-g bands composite image of the Crab Nebula.*

the presence of a close companion with whom gas exchange occurs. This discovery should make astronomers more interested in the history of their field of study, because maybe we do not really know how much very ancient cultures knew about the physical properties of bright sources in the night sky and some of those properties might come in handy for the next publication.

In the west, the discovery of variable sources not related to supernova only came after the Renaissance. In 1596, David Fabricius was randomly using the star now known as Mira (Omicron Ceti) in order to determine the position of the planet Jupiter (which he at the time had mistaken for Mercury) when he noticed that the star increased from magnitude 3 to magnitude 2 in some 20 days in August (Hoffleit, 1997). He continued observing the star and noticed that it had faded during September, only to disappear completely by October; because of this he misclassified it as a nova (Hoffleit, 1997). Only in 1638 did Johann Holwarda actually determine its 11 month period[4], thus classifying it as a variable star (Hoffleit, 1997). Mira became the prototype star for a class of variable sources later named Mira variables, which are known to pulsate with a fixed period of long duration and constant brightness changes. Following the discovery of Mira, many started looking into the phenomena of variability, resulting in more variable stars being discovered. Such examples are Delta Cephei and Beta Lyrae (both by John Goodricke in 1784; Goodricke 1786). Delta Cephei (δ Cep from here on) is another star prototype which spawned the variable class of Cepheids, which, similarly to Mira variables, are also characterized by a fixed (although much shorter) period and amplitude. It is safe to say that, by this time in the late 18th century, astronomers were beginning to understand that the night sky was not as eternal as classical thinkers like Aristotle had them

---

[4] More information and references regarding Mira on the following web pages:
`https://archive.is/20071024210620/http://subdomainname.yurisnight.net/~spider/spider/Vars/mira.html`
`https://www.aavso.org/vsots_mira2`

believe.

1.2 The Beginning of Modern Research into Variability

All the theoretical background laid in the first half of the 20th century started to hint at solutions for the variability known to occur in many stellar sources. Both Cepheid and Mira variables are sources whose variability is due to their departure from what astrophysicists call the Main Sequence (MS). The MS phase is the period in the life of a star since its luminosity output starts to be mostly due to nuclear reactions in its core turning hydrogen into helium rather than due to the release of gravitational potential energy from their early contraction. After the star departs from the MS, the fusion reactions in its core start turning helium into carbon/oxygen. It was discovered empirically when 3 researchers in the early 20th century were working on plots of indices of temperature versus apparent brightness of stars located in clusters (Russell, 1914; Rosenberg, 1910; Hertzsprung, 1911)[5]. Because stars in clusters are all approximately at the same distance from Earth, their apparent brightness is directly related to their luminosity. In this plot one is able to discern a band of stars which cluster on the 2-dimensional plane along a specific path; this was later named the MS of stellar evolution. This sort of plot was later named an Hertzsprung–Russell Diagram, or HRD in abbreviated form, in honor of the scientists which first worked on it; however the very first record of a plot of this sort was by Rosenberg in 1910 (Rosenberg, 1910). Later in this work we study the color-magnitude diagram (CMD) of our variables, which is the observational equivalent of the HRD. In a CMD it is the color, difference in brightness in two measurements with different bands, of the sources which is a temperature index, with the reddest sources being the coldest and the bluest sources being the hottest.

Pulsating variables such as Miras and Cepheids are stars which have already evolved away from the MS and started burning helium in their core. When this happens, the star starts to expand, increasing its overall luminosity because of the higher surface area but also decreasing their surface temperature. This process is also notable in the HRD and Hertzsprung called this clustering of stars in the plot the Asymptotic Giant Branch (AGB). Miras and Cepheids are giants already located in the AGB of an HRD. These sources are also very important for distance estimations in Astrophysics, specially Cepheids of δ Cep class (there exist other types of Cepheids). Their fixed period and amplitude in brightness changes make them extremely good standard candles: sources which have known properties of luminosity shared by the entire class of objects. This class of stellar sources have what is called a luminosity-period relation. From this relation one can deduce the absolute magnitude (magnitude at a distance of 10 pc) of a Cepheid by finding the period of the variability and then get the distance from the observational value of the apparent magnitude! This latter part is possible because of the distance modulus μ, which relates the distance, absolute and apparent magnitudes of a source:

$$\mu \equiv m - M = 5\log\left(d_{pc}\right) - 5 \tag{1.2}$$

These findings began to make astrophysicists understand how variability could be linked to very intrinsic physics of stellar evolution such as in the case of Mira stars and supernovae.

---

[5] For information on the contributions of Hertzsprung please see the review by Strand (1968)

1.2.1 Star Formation and Young Variables

We have shown that stellar sources are known to evolve and that some present physical mechanisms which cause their apparent brightness to change over time. In the case of Algol, Mira, Cepheids, supernova and nova events, the changes in brightness have well defined periodicy and amplitudes[6]. However, in this thesis we are interested in another sort of variables, which are Young Stellar Objects (YSO). Although this nomenclature only became popular in the second half of the 20th century, it was in the 1940s that their research began with the discovery of a new class of variable stars whose prototype star is T Tauri (T Tau; Joy 1945).

Before Joy worked on T Tau and the class of variables which it spawned, it was already an interesting object in the astrophysical community. It was discovered in the 1800s and was associated to the first ever discovered variable nebula located $20 - 30''$ west of T Tauri, Hind's Variable Nebula (NGC 1555; Hind 1864). The variable brightness of Hind's Nebula was also noted by Burnham (1890), who observed it to dim irregularly and also discovered low level nebulous emission surrounding T Tauri which had a localized $4''$ extension; this nebula was named Burnham's nebula[7]. In the same article, Burnham (1890) even mentions how the brightness of T Tau should be reviewed since it appeared to have dimmed and suggests that variable star observers should include it into their observations.

This new class of variables was found to change their apparent magnitude in a very irregular way, unlike Miras and Cepheids. Besides being aperiodic, which meant no luminosity-period relation would be possible, their apparent brightness was able to change up to 3 magnitudes very irregularly; additionally they were always associated with nebulae and were overall not very luminous. As Joy mentions in his original article, T Tau varied from magnitude 12.8 up to magnitude 9; variations which could happen quickly in the course of some weeks or very slowly during some months. Interestingly enough, throughout the course of the 1920s this change in brightness started to stabilize, setting on the upper values of its amplitude range until the present times (see Section 2.1.1; Beck et al. 2020).

T Tauri were known to be of spectral type F-K and to present prominent emission lines in their spectra, such as H_α, which along with the aforementioned features, separated them from typical F-K stars. But none of these features pointed to their actual age. The first clue was found by Viktor Ambartsumian, an Armenian astrophysicist who wrote on stellar associations in the late 1940s and early 1950s and found they were systems of positive total energy and thus were expanding (Ambartsumian, 1954). In contrast, stars also reside in clusters which are more well-known and often bound. Given the physical characteristics of the stellar components of such associations Ambartsumian determined that these systems had to be young. He computed an approximate age of a few Myr and 10 Myr for known T-associations and OB-associations, respectively. Given that these values were some 3 orders of magnitude inferior to the hypothesized age of our galaxy, Ambartsumian found that stars had to be actively forming in the present epoch of cosmological history and that stellar associations were thus composed of "infant" stars.

Researchers such as Hayashi (Hayashi, 1966) helped develop models which explain the physics

---

[6] Algols do change their period in time, as Jetsu et al. (2013) point out. The core collapse supernova also can vary in amplitude and period because they result from the death of a range of stellar masses, unlike type Ia supernova which happen at a specific mass.

[7] More information on Burnham's nebula can be found in the article by Matt and Böhm (2003)

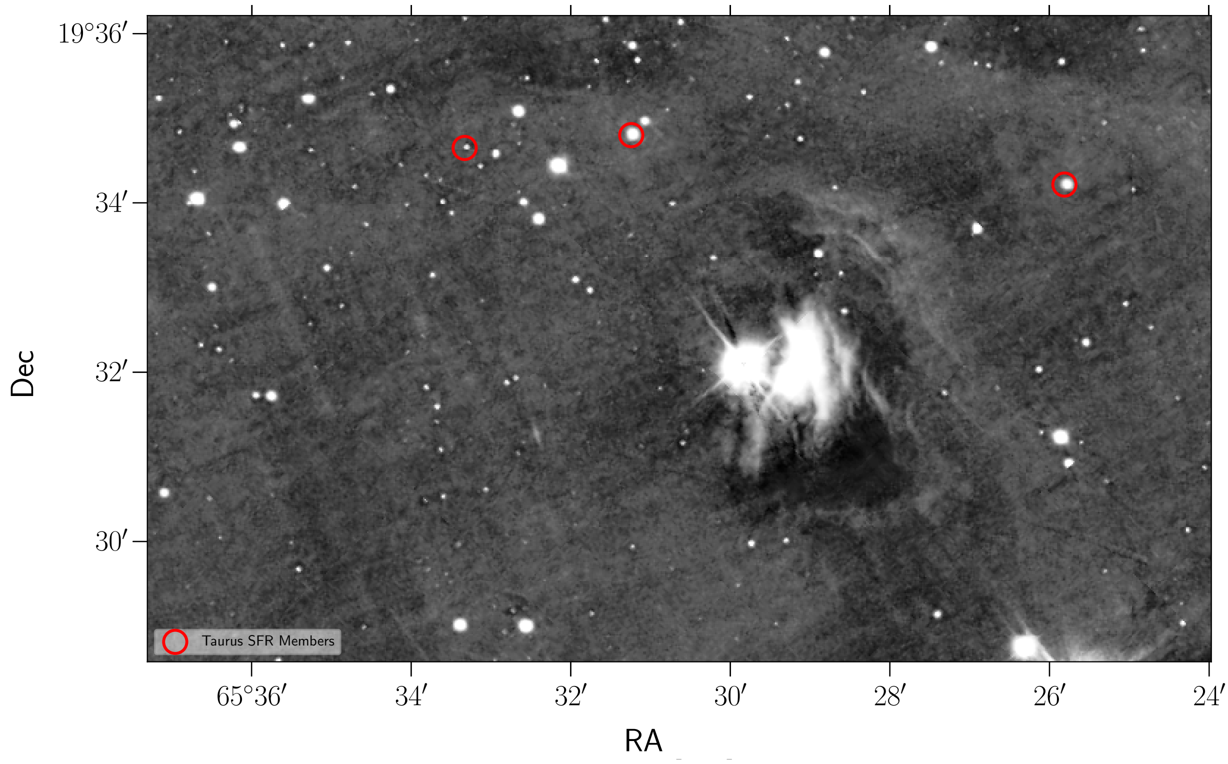

Figure 1.2: *Pan-STARRs i-band image of T Tau and Hind's variable nebula. In red circles are nearby stars to T Tau from the catalog of young members in Taurus SFR (see Chapter 3) which we have compiled from the works of Esplin and Luhman (2019) and Luhman (2018). This star is located in an isolated cloud towards the southern part of the Taurus SFR (see Figure 3.1 in which the location of T Tau is marked with a pink star symbol)*

behind early stellar formation, models which showed that T Tauri stars were objects in the very early stages of their development, having only just entered their pre-main-sequence (PMS) evolution. The research into T Tauri objects showed that YSOs go through an accretion disk phase where the star is still contracting and that it may present outflow events! These can spawn Herbig-Haro objects, which are nebula excited by shock induced phenomena from outflow events (Reipurth and Heathcote, 1997; Ambartsumian, 1954; Schwartz, 1975, 1983). The Burnham Nebula near T Tau is one such object and the first ever discovered.

In the next chapter we introduce the theoretical properties of the irregular variables which we study in this thesis: YSOs. We introduce the original T Tauri classification (Joy, 1945) and the posterior Lada (1987) YSO class. Finally we explain the different physical mechanisms which can induce variability in the brightness determinations of YSOs and how they can impact the amplitudes of the variability in different parts of the electromagnetic spectrum.

Chapter 2

Introduction

Variability of stellar sources is now much better understood than it was centuries ago. A more complete understanding of the process of stellar evolution, along with the technological possibility of observing the sky in other parts of the spectrum rather than the optical, allowed for a better understanding of the sources which we had spent an entire millennia trying to classify. Supernova and nova events are called **cataclysmic variables**, being as they correspond to such an energetic final moment in the stellar evolutionary path. Miras, Cepheids, RR Lyrae and δ Scuti stars are **pulsating variables**, being as their variability is due to expansions and contractions of the outer layers due to evolutionary changes in the core. Pulsating variables can further be classified into different pulsation period classes. This way, Cepheids, which vary in timescales of tens of days, differ from Miras which vary on periods upward of a month and finally RR Lyrae and δ Scuti are short period variables which vary daily. Thirdly, we have **eclipsing binary variables**, of which Algol stars are an example of[1]. Finally, we have **irregular variables**, a class which encompasses many different physical phenomena but is very much connected to YSOs.

Long et al. (2018) The variability which we study in this thesis, unlike the previously mentioned well characterized variability of pulsators such as Mira and Cepheid, is much more complex and less understood. The more recent star formation research from the late 90s to late 00s, both on the theoretical side and the observational side, which improved on the knowledge of the Initial Mass Function (IMF) at smaller masses, the theoretical basis for the youngest and most embedded protostars, the creation of more sophisticated modeling of accretion and extinction processes, provided much insight to the paradigm of YSO variability (Meyer et al., 1997; Herbst et al., 1994; Carpenter et al., 2001; Lada and Lada, 2003; Lada et al., 2006; Robitaille et al., 2006). The younger the source, the more embedded it is expected to be, so the very first studies were on the role of **extinction** in the variability of YSOs. Very young sources are still "coated" in the envelope of gas and dust in which they formed, but after some time the gas starts setting into the accretion disk component and the star become optically visible (Bertout and Bouvier, 1989; Bertout et al., 1988). This is the evolutionary stage now associated with T Tau and most T Tauri objects, however, as we shall see later in this chapter, the original T Tauri classification is more of a spectroscopic classification rather than a variability classification itself. While the star has a clear disk component, many

---

[1] This type is characterized by a close binary system in which gas exchange between the two exists. One of the stars has its Roche lobe filled while the other does not. More information on Algol type stars in the following web page: `https://www.aavso.org/vsots_betaper`

subclassifications exist which try to characterize different types of disks based on photometry (Teixeira et al., 2012), spectroscopy (Herbig, 1962), variability studies (Grinin et al., 1998) and a combination of all the former (Bouvier et al., 2003). Recently the Atacama Large Milimiter Array (ALMA; Wootten and Thompson 2009) has also been able to actually resolve structure in protoplanetary disks (Barenfeld et al., 2016; Long et al., 2018, 2019), further improving our understanding of this key component of PMS evolution.

By better understanding the properties of the disk it became clear that the complete variability in YSOs should have a complex origin, with multiple physical mechanisms at play. Carpenter et al. (2001) present a very complete and concise exposition of the known possible mechanisms for Near Infrared (NIR) variability in YSOs. These are: **extinction**, **disk activity**, **spots** and **multiplicity**. Extinction along our line of sight can change because of the disk+envelope component of YSOs, which can obscure the light from the central object in a very irregular way. Variability from the disk can be caused by a range of phenomena of which the most common is a temporary variable accretion rate, but also includes scenarios due to variable properties of the disk itself such as a variable inner disk radius Meyer et al. (1997). Spots are regions on the surface of the star where the temperature differs from the average, and which may induce variability due to changes in the surface coverage coupled with stellar rotation. Finally, multiplicity as a source of variability refers to possible eclipsing phenomena. In this chapter we will go over the aforementioned physical causes for variability in young sources (Section 2.2) but first we will present the criteria for T Tauri classification - as proposed by Joy (1945) - and the YSO classification - as proposed by Lada (1987).

2.1 Young Stellar Objects

2.1.1 T Tauri class

Following Joy (1945) and Herbig (1962), T Tauri stars were classified as follows:

- Irregular brightness variations of up to 3 magnitudes in the optical.
- Spectral type F5-G5 with hydrogen and the K and H lines of CaII in emission.
- The fluorescent FeI emission lines 406.3 nm, 413.2 nm must be present in the spectra.
- Additional characteristic lines such as [SII] or [OI] in emission or possibly [LiI] in absorption.
- Have a low luminosity.
- Be associated with dark clouds.

Figure 2.1 shows the brightness measurements of T Tau compiled from Harvard photographic plates in the V band during the first half of the 20th century. This type of plot is called a **light curve**. In the top panel of Figure 2.1 we can observe the irregular variability period which T Tau undertook prior to the 1920s. After this period, T Tau suffered a quiescent period in which its irregular, high amplitude variability stopped (Beck and Simon, 2001; Beck et al., 2020). Herbig (1962) notes how following what he called *the first phase* of T Tauri studies (referring to the first years of studies in which the link between T Tauri variables and the presence of an accretion disk was not well understood), most researchers neglected the variability and focused on finding H_α

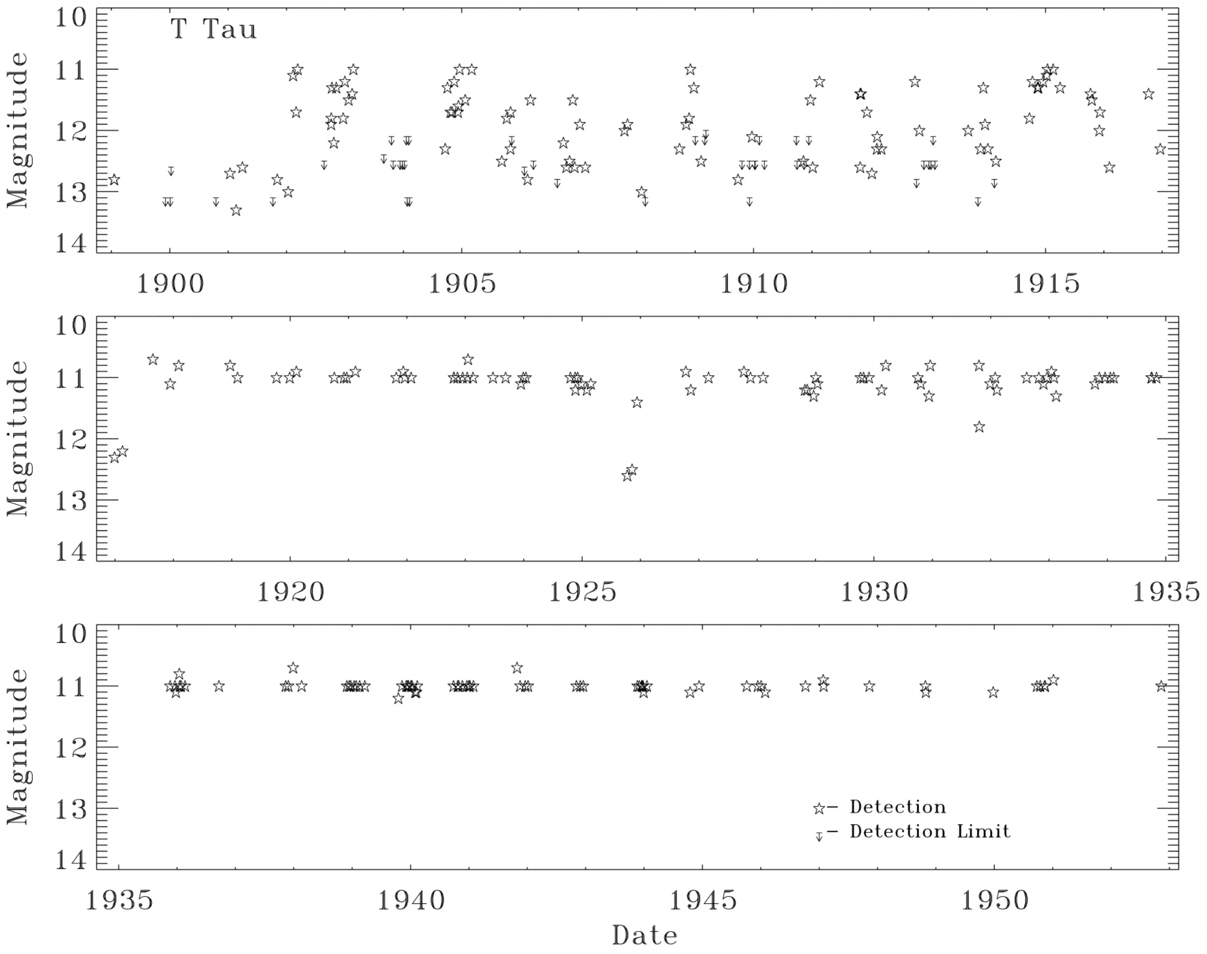

Figure 2.1: *Light curve of T Tau from 1899 to 1952 compiled from Harvard photographic plates in the V band. The points marked with a downward arrow refer to observations in which the source was too faint to be detected (Beck and Simon, 2001).*

line emitters associated with nebulae. These researchers would not know at the time that the features (that is localized behaviour observed during a specific time period of the light curve;i.e. increases/decreases in brightness such as the clear fast decrease around 1926 in Figure 2.1) in the light curves they were ignoring would end up being as complex as the information contained in a spectrum. This is because the presence of specific features in light curves can help infer the physical context in which the star resides which can then hint at the evolutionary stage of the source and its dynamical configuration as well.

The case study for the T Tau class, T Tauri, still presents today new information on young stellar evolution. It is in a multiple system composed of T Tau North and Tau South, which is a close binary (Sa/Sb). In Section 2.2 we will go over the state of the art arguments which try to explain the variability of this system.

Flores et al. (2020) notes that nowadays T Tauri has become a much more relaxed terminology which describes most optically visible YSOs. In the next section the YSO classification system proposed by Charles Lada in 1987 will be presented to the reader and how it integrates T Tauri class of variable stars will also be explained.

2.1.2 YSO class

One of the most important contributions of astrophysicist Charles Lada was his classification scheme for low-mass YSOs. The Spectral Energy Distribution (SED) is the spectral energy plotted as a function of the wavelength and is obtained via multi band photometry over a wide wavelength range. Most main sequence stars have SEDs which can be approximated by a black body, however, YSO often have disks or are so embedded that the shape of the SED is changed in the Mid Infrared (MIR) because of the contributions of these additional components to the stellar system. These properties enable a classification to be made by studying SEDs of young stars. Figure 2.2 presents the different expected SEDs for each class except for the now accepted class 0 introduced by André (1995). This latter class was found by sub-millimeter observations of extremely embedded sources which indicated an excess of energy in the Rayleigh-Jeans part of the spectrum. Summarizing:

- Class 0: embedded protostar in the process of collapse. Detectable in the mm wavelengths and radio.
- Class I: embedded protostar, still accreting. Detectable in the NIR and MIR, presents excess of radiation in the MIR due to thermal energy from the embedded cloud and disk material.
- Class II: optically visible YSO which presents NIR excess due to the presence of an accretion disk. Presents detectable broad or double peaked emission lines due to the rotation of the disk.
- Class III: optically visible YSO which has lost most of its MIR emission and its emission lines are much dimmer.

These classes are though to have an evolutionary link, such as we have described above. As gas starts collapsing inside a core of a giant molecular cloud (GMC), eventually an object in hydrostatic equilibrium is formed. This would be a class 0 source. This source continues its gravitational contraction, heating up its surroundings even more. This will make the

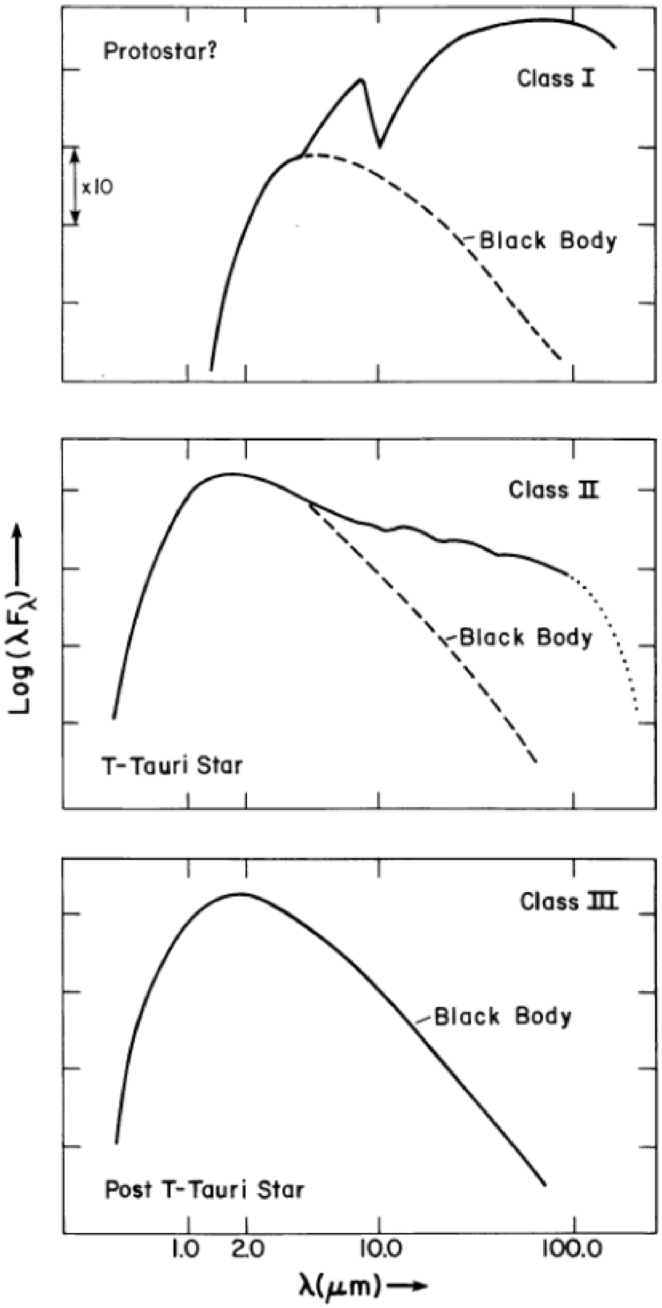

Figure 2.2: *Plot from Lada (1987) describing the 3 different original classes for the SEDs of YSOs. In the upper panel, class I: embedded source and the interrogation point next to the word protostar points to the ambiguity of the term. In the middle panel, the class II: vaguely corresponds to T Tauri class objects or YSOs which have become visible and are associated with protoplanetary disks. In the bottom panel, class III sources: YSOs which have moved on from the T Tauri phase and as such its SED differs from class II and starts resembling more a black body.*

surroundings of the source glow in the IR. At this point astrophysicists would detect a class I object. Further evolution from the source leads it to dissipate the cloud from whence it formed, becoming visible. This change dims its MIR energy output in the SED, however the presence of a protoplanetary disk still makes the source glow in the MIR. These are class II sources, vaguely T Tauri objects. When the disk dissipates we have a class III source.
The way astrophysicists classify young sources in the aforementioned classes is usually through the NIR or MIR slope in the log-log SED of a source,

$$\alpha = \frac{dlog\left(\lambda F_\lambda\right)}{dlog\left(\lambda\right)}. \tag{2.1}$$

Classically, positive slope values were associated with class I sources while negative values were associated with disk bearing stars down to -2 and then disk-less stars down to -3. Due to progress being made in protostellar disk evolution theory, new sub-classes have been added to refer to specific disks but authors in the literature have different definitions for them (Teixeira et al., 2012; Esplin and Luhman, 2019). This has created some ambiguous nomenclature regarding the disk subclasses. In this work we adopt the classes employed by Teixeira et al. (2012), which use the 2 disk classes by Lada et al. (2006) and adds a new one between Class I and Class II, flat spectrum sources:

- Flat Spectrum: sources with α slopes near zero ($-0.50 \leq \alpha \leq 0.50$). There have been suggestions that this class has unique properties which might indicate it is a unique evolutionary group (Greene and Lada, 2002; Muench et al., 2007).
- Thick Disk: also known as primordial disks, these are the youngest sort of disks. They are characterized by an α slope between -0.50 to -1.80.
- Anemic Disk: also known as optically thin disks, these are the more evolved counterpart of the thick disk. They are characterized by an α slope between -1.80 to -2.56.

Upward ($\alpha > 0.5$) and downward ($\alpha < -2.56$) of these values are Class I and Class III (named Naked Photosphere in Teixeira et al. (2012)) sources, respectively. In Chapter 6 of this thesis we investigate how this classification changes due to the variability associated with YSOs (see Section 6.4). YSOs are known to be highly variable mostly in the optical, however their variability extends to the mid infrared (see the following works: Wolk et al. 2013; Carpenter et al. 2001; Rebull et al. 2014) mainly because of spots and changes in the properties of the accretion disk.

2.2 Variability in YSOs

Many different physical mechanisms can cause the variability which is observed in YSOs, all with different brightness and color changes, but the most significant are spots, variable extinction and variable accretion. Depending on the exact configuration of the star system, different features will be observed in the light curve. Some sources can present clear features which are related to large-scale non-uniformities in the dust distribution in the disk which periodically or quasi-periodically appear in the line of sight. This behaviour was first observed in the star **UX Orionis** which then spawned the variable class of the same name similarly to T Tauri. The possible origins for these non-uniformities are the existence of a binary or multiple system or protoplanets forming in the disk (Grinin et al., 1998)[2]. Other sources like **AA Tau** show quasi-periodic occultations of the stellar photosphere by opaque circumstellar material which is thought to be caused by dynamical interactions between the warped inner edge of its accretion disk and the stellar magnetosphere (Bouvier et al., 1999). It was later discovered that the same source could possibly have a brown dwarf companion orbiting at a radius of 0.08 AU and that the interaction between the disk and the magnetosphere was highly dynamical and time dependent (Bouvier et al., 2003). This latter property was argued from observations of a quiescent period with no fadings and reduced variability in which emission lines were suppressed. One final interesting YSO variable is **FU Orionis**. This source was found to exhibit large increases in brightness followed by a slow decrease and is argued that this phenomenon is caused by bursts of high accretion (Herbig, 1977).

T Tauri, the prototype star for T Tau objects was found to be in a triple system in which all components, T Tau N and T Tau Sa/Sb exhibit photometric variability (Beck et al., 2020). Köhler and Kubiak (2020); Köhler (2021) argue that the variability of the infrared companion could be due to the presence of a circumbinary[3] thick and inclined disk. The variability of T Tau N is more difficult to explain but Beck et al. (2020) proposes that the extreme variability that T Tau presented before the 1930s (top plot in Figure 2.1) was because the redshifted outflow from T Tau Sa/Sb passed in front of T Tau N and created variable extinction along our line of sight.

Other causes can be linked to phenomena happening on the stellar photosphere. A common source of photospheric variability which has already been introduced at the beginning of this chapter are hot or cold spots. A variable accretion rate onto the stellar surface can also create a significant brightness variability as can the variability of the disk configuration itself. Meyer et al. (1997) created models for how the accretion rate, the amount of infalling matter from the disk/envelope that is accreted onto the stellar surface per unit time, could impact the colors of YSOs and found that it was dependent on the radius of the inner disk (and the inner disk dependent on the accretion rate itself). Interestingly, all of these phenomena are linked to the magnestosphere of the star and to how accretion in the young star happens (Herbst et al., 1994). Accretion from material in the circumstellar disk onto the stellar surface is channeled at free-fall speeds through accretion columns which follow the magnetic field lines. When this material reaches the stellar surface it decelerates, converting its kinetic energy into radiation via accretion shocks. This is the magnetospheric accretion theory that dominates the paradigm at the present time (Koenigl, 1991; Hartmann et al., 1994; Dodin, 2015). In this process, the accretion rate onto the surface is not constant throughout the lifetime of the disk (Hartmann et al., 1994; Herbst et al., 1994)), thus inducing variability in the brightness output of the source. In the regions where the accretion columns meets the surface of the star, the accretion shocks will create a hot spot. Hotspots are known to cover ∼1% of the surface of young stars, unlike cold spots which typically cover about 15%, and up to 60% of the stellar surface (see Section 6.1; Bouvier et al. 1993). Cold spots are also caused by magnetic activity but through a different mechanism which resembles what causes the more known Sun spots.

---

[2] More information in the following url: `https://starman.co.uk/variables/Young%20Stellar%20Objects/uxors.html`

[3] Accretion disk orbiting around both components to the binary system

2.2.1 Causes and Observational Consequences

It is important to be clear that the multiple mechanisms introduced in this section can all be actively causing the observed variability **simultaneously**. This is what makes the study of YSO variability so interesting and complex. It is also important to understand how the different mechanisms affect different parts of the electromagnetic spectrum. Variable extinction will mostly obscure optical wavelengths while variability due to accretion onto the star will be mostly covered in the infrared and redder parts of the optical spectrum (eg. optical bands which include the H_α line). In the following we will enumerate the possible mechanisms which can induce variability in the light curves of young stars:

- Hot Spots: caused by the transformation of kinetic energy into radiation on the stellar surface due to accretion shocks. Can be detected mostly in the optical but also in the NIR with less sensitivity.

- Cold Spots: caused by magnetic activity on the stellar surface. It is the most common variability mechanism for low-mass stars of all ages. Can be studied in the optical and NIR.

- Variable extinction: caused by the presence of circumstellar and interstellar material. YSO are known to be composed of an envelope + disk components that disappear over time. While the star has any of these components, changes to the configuration of the system or simply the disk/envelope themselves can cause changes in the extinction along our line of sight. It can be detected from the optical to the MIR with decreasing sensitivity as the wavelength increases.

- Multiplicity: caused by the presence of additional stars and/or brown dwarfs in the system.

- Variable accretion: caused by the irregular infall of matter onto the stellar surface, from material in the circumstellar disk. This mechanism is detectable from the optical to the MIR. Regions of the electromagnetic spectrum which have known emission lines linked to accretion such as H_α are most sensitive.

In this thesis we wish to apply the aforementioned theoretical background on the research of light curves of very young sources in the Taurus Star Forming Region (Taurus SFR). Our goal is to identify young variables in the Taurus SFR through a classification system using well known statistical variability indices. This classification system will be applied to both an optical and MIR data sets, enabling us to determine the set of optical and MIR variable stars in Taurus SFR and thus the fraction of optical/MIR variables. From this set of variables we aim to search the optical and MIR light curves for possible origins of variability. To do this we aim to research the expected properties that each possible origin for variability will induce in our data; study the general properties of the set of variables; analyze how their brightness and colors change over time; look into how the YSO classes can change because of variability; and finally understand how the different origins can create specific changes in the position of the variable source in a CMD.

In the following chapter we will first review the Taurus Star Forming Region, then briefly discuss the structure of the molecular clouds and properties of the known stellar members and finally present our catalog of YSOs in Taurus SFR and their general properties.

Chapter 3

Taurus Star Forming Region

The Taurus SFR is one of the largest (10-15 deg; Fleming et al. 2019) and closest (~140 pc; Pettersson 2008) star forming regions in the vicinity of the Sun. Its population is very sparsely distributed which enables the individual study of many star systems (Luhman, 2018). Taurus SFR is well known for its T-associations, which are associations of young irregular variables of F-K type also known as T Tauri objects. In contrast, Orion, is known for its OB-associations, which are young and massive stellar sources. Additionally the region is filled with known and confirmed M dwarfs and also some brown dwarfs. In the scope of this thesis, these are exactly the types of objects we are looking into: **low-mass stellar and substellar objects**.

3.1 Molecular Cloud Structure and Stellar Membership

Taurus SFR is one of the most complex molecular structures in the observable Milky Way. Given its proximity to Earth, as technology has advanced, more detailed structure can be observed in these clouds. Recently, Fleming et al. (2019) presented a very good review on the structure of the clouds, having discovered that there seems to exist, at least, two distinct groups of stars in these clouds. When compiling the histograms of Gaia Data Release 2 (Gaia DR2) (Gaia Collaboration et al., 2018) parallaxes the authors quickly saw a very detailed double peak, with some sources being located at $\sim 130 \pm 6$ pc (near population) and others at $\sim 160 \pm 4$ pc (far population); they also found that each population had common proper motions which differed between the two. Thus the Taurus clouds seem to harbour different populations of stars which are located $\approx$30pc apart along our line of sight. The same authors were also able to compute XYZ coordinates for stellar members of Taurus and presented the hypothesis that the clouds are shaped like a sheet which is edge-on facing earth, thus we see members seemingly clustered together when in fact they are distant along our line of sight. These findings were also corroborated by the works of Luhman 2018; Galli et al. 2019; Roccatagliata et al. 2020 and more recently Liu et al. (2021); Krolikowski et al. (2021). All of the aforementioned authors found evidence that distinct populations exist, each with distinct Gaia DR2 or Early Data Release 3 (Gaia eDR3) (Gaia Collaboration et al., 2021) kinematics and association with different clouds; all also found depth associated with the clouds; Liu et al. (2021) and Krolikowski et al. (2021) found evidence for older stellar members associated with the Taurus Clouds. To fully describe the complexity of the cloud structure we will give a brief review of the results from the aforementioned articles.

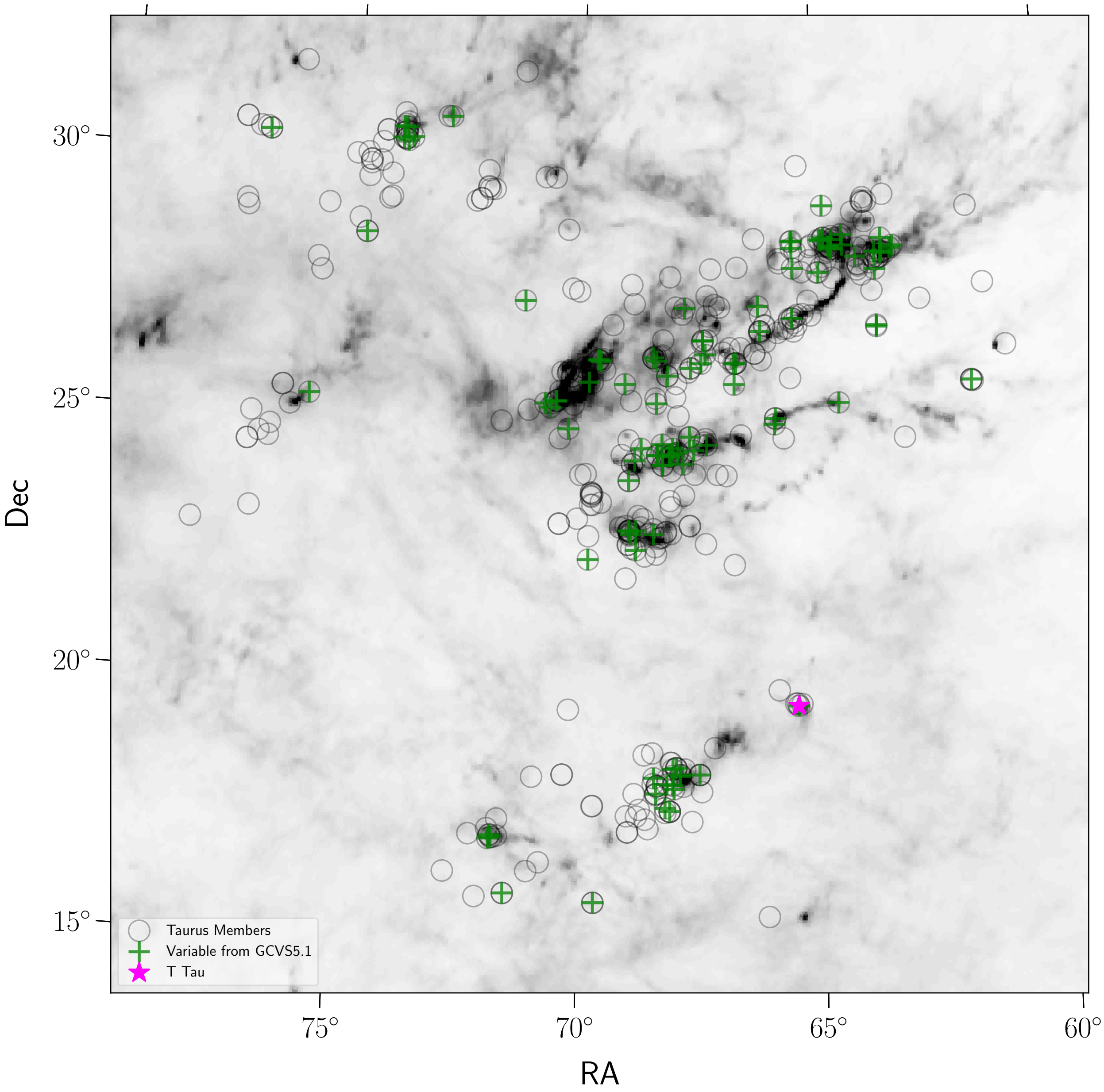

Figure 3.1: *Planck HFI 857GHz dust map with the probable member catalog considered in this work shown as grey open circles. Previously known variable stars from GCVS are marked with green plus symbols.*

Structure of the whole Taurus Region

All of the works mentioned expose complex structure in the Taurus clouds and hint at the existence of populations of stars with different and distinct kinematical properties. Many clouds seem to harbour stellar populations with distinct parallaxes and as such they must have depth along the line of sight. These include the cloud complexes B209/L1495, L1521/B213/B215, L1524/L1529/L1536 and L1527. The latter cloud is also known as Heiles Cloud (also known as Taurus Molecular Ring; Luhman 2018) and is characterized by a distance distribution with a gradient in Right Ascension (RA). This range is small, with an amplitude of about 10 pc, and its stellar population is found to share common kinematics and thus is considered a distinct population. However, interestingly, most of the clouds west from it harbour two distinct populations which seem to be about 20-30 pc apart along the line of sight.

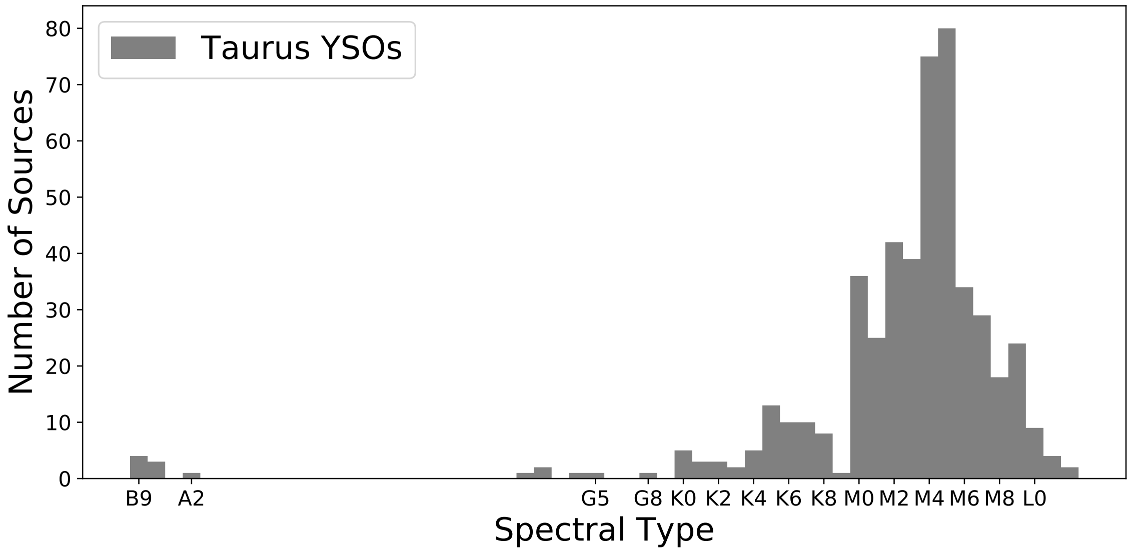

Figure 3.2: *Distribution of spectral types of Taurus YSOs determined by Esplin and Luhman (2019). The catalog is mostly composed of stellar sources with spectral type later than K but there also exist few G stars and few Herbig AeBe objects which are related to the earliest spectral types in the histogram.*

We then assume that most of the depth of the Taurus complex is along the western part of the region. In this context, it is also interesting to note the disparity in distance determinations from Gaia DR2 (Luhman, 2018; Galli et al., 2019) to Gaia eDR3 (Krolikowski et al., 2021) of the distance to cloud L1558 which might also be an indication of depth along the line of sight. The findings of multiple distinct stellar population within the clouds may indicate multiple star forming events, which in turn could cause an observable spread in age. Several authors have indeed found evidence for an age spread of up to 10 Myr. Recently, Liu et al. (2021) and Krolikowski et al. (2021) present evidence for the existence of even older members, indicating that different star forming events may have occurred along the last 10-20 Myr. Alternatively, these additional young contaminants may not be related to the Taurus clouds. However, most of the clustered sources in Taurus are found to be younger than 6 Myr and about 1-3 Myr on average (Liu et al., 2021; Krolikowski et al., 2021).

3.2 Taurus Young Members Catalog

For the purpose of this work we chose to use the list of members confirmed by Kevin L. Luhman and Taran L. Esplin who have worked together in the last decade trying to uncover new members of the association and confirming candidate ones. Luhman (2018) uses the Gaia DR2 parallaxes, proper motions and radial velocities to revise the membership status of each member in the previously built catalog (Luhman et al., 2017; Esplin and Luhman, 2017). This enabled the consolidation of the catalog through a kinematical approach and also resulted in a catalog of possible members composed of stars with Taurus-like kinematics but no spectra. Esplin and Luhman (2019) then studied spectra of the candidate members in order to assert membership, confirming new members extending into the substellar regime.

We use the catalog of Esplin and Luhman (2019) because it presents a bonafide set of YSOs, verified through low resolution spectra, in Taurus SFR, verified through Gaia DR2 kinematics. Of the 519 sources in this catalog, 28 do not have information on spectral types associated,

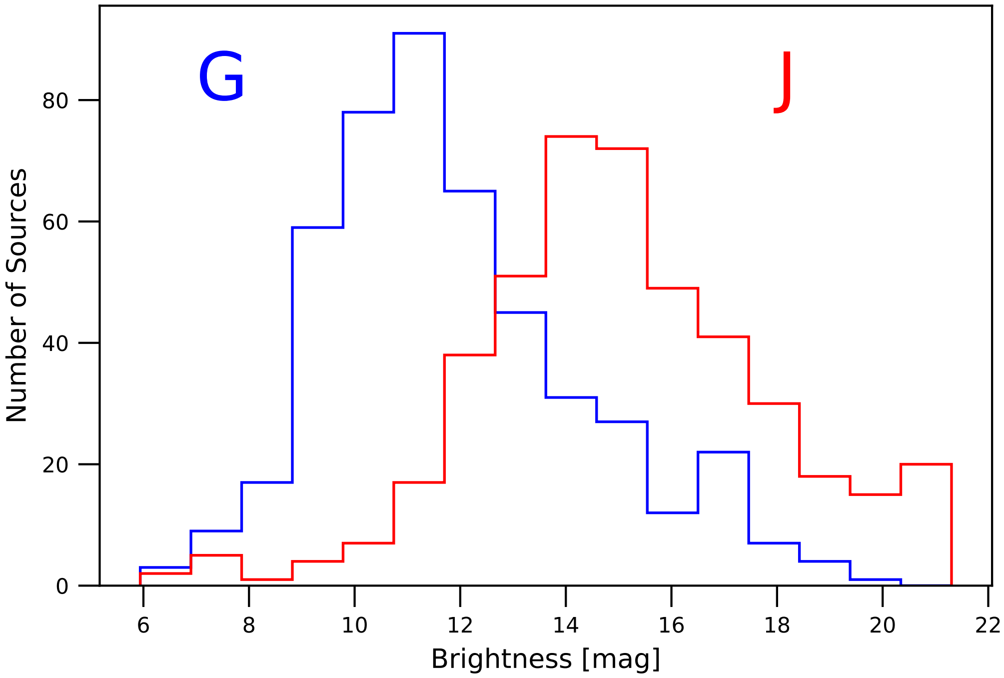

Figure 3.3: *Distributions of the brightness of the NIR J-band from Esplin and Luhman (2019) and the Gaia eDR3 G for the sources in our catalog of YSOs.*

and have been excluded by us. Thus, our final catalog of the young members in the Taurus association is composed of 491 sources. We have numbered each source in the catalog according to ascending RA and have kept this numbering as an identifier throughout this work. Figure 3.1 shows the sky distribution of these sources (grey open circles) on top of a Planck HFI 857GHz dust map; green plus signs mark known variables from the General Catalog of Variable Stars (see Section 3.2.2 from this work)). We can see that the YSOs in our catalog span the entire cloud complex and that most of the sources are located in the regions of higher cloud density. It is important, however, to note that the catalog is biased towards the sources which are easier to detect in the NIR, thus it is expected that few Class I sources are present in the catalog.

The catalog is mostly composed of M dwarfs (402) and G-K (6,60), however it does present few A and very late B stars - specifically four A0-A2 stars and four B9-B9.5 stars - and some (15) L objects. These A/B stars are known as Herbig AeBe stars, young (<10 Myr) intermediate-mass (2-8 $M_\odot$) stars still presenting an envelope+disk component. The L objects are called **brown dwarfs** (BD). BD are in the lower end of the Mass Function, in which we reach a limit in mass from which a star ceases to be able to sustain hydrogen fusion - the limit in mass is $\sim 0.075 M_\odot$ - and thus ceases to be a star, however BD can still burn deuterium (and lithium if they are more massive than $\sim 0.062 M_\odot$) and are formed by the same processes as stars. For stars already in the main-sequence, brown dwarfs are associated with the spectral types L-T-Y, from the hottest to the coolest, but for very young sources, brown dwarfs can extend into the M class; this means that we have (120) possible BD in our catalog of YSOs. From these 120 sources, 15 are classified as L type and the remaining have spectral types of M6 or later, which at an age of ~1 Myr should be brown dwarfs (Mužić et al., 2011). Most other sources in Taurus should have masses close to $M = 0.5 M_\odot$ with a subsample having masses up to 3-4 times larger than the sun Herczeg

Table 3.1: *Catalog of the YSOs in Esplin and Luhman (2019) which have an associated spectral type. NIR J photometry from Esplin and Luhman (2019) is also presented along with Gaia eDR3 G photometry, parallax and proper motions. The full table with the results from the analysis in 6 will be available online, following publication, in the following GitHub:* `https://github.com/AfonsoDoVale/Taurus-Variability.git`

ID	SimbadName	RA	Dec	rpos[a]	SpType[b]	G	J[c]	ϖ	μ_α	μ_δ
1		04:01:32.09	26:07:33.2	UKIDSS	M9.5		17.00			
2	2MASS J04034997+2620382	04:03:49.98	26:20:38.2	eDR3	M5.25	16.96	13.28	6.97	14.44	-19.27
3	2MASS J04044307+2618563	04:04:43.07	26:18:56.4	2MASS	K3					
4		04:05:32.15	27:33:13.9	eDR3	M4.75	14.68	11.37	7.61	11.31	-25.22
5	2MASS J04064263+2902014	04:06:42.64	29:02:01.5	eDR3	M4.5	15.40	11.83	6.09	10.98	-17.51
6	2MASS J04064443+2540182	04:06:44.44	25:40:18.2	eDR3	M5.75	16.34	12.70	6.52	14.01	-18.76
7	Gaia DR2 162260226605718784	04:06:51.35	25:41:27.8	eDR3	K6.5	11.82		5.64	14.60	-18.16
8	2MASS J04065134+2541282	04:06:51.36	25:41:28.8	eDR3	K4.5	12.04	8.77	6.30	12.20	-17.97
9	Gaia DR2 162259951730099968	04:06:53.65	25:40:36.9	eDR3	M5.5	16.09	12.40	6.58	14.14	-18.77
10	2MASS J04105425+2501266	04:10:54.26	25:01:26.6	2MASS	M2		16.27			
11	2MASS J04110081+2717163	04:11:00.83	27:17:15.8	eDR3	M9.5	21.07	15.92			
12	2MASS J04124068+2438157	04:12:40.69	24:38:15.7	eDR3	M3.5	14.56	11.15	6.73	14.23	-18.84
13	2MASS J04131414+2819108	04:13:14.16	28:19:10.7	eDR3	M3.6	12.52	9.64	7.84	8.29	-24.27
14	2MASS J04132722+2816247	04:13:27.22	28:16:24.7	eDR3	M0.5	12.20	8.83	7.36	8.11	-23.98
15	2MASS J04135328+2811233	04:13:53.28	28:11:23.2	eDR3	M5	20.39	13.64	5.88	8.86	-22.65
16	2MASS J04135471+2811328	04:13:54.72	28:11:32.9	2MASS	K-M		17.23			
17	2MASS J04135737+2918193	04:13:57.38	29:18:19.4	eDR3	M3	15.08	11.31	8.36	9.14	-23.77
18	2MASS J04141188+2811535	04:14:11.88	28:11:53.4	eDR3	M6.25	17.28	13.16	7.62	7.60	-23.84
19	2MASS J04141291+2812124	04:14:12.93	28:12:12.4	eDR3	K4	9.99	7.49	8.33	6.54	-27.79
20	2MASS J04141358+2812492	04:14:13.58	28:12:49.2	eDR3	M4.5	13.58	10.33	7.58	8.38	-24.54

---

[a] Reference for the coordinates

[b] From Esplin and Luhman (2019)

[c] J magnitudes from Esplin and Luhman (2019). They are mainly composed of 2MASS photometry, but also present UKIRT Hemisphere Survey data, UKIDSS DR10 and original photometry from the aforementioned work using the WFCAM instrument

and Hillenbrand (2014). This spectral type information is presented in Figure 3.2, in which we see that M4 and M5 are the most common spectral types in our catalog. We also employ the NIR photometry in the catalog of Esplin and Luhman (2019), which includes data from 2MASS (Skrutskie et al., 2006), UKIDSS (Lawrence et al., 2007) and additional photometry from the authors own work. More than 95% of the sources in our catalog have measurements in either J, H or Ks bands. The set of sources which does not have any NIR photometry is mostly (14/18) composed of secondary components in multiple systems and all of these sources have a Gaia eDR3 (see next Section) entry and photometry in G, Bp and Rp; the remaining consist of a primary in a multiple system (HD 28867) and 3 M dwarfs of which at least one is associated with a multiple system in the Simbad database.

3.2.1 Gaia Early Data Release 3

For a comprehensive look into the kinematics of the stellar members of the Taurus Clouds, which have been studied in detail by the several authors referenced in section 3.1, and to obtain accurate coordinates for most of our sources, we queried data from the Gaia eDR3. This release builds upon the DR2 by including more accurate and precise photometry and astrometry for about 1.8 billion sources (radial velocities still the same from DR2, however). We obtained 445 matches with our catalog of 491 sources by matching within $1''$[1] in the Gaia Archive. For each source we queried J2000 coordinates, parallax, proper motions, radial velocities, photometry in the G, Bp and Rp bands, and the associated errors. After matching, the coordinates in our catalog are mainly from Gaia eDR3 (445) but also 2MASS (31) and UKIDSS (15) surveys for sources with no Gaia data.

The brightness distributions for the J band included in the compilation by Esplin and Luhman (2019) and the Gaia eDR3 G are presented in Figure 3.3. We can see that the G brightness peaks near $11 < G < 12$ while the J brightness peaks near $14 < J < 15$. The catalog of Taurus YSOs is presented in Table 3.1 in reduced form, showing our own source identification as stated above (ascending RA), SIMBAD Astronomical Database[2] identification, coordinates with the corresponding reference, the spectral types and J photometry from Esplin and Luhman (2019) and the Gaia eDR3 G photometry, parallax and proper motion measurements.

We investigate the parallax measurements and find the same double peak distribution that the authors quoted in Section 3.1; see Figure 3.4. A third peak which seems distinct from the reported peak at 6-6.5 mas, but is very close to it, (≈ 7 mas) starts to appear in the middle panel of Figure 3.4, which shows the Gaia eDR3 G as a function of the determined parallax. In the top panel of Figure 3.4 we see the distribution of the parallax measurements and this possible third peak is much less visible (maybe it is the effect of a larger parallax range existing for the nearer population), but the "two horns of Taurus" (Fleming et al., 2019) are quite visible. Figure 3.4 also shows the distributions of the catalog members in the proper motion space (μ_α vs μ_δ) in the bottom panel. We can visually distinguish some clustering which is related to the different stellar populations that we described in Section 3.1. We can also see that there exist sources which seem to have proper motions unrelated to any of the visually distinct clusters.

Figure 3.5 shows the optical and NIR CMDs for the members of our catalog using the Gaia Rp and Bp bands and the NIR photometry compiled in our catalog (Esplin and Luhman, 2019).

---

[1] This aperture for matching is found to be optimal for matching external catalogs with the Gaia DR2 data by Marrese et al. (2019)

[2] `https://simbad.u-strasbg.fr/simbad/`

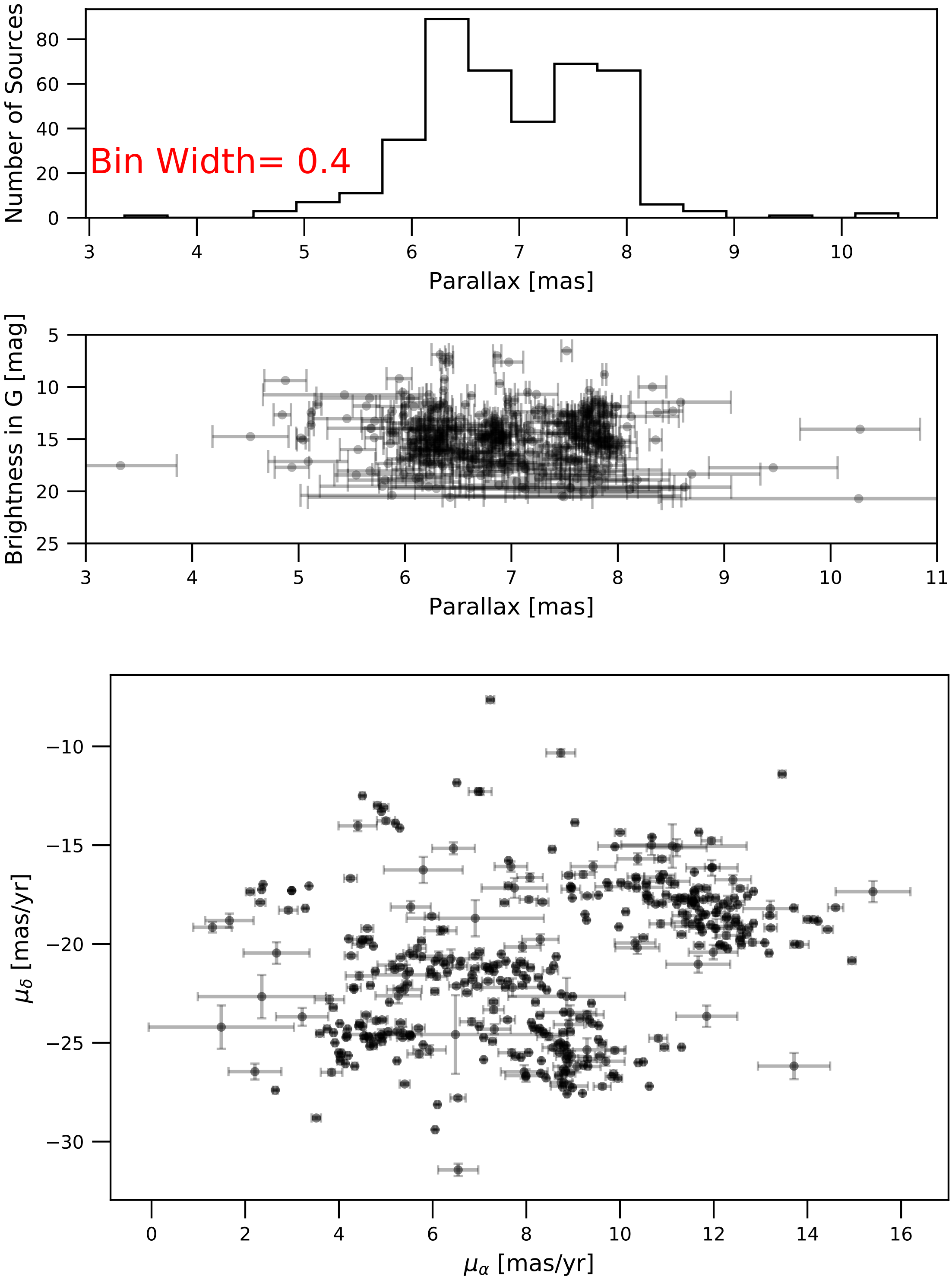

Figure 3.4: *Top panel: Distribution of the parallax measurements from Gaia eDR3; middle panel: Gaia G magnitudes as a function of parallax; bottom panel: distribution of the sources in the proper motion space from Gaia eDR3. We can see the double pick in the two top panels, but the middle panel seems to show a possible third peak near* $\varpi \sim 7$.

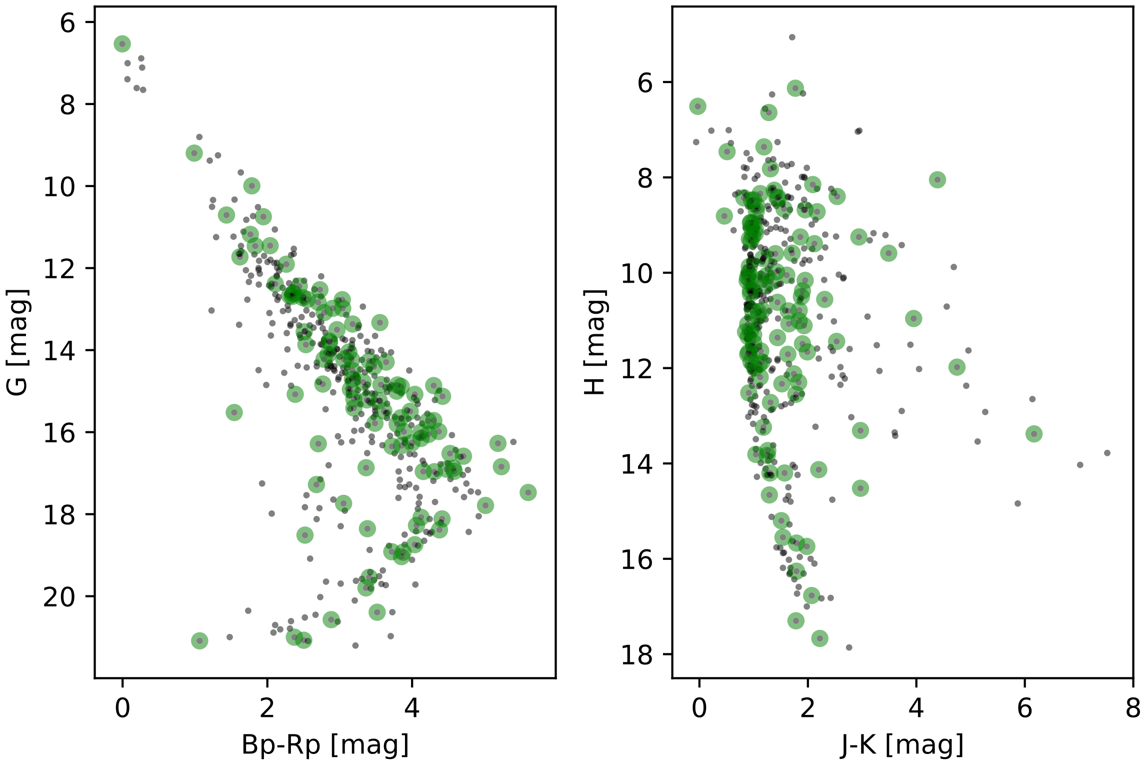

Figure 3.5: *Color-Magnitude plots of the members of the Taurus Catalog (black dots) with Gaia photometry, on the left, and JHK photometry, on the right. Green circles are sources flagged as variable by the General Catalog of Variable Stars (see section 3.2.2).*

In the Gaia CMD we can see the earlier spectral type population separated from the other sources as they represent the few massive stars in the Taurus clouds. In the NIR CMD, on the other hand, we can see the infrared excess that some sources present through the J-K color, which is a proxy for extinction and/or emission from the disk+envelope component. The stellar members in our catalog are composed of young, later type stars which are still in the PMS phase and clearly still present remnants of the molecular clouds in which they have formed (disk, envelope or both) as is expected from the canonical age for Taurus - ∼1 to 3 Myr. Employing the protostar class nomenclature introduced in Section 2.1.2, our catalog should then have Class I and Class II sources in excess when compared to older regions. Because many of the physical causes for variability in YSOs are related to the context in which the star is born, the younger the star forming region, the higher the fraction of variable YSOs should be.

3.2.2 General Catalog of Variable Stars

The General Catalog of Variable Stars (GCVS) is a catalog of variable galactic and extragalactic stars which has been in the works since 1946 by Moscow researchers. It is one of the largest, most thorough and complete catalogs on variability ever compiled. It is presently in its fifth (5.1) edition and is now only supported and updated electronically. Edition 5.1 of the GCVS has information on 51 853 stellar sources, most located in the Milky Way but also in the Magellanic Clouds and some nearby galaxies (Samus' et al., 2017).

The requirements for a source to be present in the GCVS, as per Samus' et al. (2017), has changed over the years, however at the present time 3 rules must be followed:

- Brightness variations which have reliable references
- It must be possible to reliably identify the stellar source
- Sufficient photometric data on the brightness variations of the source so that it is possible to classify it according to the GCVS variability types, or to establish that such classification cannot be done, thus possibly making it necessary to introduce a new class type.

It is possible to see from these requirements why this catalog is the most thorough since it requires a lot of research into the source before it is introduced into the catalog. One of the most important features of GCVS is that it provides references not only for studies done on each variable but also for imaging and charts in which it appears. The information compiled in the GCVS is lengthy, including not only classifications for its observed variability, but also maximum/minimum amplitudes of the observed variations, period estimations, proper motions, spectral type, etc[3]. For this work we are only interested in the spectral type, the variability type and period of variability.

Table 3.2: *GCVS information on all the YSOs in the catalog presented in Table 3.1. Not all information is listed in this table and GCVS5.1 also offers a text file with remarks on specific sources which can be found in the following url:* `http://www.sai.msu.su/gcvs/gcvs/gcvs5/remark.txt`.

ID	GCVS	Spectral Type (GCVS)	Variability Type[4]	Ref1[5]	Ref2[6]
7	V1195 Tau		IT	76033	UCAC2
8	V1195 Tau		IT	76033	UCAC2
13	V1095 Tau		BY	73323	73324
14	V1096 Tau		BY	73323	73324
19	V0773 Tau	K2ea	INB+BY	08567	10000
20	FM Tau	M0e(T)	INST	08289	10000
21	FN Tau	K5e(T)-M5e(T)	INST	08289	10000
22	CW Tau	K0Ve-K5Ve(T)	INST	08292	10000
29	FP Tau	M2.5Ve-M5Ve(T)	INT	08292	10000
31	CX Tau	M1.5-2.5Ve(T)	INST	08292	10000
32	V1098 Tau		INB	73325	73324
33	FO Tau	ea	INS	08289	00598
52	V1068 Tau		INT	72159	72160
54	CY Tau	M1-2Ve(T)	INST	08292	10000
55	V1312 Tau	M2Ve	IT	80021	GSC
60	V0409 Tau		INS	05614	05614
64	V0410 Tau	K3Ve-K7Ve	INSB	05796	10000
65	DD Tau	K6Ve-M1Ve(T)	INST	06996	10000
66	CZ Tau	M1.5-2Ve	INSB	06996	10000

---

[3] Information regarding all the information contained in the GCVS can be found in the following webpage: `http://www.sai.msu.su/gcvs/gcvs/gcvs5/htm/`

[4] More information on the specific classes in the following url: `http://www.sai.msu.su/gcvs/gcvs/vartype.htm`. Additionally, information on the new variable types being tested by the GCVS team can be found here: `http://www.sai.msu.su/gcvs/gcvs/classif.htm`

[5] Reference to a study of the star. References listed in the following url: `http://www.sai.msu.su/gcvs/gcvs/gcvs5/ref.txt`

[6] Reference to a chart or photograph of the star. See the link in [5]

70	V0892 Tau		INA	68258	68258
75	V1023 Tau		INT	70122	70121
82	FQ Tau	M2e(T)	INST	08289	10024
83	FQ Tau	M2e(T)	INST	08289	10024
84	BP Tau	K3Ve-M0Ve(T)	INT(YY)	05469	00598
86	V0819 Tau		BY	67323	67322
87	FR Tau	ea	INS	08289	10024
88	V1070 Tau		INT	72159	72160
116	DE Tau	M1-3Ve(T)	INST	08292	10000
117	RY Tau	F8Ve-K1IV-Ve(T)	INT	09990	09990
118	V0987 Tau		INT	69268	BD
119	T Tau	F8Ve-K1IV-Ve(T)	INT	00574	02301
123	FS Tau	M1e(T)	INST	08289	10036
124	V1071 Tau		INT	72019	72160
137	FU Tau	ea	INS	08289	00596
139	FT Tau	ea	INS	04046	04046
149	V1201 Tau		IT	76033	GSC
152	IP Tau		INS	08292	03903
159	FV Tau	K5e	INSB	04046	10024
162	DF Tau	M0-3Ve(T)	INST	05785	10000
163	DG Tau	GVe(T)-M0Ve	INST	05785	10000
179	GV Tau	e		08799	08799
180	FW Tau	ea	IN	08289	10024
184	DH Tau	M0-M1Ve(T)	INST	08292	10000
185	DI Tau	M0-M1Ve(T)	INST	08292	10000
187	IQ Tau	M0.5e-M2e(T)	INST	08292	10000
191	UX Tau	G0Ve-K2Ve(Li)	INT	04050	09991
192	UX Tau	G0Ve-K2Ve(Li)	INT	04050	09991
195	FX Tau	M1e-M4e	INSB	08289	10000
197	DK Tau	K5Ve-M1Ve(T)	INST	04046	10000
198	DK Tau	K5Ve-M1Ve(T)	INST	04046	10000
201	ZZ Tau	M4e	INSB	06401	10000
204	V1320 Tau	M1	IB	80021	GSC
207	V0927 Tau		UV	68262	68285
212	V1213 Tau		IN	77037	2MASS
213	HL Tau	K7:e(T)-M2:e(T)	INT	10036	10000
214	XZ Tau	G5Ve-M3e(T)	INT	07822	09991
217	HK Tau	Ke-M0.5Ve	INSB	04048	10000
218	HK Tau	Ke-M0.5Ve	INSB	04048	10000
219	V0710 Tau	K7e-M3e	INB	04050	04050
220	V0710 Tau	K7e-M3e	INB	04050	04050
226	V1075 Tau		INT	72019	72020
227	V0827 Tau		UV+BY	67329	67322
228	V0806 Tau	ea	IN	08799	00596
229	V0826 Tau		BY	67322	67322

232	V0928 Tau		INB:	68263	68263
242	GG Tau	K5-M0Ve(T)	INT	00598	10000
244	FY Tau	K7-M0e(T)	INST	08289	10037
245	FZ Tau	cont+e(T)	INST	08289	10037
250	UZ Tau	G5Ve-M1-3Ve(T)	INT(YY)	09478	10000
251	V1076 Tau		INT	72161	72020
256	V1321 Tau	M2	IB	80154	GSC
259	GH Tau	M1-M3Ve	INB	04046	10037
260	V0807 Tau	ea	IN	10024	10024
263	V0830 Tau		BY	67323	67322
272	GI Tau	K5-7Ve(T)	INST	08289	10037
273	GK Tau	K5-7Ve(T)	INST	08289	10037
274	IS Tau	ea	INS	04051	10024
276	DL Tau	GVe-K7Ve(T)	INST(YY)	10027	10000
278	HN Tau	K5e(T)	INST	04050	10000
283	DM Tau	K5Ve-M2Ve(T)	INST(YY)	04050	10000
284	CI Tau	G:e(T)-K7Ve(T)	INST(YY)	04046	00598
289	IT Tau	K2e	INSB	04051	10024
290	IT Tau	K2e	INSB	04051	10024
300	AA Tau	K5Ve-M1Ve(T)	INT	06996	09991
306	HO Tau	K-M0.5e(T)	INT	04051	10000
307	FF Tau	K8V-M1V	INSB	04046	00621
309	DN Tau	K6Ve-M1:Ve(T)	INST	06996	10000
316	HQ Tau		INS	04046	04046
321	HP Tau	K3e	INB	04046	10000
324	V1025 Tau		INSB	70124	70166
328	V1324 Tau	M1.5	IB	80154	GSC
329	V1026 Tau		INT	70126	70125
339	V1115 Tau		BY	73325	73324
347	GM Tau	ea	INS	08289	10024
348	DO Tau	GVe-M1Ve(T)	INST	04046	10000
349	HV Tau	M1Vea(Li)	INT	04046	10024
352	V1204 Tau		IT	76033	GSC
365	VY Tau	M0e(T)	INT	05472	09994
366	V1079 Tau		INT	72019	72160
367	GN Tau	ea	INS	08289	04046
382	IW Tau		INS	03905	03905
394	V0999 Tau		UVN	69272	69273
395	V1000 Tau		INT	69272	69273
396	V0955 Tau		INB	68263	68286
399	DP Tau	M0.5Ve(T)	INT	00598	10000
401	GO Tau	K5Ve-M0e(T)	INST	08289	10000
406	V1334 Tau	K1	IB	80154	DM
408	V1206 Tau		IT	76033	GSC
414	DQ Tau	K7-M1Ve(T)	INST	10025	10000

415	V1001 Tau		INT	69277	69275
416	V1001 Tau		INT	69277	69275
417	DR Tau	(cont+e)-K5Ve(T)	INST(YY)	10026	10000
419	DS Tau	K3Ve-M0:Ve(T)	INST	00598	10000
430	UY Aur	K7Ve(Li)	INT		GSC
433	GM Aur	K3Ve(T)-M0	INT	00598	GSC
435	V0396 Aur	K0Ve	INT	N0198	72160
438	AB Aur	A0Ve+sh	INA		HIP

We matched our catalog with GCVS 5.1 and obtained 125 matches within a radius of $3''$ and checked matches with separations larger than $1''$. Of all sources, only 4 matched with separations larger than $1''$; these are DS Tau, GZ Aur, HP Tau and V710 Tau. 8 secondary components to a multiple stellar system also matched within $3''$ along with their primaries. One source, #179 (GV Tau), does not have a variable type classification even though it matched. The total number of unique matches is thus 116. Most variability types are related to irregular variables associated with dark nebula (IN). The complexity of this classification, however, lies on the multiple subclassifications which can be associated with irregular variables. Table 3.2 presents the GCVS identifications (along with our source identification described above), spectral types, variability types and references for both studies of the variables and images/charts of the variables. The eruptive variable types which are associated with the sources in our catalog are the following[7]:

- **IB**(4/116; $\sim 3\%$): Irregular variables of spectral type later than F-G and earlier than K-M. This classification is reserved for sources which have not been well studied.

- **IN** (17/116; $\sim 15\%$), of which 13 ($\sim 76\%$) are **INS**: CGVS describes these sources as Orion variables. These are irregular variables which are known to be eruptive and be associated with nebulae or simply located in the same region. If the light variations change 0.5 - 1.0 mag within several hours or days then the classification is **INS**. This fast variability flag noted by the letter **S** is also present in the following classifications and has the same connotation.

- **INA** (2/116; $< 2\%$): These sources are described in GCVS as Orion variables of type B-A or Ae. This classification differs from IA because of the association with nebulae. These sources are also known to often be characterized by abrupt Algol-like fadings which are thought to be linked to non-uniform dust structure around the star. This phenomena is linked to a class of young variables named after UX Orionis, which are Herbig AeBe objects presenting the aforementioned fadings.

- **INB** (19/116; $\sim$ 16%), of which 11 ($\sim$ 58%) are **INSB**: GCVS describes these sources as Orion variables of type F-M or Fe-Me. The authors state that the sources of type F can also present the Algol-like fadings of their INA counterparts. K-M stars are noted to present flares along with irregular light variations.

---

[7] In the itemization that presently follows, the numbering associated with each class corresponds to how many matches we got with our catalog and its associated ratio. Keep in mind that as we have mentioned earlier, these classifications overlap, which means some sources can have more than one classification; this is the case of #227 (V0827 Tau) which is in class UV and BY!

- **IT** (66/116; $\sim$ 57%), of which 58 ($\sim$ 88%) are **INT**, of which 28 ($\sim$ 48%) are **INST**: T Tauri type. GCVS states that the unique criteria for assignment onto this class is purely spectroscopic: Spectral types in the range Fe-Me and specific spectral features in emission which include the fluorescent emission lines Fe II 4046 and 4132 A, both of which are anomalously intense in these variables.
- **INT (YY)** (6/116; $\sim$ 5%), of which 4 (67%) are **INST (YY)**: These variables show evidence for the infall of matter through the presence of absorption components on the redward sides of emission lines; i.e. variables which are associated with accretion.
- **UV** (3/116; $<$ 3%), of which 1 (33%) is **UVN**: eruptive variables of UV Ceti type. They can present flares which cause variation amplitudes of up to 6 magnitudes in V and even larger in the ultraviolet part of the spectrum and are associated with the spectral types of K Ve-M Ve. **UVN** variables are associated with flaring Orion variables of spectral types Ke-Me which are associated with nebulae.

On the other hand, the few periodic variables which are assigned to sources in our catalog are limited to the BY Draconis type:

- **BY** (9/116; $\sim$ 8%): GCVS5.1 describes this class as follows, "emission-line dwarfs of dKe-dMe spectral type showing quasiperiodic light changes with periods from a fraction of a day to 120 days and amplitudes from several hundredths of a magnitude to about 0.5 mag in V. As we have described in Section 2.2 some sources can present light variations due to non uniform brightness along their surface due to hot and cold spots. The phenomena which characterizes the periodicity of this variable are cold spots, but if the source has a disk, hot spots can also influence the variability albeit in an irregular way unlike cold spots.

It is interesting to note that most INB and INT (YY) sources show rapid variability and that almost half of INT sources do too. Most of the YSOs in Taurus are classified as either INB, INT or simply IN. The latter are sources which still lack data to confirm a subtype and many can be related to INB, INT or other types. We thus expect much of the sample of YSOs in Taurus to present fast variability.

Table 3.2 does not include all information included in the present version of the GCVS. There exist period determinations for 5 stars in our catalog, none of which are classified as BY in GCVS: sources #55, #204, #256, #435, #448. Because of this we do not use the period determinations in GCVS in this work. GCVS also includes a new secondary classification that was added "(...) upon recommendations of the IAU Commissions 27 and 42, in 2006"[8] but only 9 sources have such a classification. These are all T Tauri sources which have been reclassified from INT or IT to classical T Tauri or weak T Tauri (see section 1.2.1) but one source - 438, AB Aur -which was reclassified from INA to a Herbig AeBe star, the massive counterpart to the T Tauri. Because this new classification does not add much to the original classification we do not use it in this work. Finally, GCVS also has a file in addition to the catalog which has remarks on specific sources, but not all sources have remarks[9].

---

[8] See "Note on VarTypeII" in the following url `http://www.sai.msu.su/gcvs/gcvs/gcvs5/htm/`

[9] remarks.txt can be accessed through the following link:`http://www.sai.msu.su/gcvs/gcvs/gcvs5/`

Chapter 4

Observational Data and Catalogs

The cadence and time span of the data we choose set the sort of phenomena that we are able to detected. Because we want to study the long term variability of the low mass stars and brown dwarfs in Taurus we are most interested in acquiring multi-epoch photometry over as large a time span as possible. The Zwicky Transient Facility (ZTF) provides data covering a time span of over 3 years (see Section 4.1), with two available bands, g and r, and the AllWISE survey offers multi-epoch photometry in at least two bands, W1 and W2, with a cadence of hours over two days separated by ∼6 months (see Section 4.2). We employ data from both surveys in this work in order to understand how the variability of the sources in Taurus SFR affects each wavelength range. In this Chapter we describe the properties of each survey, how the data was acquired and then present the light curve data for the Taurus SFR and its properties.

4.1 Zwicky Transient Facility

The Zwicky Transient Facility (ZTF) (Masci et al. 2019; Bellm 2014) is a high cadence optical survey using the 1.2m Palomar telescope in San Diego County, California. It employs new technology to improve upon its predecessor, the Palomar Transient Factory (PTF). In contrast to PTF, the new camera of ZTF now fills the entire focal plane of the Palomar telescope, which enabled it to improve survey speed in 3 orders of magnitude; this is achieved through higher quantum efficiency and reduced time between exposures. The new camera has a field of view of 55.0 deg^2 with an active area of about 47.7 deg^2 and provides image quality of about $2''$ FWHM across all three band, g (480.48 nm), r (643.69 nm) and i (796.82 nm) - see Figure 4.1, which shows the transmission curve for the ZTF g, r and i bands. This provides 5σ sensitivity up to $g = 20.8$, $r = 20.6$ and $i = 19.9$, respectively, in 30 second exposures (public survey only, private survey data can have different exposure times) across the 16, $6144p \times 6160p$, CCD[1] array. The saturation limit for ZTF is found to be between 12.5 to 13.2 mag for all filters and CCD-quadrants[2]

The main ZTF science drives are all connected to its high cadence capabilities: detection of supernova, fast decaying transients such as the optical afterglow of gamma rays burst events and variability studies. For stellar variability studies, ZTF can help to identify variables in their three bands, g, r and i. With these three bands it is possible to probe many different

---

[1] Charged Coupled Device

[2] This information can be found in the ZTF Science Data System Explanatory Supplement: `https://irsa.ipac.caltech.edu/data/ZTF/docs/ztf_pipelines_deliverables.pdf`

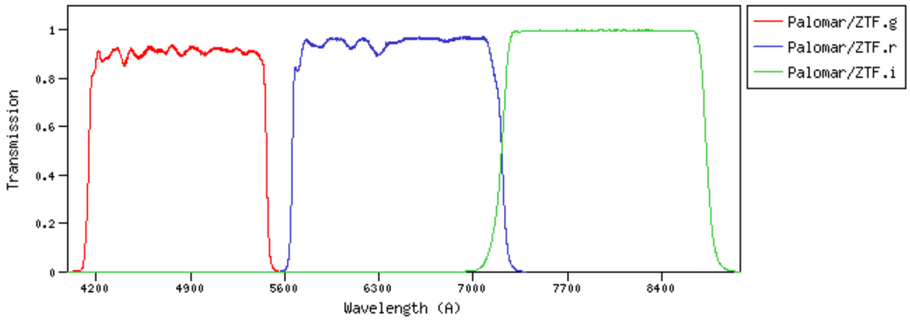

Figure 4.1: *On-axis filter transmission for the ZTF g, r, and i-band filters. Full credit to the Spanish Virtual Observatory, which can be accessed through the following URL:* `http://svo2.cab.inta-csic.es/theory/fps/`

phenomena known to occur in young variables as the ones we know exist in Taurus. The ZTF g is the most sensitive of the three ZTF bands to variations produced by variable extinction (due to being the shortest wavelength band; see the discussion on variable extinction in Section 6.1), while the ZTF r, which encompasses H_α (656.28 nm; see Figure 4.1 and the discussion on variables accretion in Section 6.1), should be more sensitive than g to variations due to variable accretion.

We employ the 6th data release from ZTF[3] (Masci et al., 2019) (hereforth, ZTF DR6) which encompasses data from 17/03/2018 (MJD $\geq$ 58194.0) to 2021-04-30 (MJD $\leq$ 59334.0) with yearly breaks of 1-3 months. This release has data from both the public survey and the private surveys that reach the end of their 18 month proprietary period. i-band data is limited to the private surveys and these can also have data with longer exposure times while the public survey is limited to 30 s. The cadence of the data can also change between data from both programs. ZTF is a high cadence instrument which has been used thus far to detect and characterize plenty of sources which present fast variability (eg. van Roestel et al. (2021)). However, for the data gathered in the public survey the cadence is expected to be between 1-3 days, with some exceptions associated with overlapping fields and some private data which is routinely added to the public set.

4.1.1 Matching and data overview

We used the ZTF DR6 to match coordinates within a radius of 1$''$ with our catalog of YSO members of Taurus SFR. The Taurus members catalog which we describe in Section 3.2 was matched through the Infrared Science Archive (hereforth, IRSA) by querying the ZTF DR6 catalog query[4] yielding 1336 matches. These matches exceed our number of members because each match corresponds to different sets of measurements taken with ZTF. So for example, for each source, a number of measurement sets are available which correspond to photometry in different fields and epochs. Because of this we are required to match each of these measurement sets to each of the sources in our catalog. Doing this, we obtain light curves for 386 sources. No *i-band* data was available but most (309) of the sources have information on both g (343) and r (352) bands. The set of 105 sources which did not match are composed of two populations: bright sources with G magnitudes smaller than the saturation limit of ZTF ($g \sim 12-13$) and

---

[3] Information on the ZTF DR6 can be found in the following link: `https://www.ztf.caltech.edu/page/dr6`

[4] https://irsa.ipac.caltech.edu/cgi-bin/Gator/nph-scan?submit=Select&projshort=ZTF

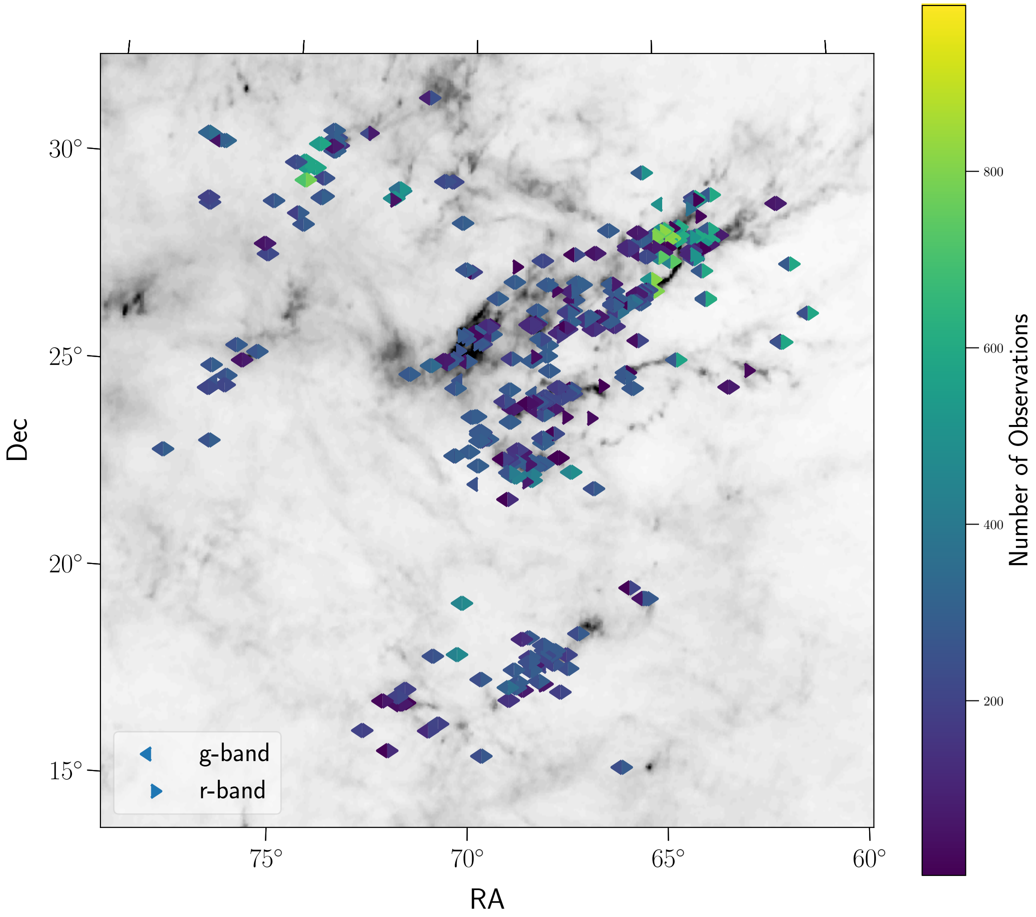

Figure 4.2: *Planck HFI 857GHz dust map (Planck Collaboration, 2016) with the sources matched in either g (left pointing triangle) or r (right pointing triangle). The color of the symbols indicate the number of observations in each band and the corresponding color bar is shown on the right.*

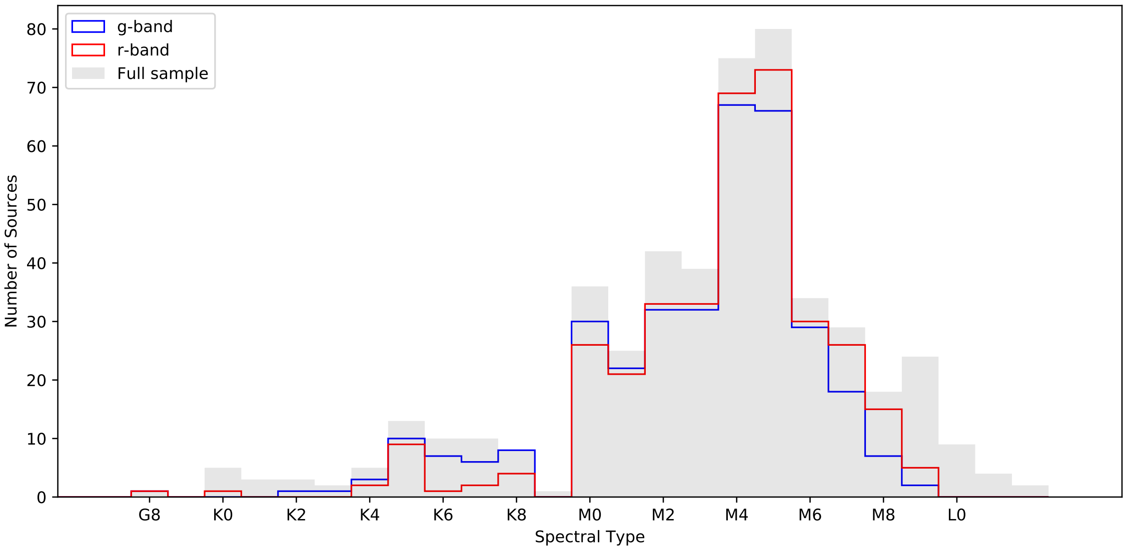

Figure 4.3: *Distribution of the spectral types in the ZTF DR6 set for sources matched in either g (blue step) or r. Filled grey histogram represents the full sample of Taurus YSOs. One source of spectral type A0,#70, also matched but was left outside of the plot for better clarity.*

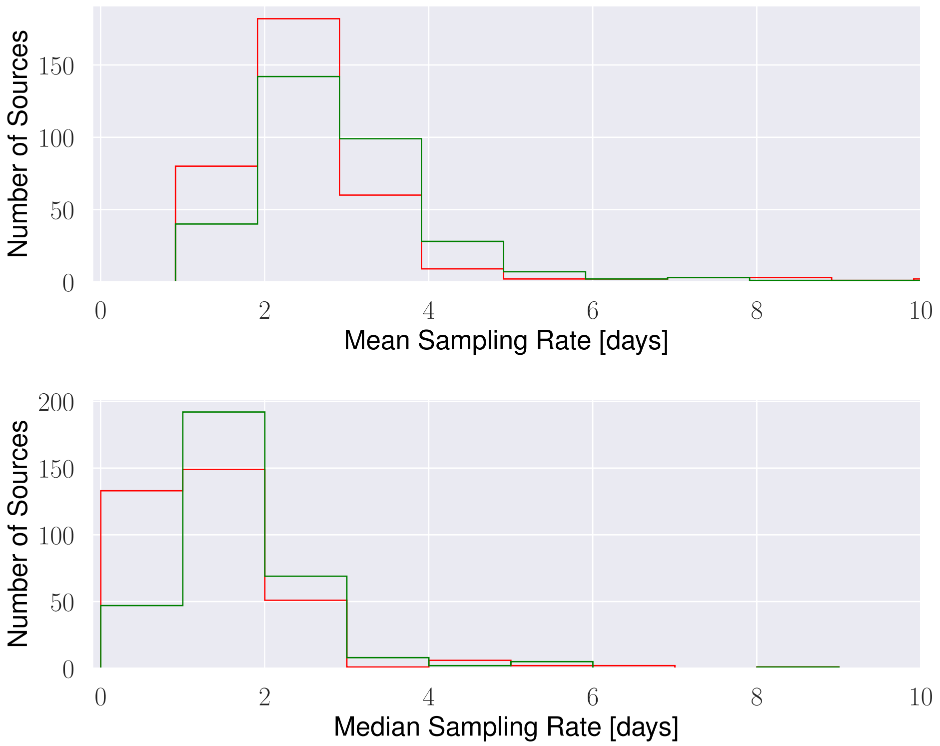

Figure 4.4: *Mean (top panel) and median (bottom panel) sampling rates of g (green) and r (red) light curves in the ZTF DR6. The median better illustrates the common cadence between two random consecutive measurements, which peaks between 1-2 days. The mean sampling rate peaks between 2-3 days, showing that in any ZTF lightcurve the cadence is not constant throughout the time span of the data. These calculations do not take into account the separation of* $\sim$ *2 months which exists for all data during the yearly maintenance period of ZTF.*

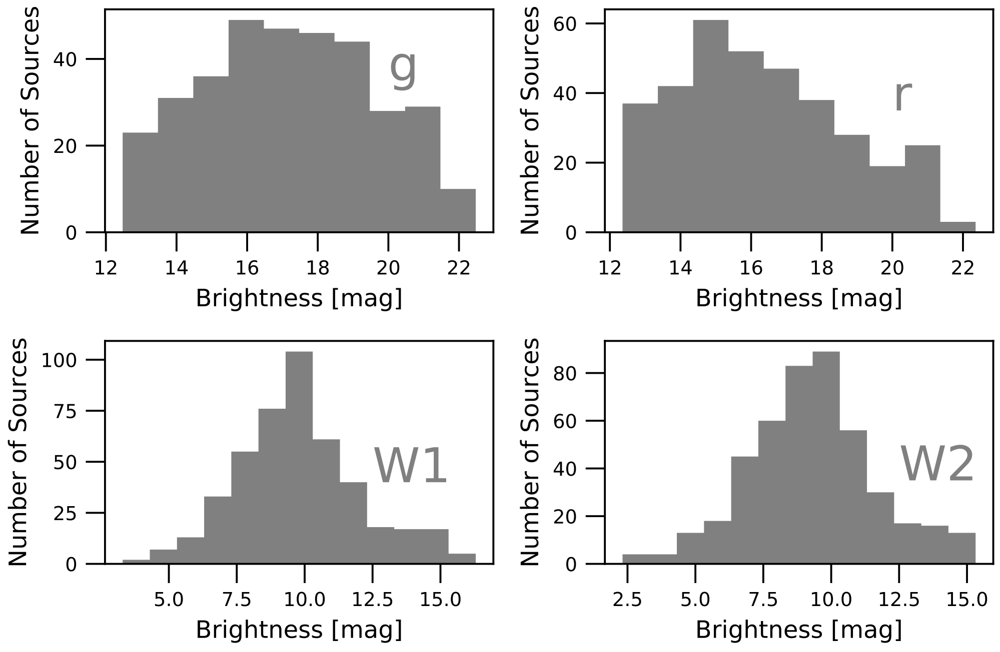

Figure 4.5: *Distribution of mean brightness in r, g, W1 and W2 for the sources matched in ZTF DR6 and AllWISE surveys.*

faint extinct sources which are not detectable at least in the usual 30 s exposures of the public survey.

Under ideal conditions, if every source in our catalog were sampled every 4 days during one year, we would expect the light curves to have about 90 data points, or somewhat less if we take into account yearly maintenance, which ZTF exercises for ∼2 months per year. Therefore, we would expect between 200-300 measurements in each light curve during the 3 years of data which exist for Taurus SFR. In Figure 4.2, a sky map of the Taurus sources color-coded by the number of observation points is presented, and we see that in fact most sources seem to present more than the expected number of measurements. Most sources seem to have more than 200 data points in either band (214, 62% in g and 255, 72% in r) with only some (29, 9% in g and 66, 19% r) having more than 400. In g, 8 sources 2 measurements or less in their light curves and in r only 3; these data for these sources is not employed in our analysis. Figure 4.3 shows the distribution of the spectral type for the sources matched in either g or r. We see that most of the M stars have light curves in both bands while the more massive stars G-K stars show a higher fraction of sources with data in only one band, when compared to the M dward population. Few sources of spectral type M9 have data in ZTF at all and no L type brown dwarf exists in the ZTF data set. Of the A/B stars in our sample, only one matched in ZTF, #70, an A0 star.

To investigate the actual cadence of the ZTF data we created histograms of the median (bottom panel) and mean (top panel) sampling rate, which are shown in Figure 4.4. From these plots we find that the most common timestep between two random consecutive measurements should be lower than the expected cadence from the literature. However, because the mean histogram peaks at higher values than the median histogram we find that there must exist higher timesteps which differ significantly from the expected cadence.

4.1.2 Light Curves

Figure 4.5 shows the mean brightness in g and r (top row) determined from the light curve data. We find no sources with mean brightness higher than the quoted saturation limit but some sources are detectable below the expected brightness limit in the ZTF literature ($g > 20.8$ and $r > 20.6$). To have a better understanding of the light curves in Taurus SFR, that is: how the brightness variations look in the light curve; if they present specific shapes; etc. We decide to perform a visual inspection onto the full data set to find specific features, which we define as different visual phenomena with common characteristics which can appear in different light curves. After visually inspecting the light curves, we are able to identify the following features:

- Visual burst (VB): an increase in brightness which then returns to the quiescent value. Usually sources present many VB events throughout their light curve but some sources have higher amplitude and duration VB events which occur over the whole time span of the light curve. **These are the most common type of feature in the Taurus ZTF light curves.**

- Visual dip (VD): a decrease in brightness which then returns to the quiescent value. VDs are usually longer than VB events, and are also less common and tend not to appear in the same light curve as many times.

- Quasi-Periodicity: Sometimes a sequence of VB or VD events might look to obey some periodicity law, at least locally.

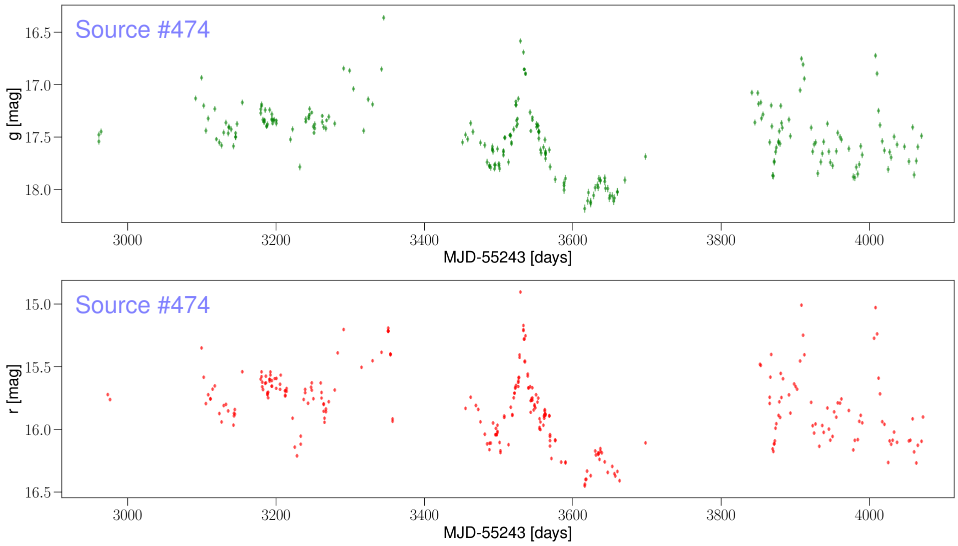

Figure 4.6: *ZTF light curve for source #474, the source presenting multiple VBs in both g and r. Top panel is g and bottom panel is r.*

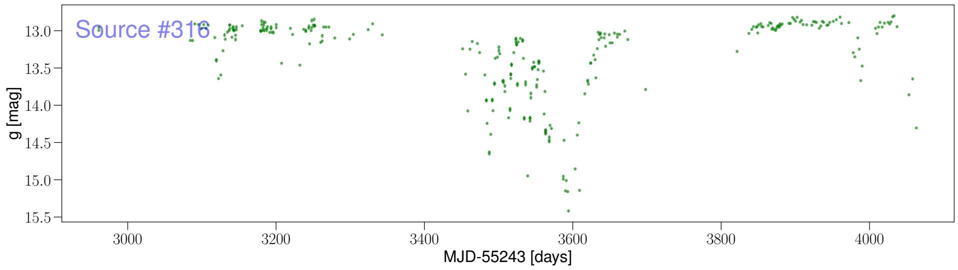

Figure 4.7: *ZTF light curve for source #316, the source presenting a large VD in g. No data for this source in r.*

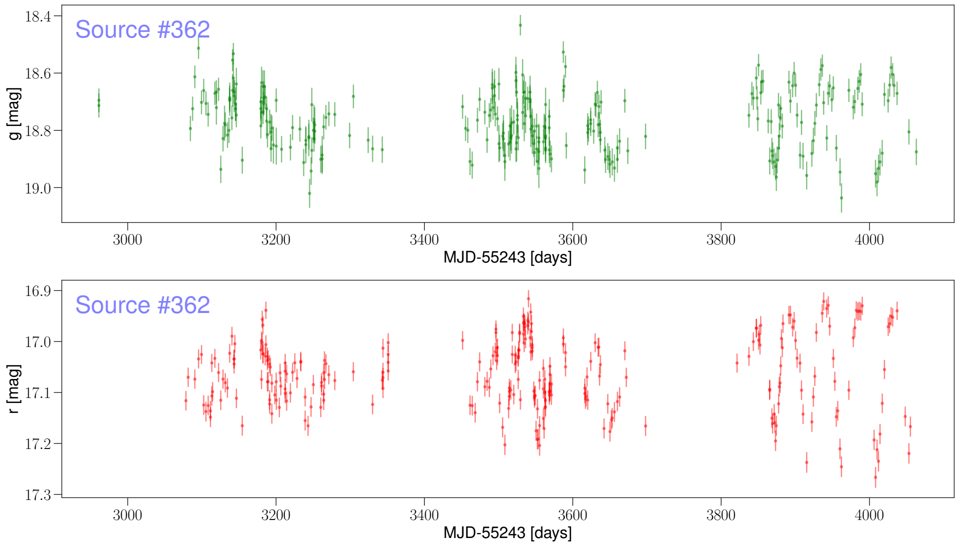

Figure 4.8: *ZTF light curves for source #362, the source presenting quasi-periodicity in both ZTF g and r light curves, specially in the third year of data. Top panel is g and bottom panel is r.*

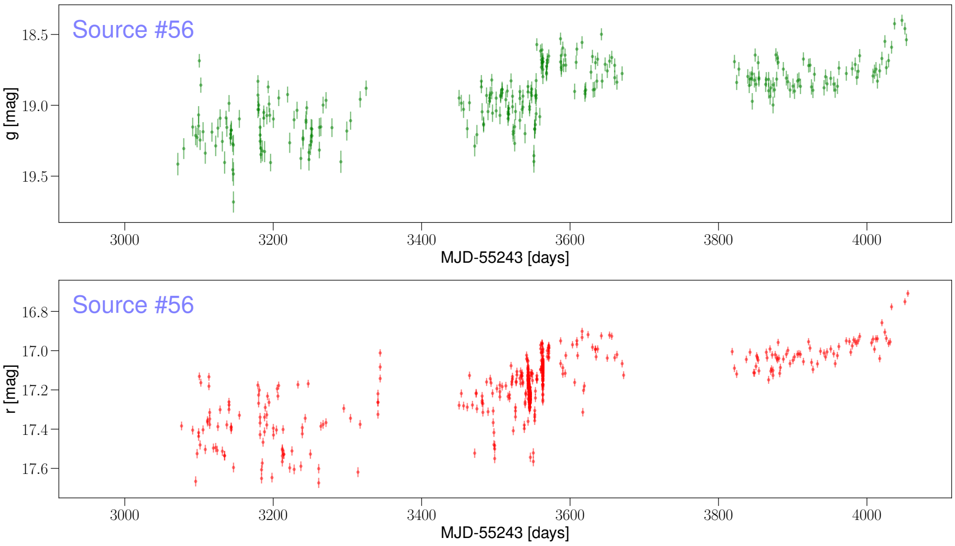

Figure 4.9: *ZTF light curve for source #56, the source showcasing long timescale phenomena in both ZTF g and r light curves. Top panel is g and bottom panel is r.*

- Long Timescale: some sources show a continuous change in their average magnitude over time which does not seem related to the local VD/VB events.

Figures 4.6-4.9 shows light curve examples for each of the aforementioned visually determined classes, while Figure 4.10 shows the on-sky distribution of all sources with visual classifications and presents the number of sources classified in each of the different classes. As stated above, VB is the most common visual feature. Some sources show VB activity which is also linked to fast variability (**S** class in GCVS). This causes the feature in the light curve to be badly sampled with only a few data points covering the event. Other sources show well sampled Gaussian like VBs which differ on their amplitude and duration. Source #474 in Figure 4.6 shows the latter of these behaviours (well sampled Gaussian-like curve). VDs are the second most common type of visual feature in the ZTF light curves. Like VB events, VDs can also be detected as clear well sampled features or through outlier like data points, both of which can be seen in the ZTF light curve for source #316 (see Figure 4.7). Long timescale phenomena is the third most common feature in the ZTF light curves and is associated with a continuous or discontinuous change in the mean magnitude of the star over the time span of the light curve; source #56 in Figure 4.9 shows an increase of brightness over the whole g/r light curve, which takes it from $g \sim 19.5$ to $g \sim 18.5$. Finally, we have looked at the possibility of quasi-periodicity in the ZTF light curves and have found some (5) promising light curves. One such light curve is that of source #362 which is possibly a brown dwarf (M7) showing some sort of clear periodic phenomena in the third year of ZTF data. From this analysis we find that it is possible for a source in the ZTF data to present more than one of the aforementioned features.

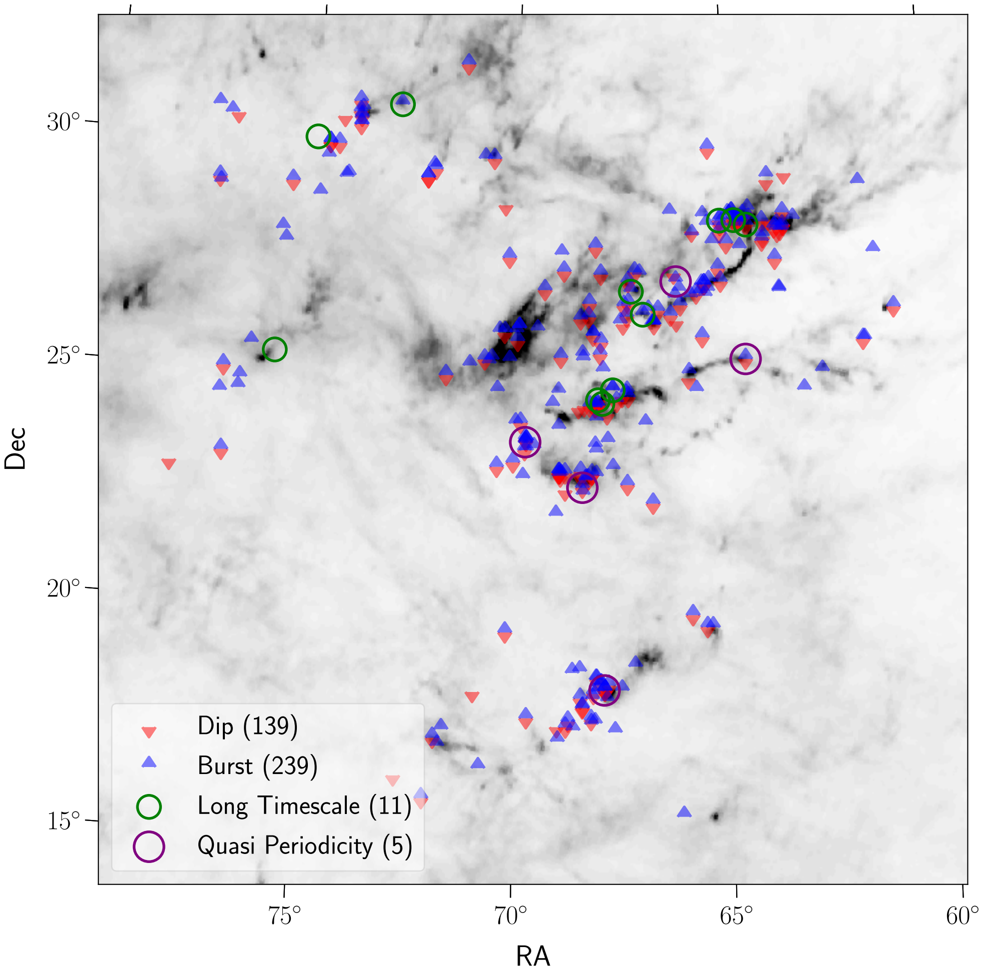

Figure 4.10: *Planck HFI 857GHz dust map (Planck Collaboration, 2016) with with visual classification marked (see Section 4.1.2).*

4.2 AllWISE

The Wide-field Infrared Survey Explorer (WISE; Wright et al. 2010) is a 40 cm telescope which is in a Sun-synchronous orbit. It surveys the entire sky in the 3.4, 4.6, 12 and 22 μm mid-infrared bandpasses (hereafter W1, W2, W3 and W4; see Figure 4.11 for the transmission curve information), taking 8.8 s exposures of a $47' \times 47'$ field. As WISE is a telescope observing in the infrared, it needs to be maintained at low temperatures in order to minimize the possible contaminants of thermal radiation. Because of this, after both cryogen tanks which cooled the satellite had depleted, a new survey continued until April 2011 in the called Post-Cryo Phase but only in the first two channels, W1 and W2, and with a new focus on solar system science. This is the NEOWISE (Mainzer et al., 2011) survey, which aimed at enhancing the processing system of WISE in order to detect and archive data related to Near Earth Objects (NEOs). In 2013 a new catalog called AllWISE (Cutri et al., 2021) was created from the archival data from both WISE and NEOWISE. The AllWISE catalog is composed of 4 main data products: the AllWISE Source Catalog, the AllWISE Images Atlas, the Rejects table and the AllWISE Multiepoch Photometry Database (MEP).

In the Cautionary Notes[5] regarding the multi epoch photometric data in the AllWISE release, it is described that this table features data for sources featured in both the AllWISE source catalog and the rejects table. Therefore, some sources might have redundant duplicated measurements which are a result from "(...) objects in the overlap region between Tiles or that are part of small-separation, same-Tile duplicate groups (...) [being] detected and extracted more than once during AllWISE Multiframe processing."[6]. These duplicated measurements were excluded from the source catalog but are present in the MEP. This can be due to these publicly available light curves being used as a tool to investigate the flux history of source in the AllWISE Source and Reject tables and for probing the same sources for follow up light curves.

---

[5] https://wise2.ipac.caltech.edu/docs/release/allwise/expsup/sec3_2.html

[6] This is described more in depth in the following online article: https://wise2.ipac.caltech.edu/docs/release/allwise/expsup/sec5_4.html

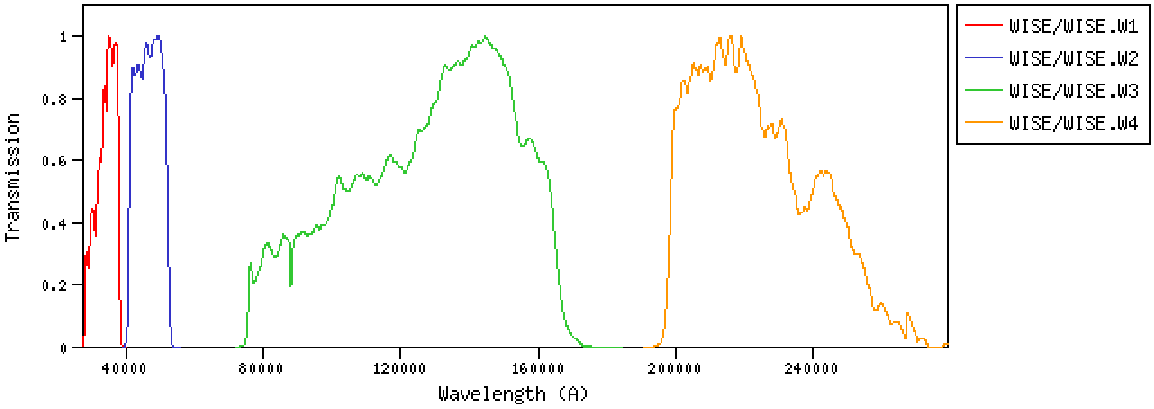

Figure 4.11: *On-axis filter transmission for the WISE W1-W4 bands. Full credit to VSO.*

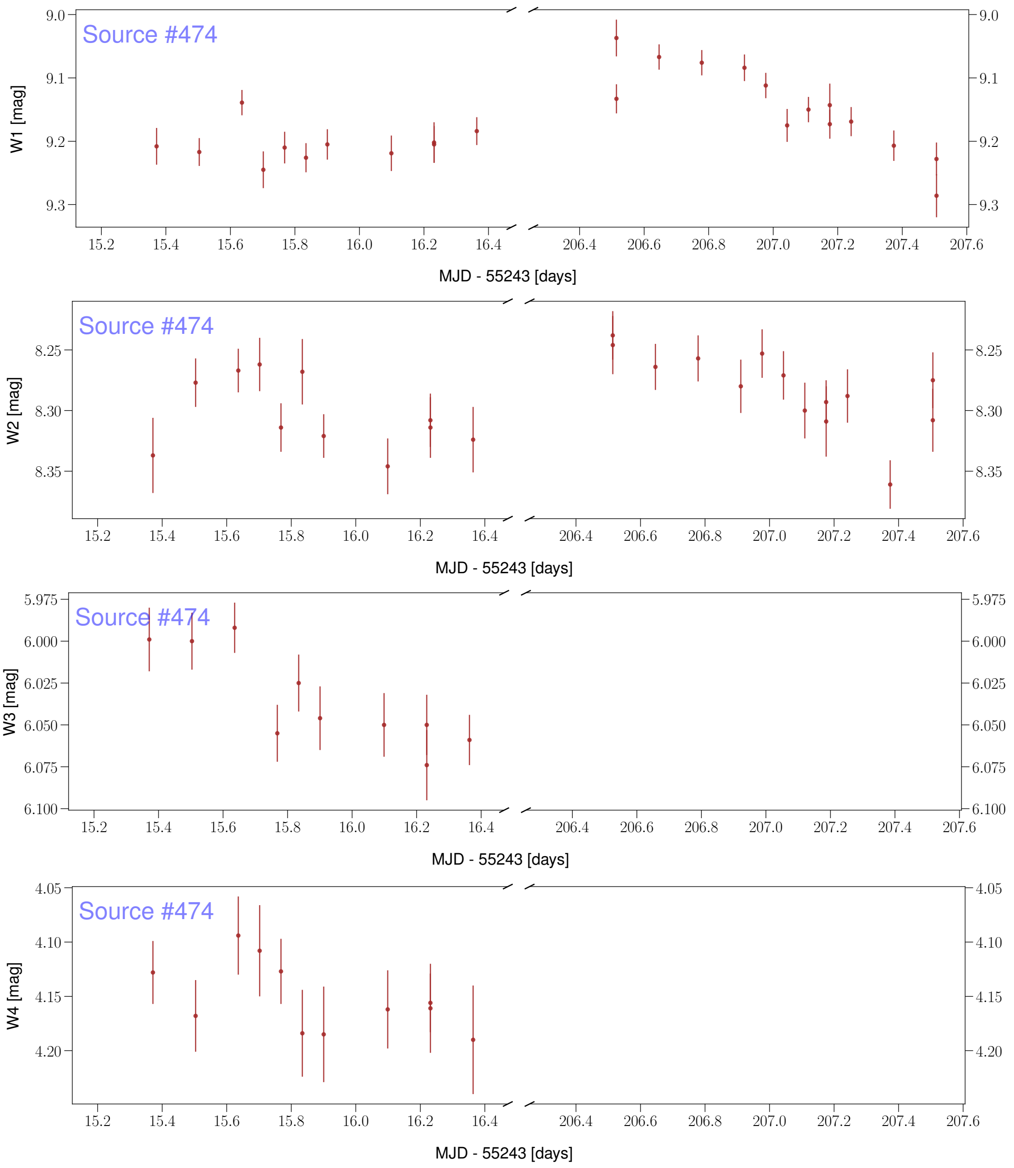

Figure 4.12: *AllWISE light curve for source #474, the source presenting multiple VBs in the ZTF g and r light curves. From top to bottom, W1, W2, W3 and W4.*

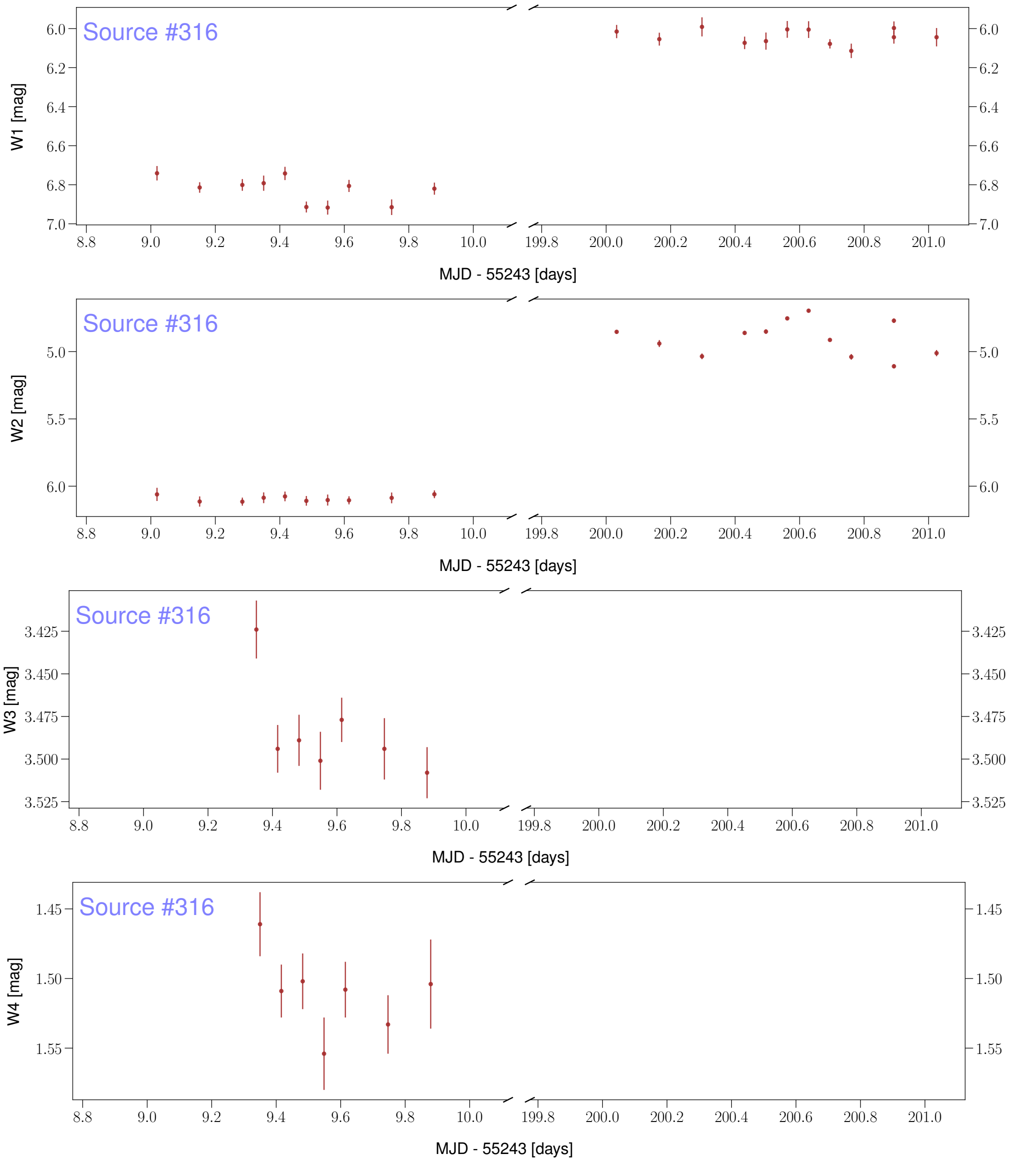

Figure 4.13: *AllWISE light curve for source #316, the source presenting multiple a large VD in the ZTF g light curve. From top to bottom, W1, W2, W3 and W4.*

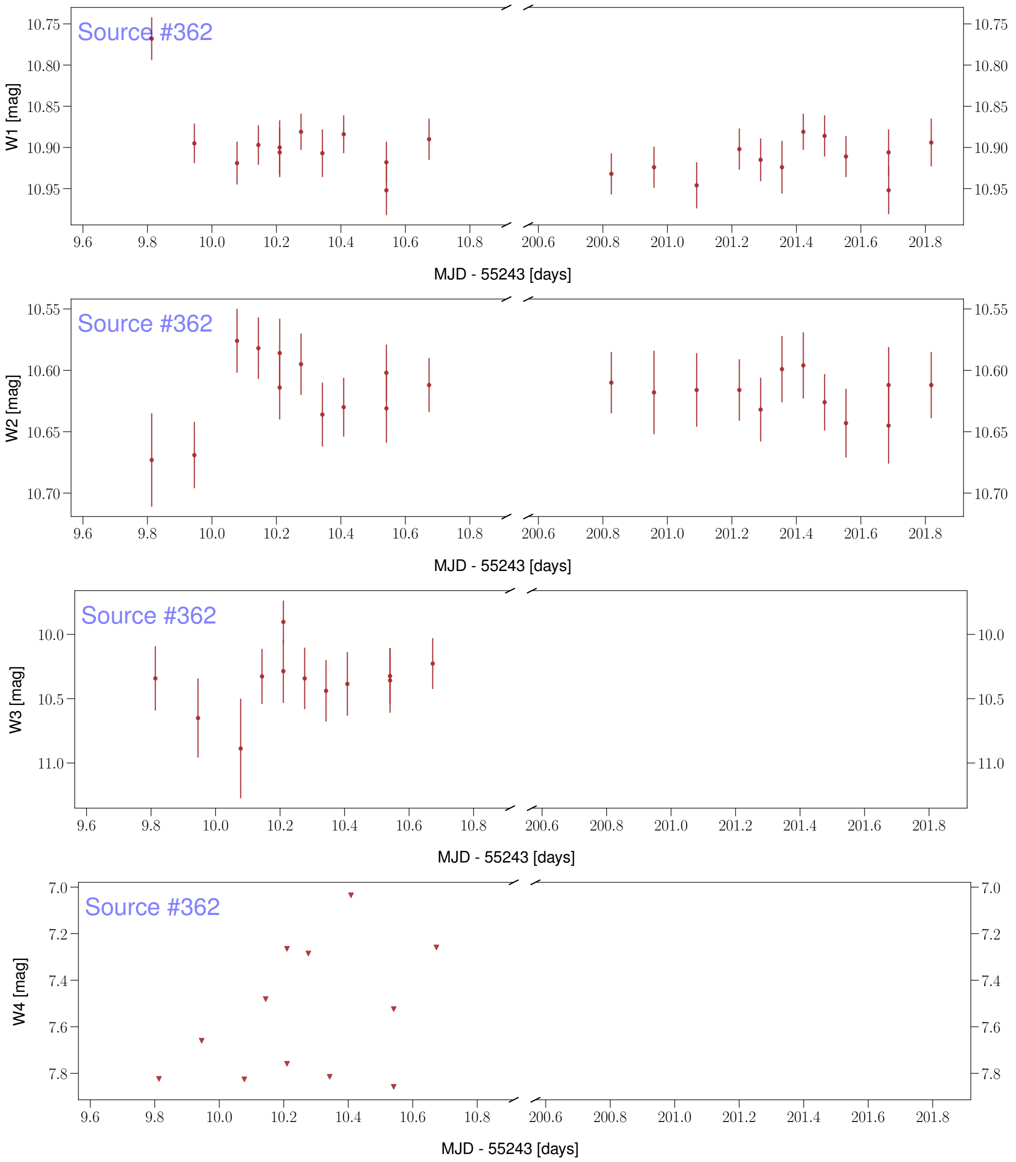

Figure 4.14: *AllWISE light curve for source #362, a possible BD (spectral type M7.5) presenting quasi-periodicity in the ZTF light curve. From top to bottom, W1, W2, W3 and W4.*

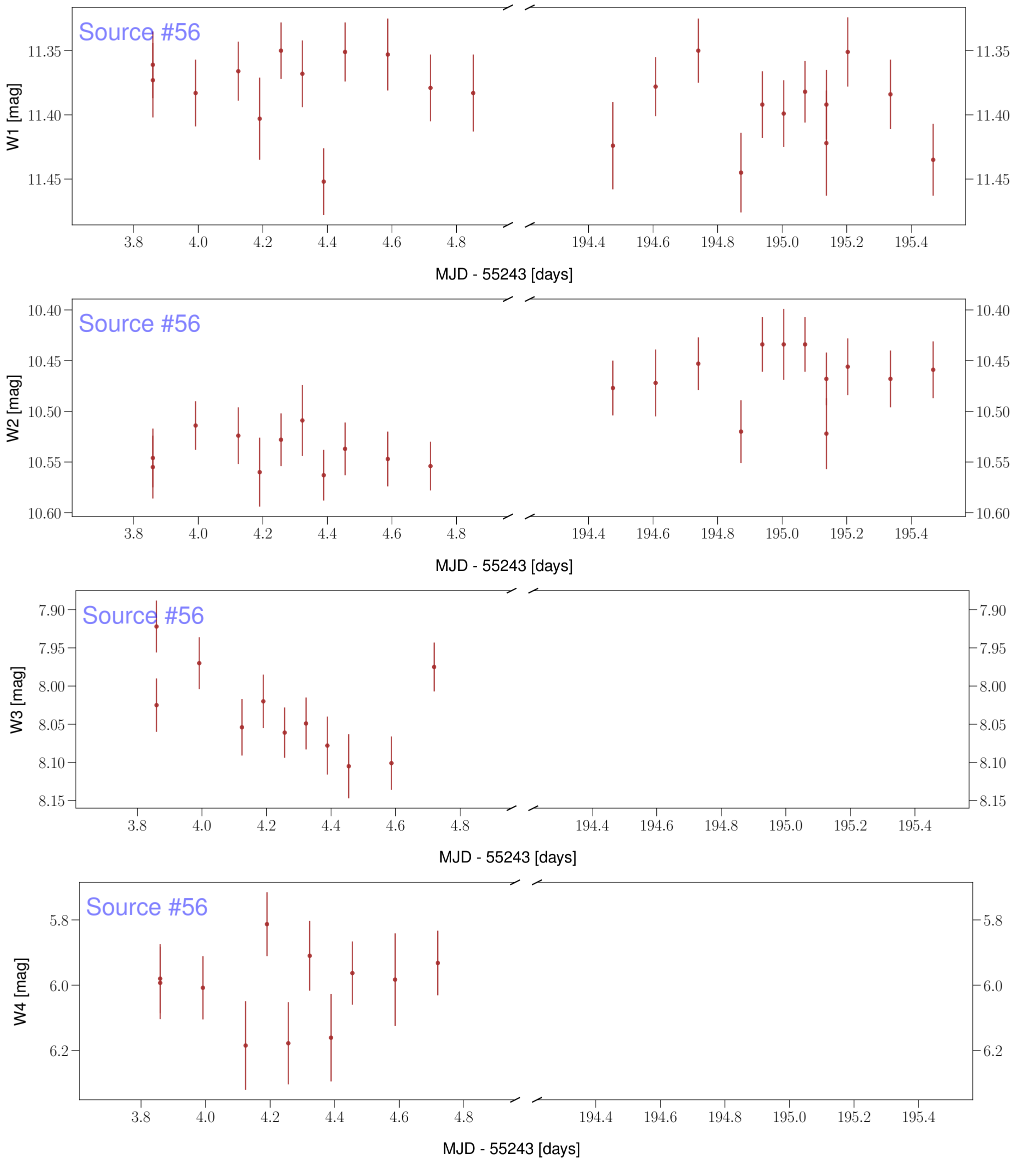

Figure 4.15: *AllWISE light curve for source #56, the source presenting long timescale phenomenon in the ZTF light curves. From top to bottom, W1, W2, W3 and W4.*

4.2.1 Matching and Data Overview

We matched with the AllWISE MEP through the IRSA services and, as for ZTF, we matched the table with our catalog of YSOs obtaining 448 matches within $1''$. The duplicate values which were mentioned in the Cautionary Notes are removed through a 'cat' flag present in the long format of the MEP table in IRSA, which separates measurements from the Source Catalog and the Rejects table. After this removal, 3 sources, (#7, #48 and #82) still presented more than 40 measurements which after visual inspection corresponded to duplicated values associated with the Source Catalog. We search for data points with exactly the same MJD and photometry and remove the extra values. Finally, there are measurements which lack associated uncertainty that we plot in the light curves with the pointing down triangle symbol, but are excluded from the statistical analysis.

After the cleaning of the AllWISE data, we find that 380 (85%) sources have more than 20 measurements in W1 while only 1 source has 10 measurements or less. In W2, 321 sources (72%) have more than 20 measurements and 33 (7%) have 10 or less.

4.2.2 Light Curves

The AllWISE MEP data consist of two sets of measurements, each with about 12 measurements with a cadence of few hours, which are separated by almost 200 days. To detected variability in this data set we use W1 and W2 because these bands are always available in the two days of data, however the possibility of having MIR data in 4 different bands (albeit only in one day of observations) enables us to explore the variability of the disk classification as explained in Section 2.1. Of the 448 sources matched, 434 (97%) have photometry in all 4 bands in the first epoch, and of those 321 (72%) have uncertainties associated with said measurements. Unlike the ZTF data, AllWISE light curves are much less sampled and particular features may be somewhat difficult to visually distinguish, but can still be identified. Figures 4.12-4.15 shows the AllWISE light curves for the same sources presented in the ZTF light curves. In the top two panels in Figure 4.13 we can see the effect of an increase in brightness from pre-cryogen data to the post-cryogen data. In Figure 4.14 we see that there is a burst in the pre-cryo data for W1 and a simultaneous dip in the same time frame for W2; this visual feature also seems to repeat itself in the post-cryo light curve.

Using the fact that we have data separated by $\sim$ 6 months, we investigate how many of our AllWISE sources showcased long term variability by checking how many had an increase of over half a magnitude in both W1 and W2 from one day of observations to the next. We found 7 such sources in W1 [16, 19, 106, 202, 316, 321, 395] and 4 in W2 [19, 250, 265, 316]. From the W1 set, sources #202 is classified as *Long Timescale* in ZTF while #321, #395 and #316 have other classifications and the rest are not present in the ZTF data. In the W2 set there are no sources classified as *Long Timescale* in ZTF, however sources #250, #316 and #265 have other classifications (the two latter sources do show large amplitude variations in ZTF) and the rest is not present in the ZTF data.

4.3 Taurus Variable YSO Atlas

In the ZTF data set we were able to get light curves for 386 members, of which 304 have a light curve in g **and** r. In AllWISE we have 448 light curves for each band (W1-W4). In addition we

create CMDs as explained in Section 6.5 for every source, when possible, and for the AllWISE data we also create plots showing the variation of the YSO class over the available time span. To better organize our work and for future researchers to be able to fully investigate the variability of specific sources in the Taurus Clouds, we compiled the *Atlas of the variability properties of young stars and brown dwarfs in Taurus* (hereforth simply atlas). For each star we create 5 pages with information of its photometric and variability properties. The full description of the atlas can be found in the appendix on this thesis and is also present in the first 6 pages of the atlas itself as a way to easily find plot and data description as well as the relevant references. Here we briefly describe the information present in each entry, but encourage the reader to read the full description in the appendix.
The sources present in the atlas are the same 491 sources described in Chapter 3 and we kept the numbering from 1 to 491 sorted by ascending Right Ascension. The Atlas will be available online, following publication, through GitHub:
`https://github.com/AfonsoDoVale/Taurus-Variability.git`.

Coordinates, photometry, spectral type and variability type

In the first page of each entry we present coordinates for each star along with their sky position on top of a Planck 857GHz dust map. The coordinates presented are from Gaia eDR3, 2MASS or UKIDSS. References for the coordinates for each star are present in all catalogs available in the GitHub repository in the column {rPos}. eDR3, 2MASS and UKIDSS are the keywords which associate the coordinates to the aforementioned references, respectively.
We also present Gaia eDR3 G brightness, JHK brightnesses from Esplin and Luhman (2019), median g and r brightnesses from ZTF DR6 data, and median W1 and W2 brightnesses from AllWISE MEP. The spectral type presented is from Esplin and Luhman (2019) and the variability type is from the GCVS5.1 (see section 3.2.2).

Light Curves

In the atlas we present ZTF and AllWISE light curves for the data employed in this thesis. For ZTF, g and r light curves for the full timespan of the data as of DR6. For AllWISE, W1-W4 light curves for the two days of data. The first day has data in all 4 WISE bands while the second day, post-cryo data, only has data in W1 and W2.

Color-magnitude diagrams

From the work presented in Section 6.5 we have created CMDs showing the trajectories that sources map over time because of their brightness variability. We have such plots for each source with data in two bands, either in ZTF DR6 or AllWISE. From the ZTF data we present in the atlas the CMD for the full timespan of the data (3 years) and also 3 more for each yearly set of data. For AllWISE we present the CMD for both days of data, one for the cryo data and another for the post-cryo data. Each of these CMDs has an extinction vector created from the extinction law by Cardelli et al. (1989). Each CMD also presents a stellar isochrone for an age of 3 Myr and a distance of 140 pc built from a combination from PARSEC (Bressan et al., 2012) ($1M_\odot < M_*$), BT-Settl (Allard et al., 2011) ($1M_\odot > M_* > 0.1M_\odot$) and AMES-Dusty (Allard et al., 2001) ($M_* < 0.1M_\odot$). More information on the extinction and isochrones employed can

be found in the atlas description in the appendix.
Additionally we also present in the atlas G, (Bp-Rp) CMDs using the Gaia eDR3 photometry and H, (J-K) CMDs from the JHK photometry present in the catalog of Esplin and Luhman (2019).

YSO class determination and changes over time

Finally, from the work presented in Section 6.4 we also have determined the YSO classification slope for each epoch with data in W1-W4, during the cryo data in AllWISE. In the atlas we present, for each source with at least one available set of measurements in W1-W4, a plot showing the data and the determined fit and another plot showing how the YSO classification slope changes for the different epochs in which there is data. More information on these plots and how they are presented can be found in the atlas introduction in the thesis appendix.

Chapter 5

Finding Variable Sources in Taurus

Detection of variability in stellar light curves is not as simple as one may naively expect it to be. What are the criteria that one should adopt in order to say that a stellar source is indeed variable? How can we then classify a source as variable? How do we implement algorithms to find out if these criteria are met in specific light curves of stellar objects? In the following chapter we will try to answer these questions by introducing some of the most useful and important algorithms which have been used for the past decades for this exact purpose. As Sokolovsky et al. (2017) describes these methods, he separates them into two distinct categories: scatter-based indices and correlation-based indices. The differentiation comes from the fact that correlation-based indices take into account the order in which the data was taken and some even consider the time difference in between observations. Scatter-based indices, on the other hand, only consider the distribution ofF the measured magnitudes and their estimated errors, thus ignoring the temporal information on the light curves. For this analysis we employ the same distinction between the variability indices.

In order to analyze the properties of the variable population of Taurus YSOs we employ a set of both correlation and scatter-based indices to get the largest possible set of bonafide variables. From the distribution of the results of each index we determine a *cut-off* which will differentiate between variables and non-variables. Some indices can work better than others on different data sets that we have acquired for this work (see Chapter 4), thus defining a reliable *cut-off* can sometimes be challenging. This is due to the properties of the data and the algorithm of the index itself. In this chapter the different variability indices which we employ are presented to the reader along with their performance on the ZTF and AllWISE data. The methodology used to define a Taurus YSO as a variable will also be presented and finally the results on the application of said method on the ZTF and AllWISE data, which define our set of optical and MIR variables.

5.1 Variability Indices

5.1.1 Scatter-based indices

Chi-squared (χ^2)

A χ^2 test is a statistical test in which the sampling distribution of the test statistic is compared to a χ^2 distribution. If the sampling distribution is a χ^2 distribution, then the null hypothesis H_0 must be true (Sokolovsky et al., 2017; Carpenter et al., 2001). If we set H_0 as the hypothesis that a stellar source **does not** change its brightness, we are able to compute its χ^2 statistic from a light curve with N magnitude measurements m_i and the corresponding errors σ_i through the following formula:

$$\chi^2 = \sum_{i=1}^{N} \frac{(m_i - \bar{m})^2}{\sigma_i^2} \tag{5.1}$$

Where $\bar{m}$ is the weighted mean magnitude value for each light curve given by:

$$\bar{m} = \sum_{i=1}^{N} \frac{m_i}{\sigma_i^2} / \sum_{i=1}^{N} \frac{1}{\sigma_i^2} \tag{5.2}$$

Two very important criteria need to be met for a χ^2 to be statistically significant: the N measurements need to be independent from each other and the corresponding errors have to be symmetric. When using the magnitude scale, which is logarithmic, the errors are by default asymmetrical. The χ^2 test should be applied in the flux space where the errors do meet the criteria (Andrae et al., 2010) but Sokolovsky et al. (2017) mentions that, regardless, this index can be useful as a simple measure of scatter in the data and in fact it has been used in variability studies to that effect (e.g. Rebull et al. 2014; Carpenter et al. 2001). If these two criteria are met, the computed χ^2 value can be compared to the critical value $\chi^2_{p,N-1}$ obtained from the χ^2 distribution with N-1 degrees of freedom. To use the approach of Carpenter et al. (2001), a sampling distribution of these computed χ^2 is required. Because the light curves from ZTF and AllWISE do not all have the same number of observations, different χ^2 values would not be comparable to each other without a normalization done beforehand. We employ the reduced form of χ^2, χ_{red} :

$$\chi^2_{\text{red}} = \frac{\chi^2}{N-1} \tag{5.3}$$

Summarizing:

- Strengths: Easy to compute. Well known and easily understood.
- Limitations: Can only be applied to one data set. Will not detect low amplitude variables.
- Requirements: Errors must be symmetric.

Weighted Standard Deviation

Variable sources should by definition have larger scatter in their light curves than non-variable sources. Another way to measure this scatter is by computing the standard deviation,

$$\sigma = \sqrt{\frac{1}{N-1} \sum_{i=1}^{N} (m_i - \bar{m})^2} \tag{5.4}$$

or its weighted version,

$$\sigma_w = \sqrt{\frac{\sum_{i=1}^{N} w_i}{\left(\sum_{i=1}^{N} w_i\right)^2 - \sum_{i=1}^{N} \left(w_i^2\right)} \sum_{i=1}^{N} w_i \left(m_i - \bar{m}\right)^2} \tag{5.5}$$

where $\bar{m}$ is the mean magnitude computed as in equation 5.2 and $w_i = 1/\sigma_i^2$ is the weight which maximizes the likelihood of obtaining the set of measurements m_i from a Gaussian distribution of variance σ_i^2.

- Strengths: easy to compute, easy to interpret.
- Limitations: Sokolovsky et al. (2017) points out that this method is relatively sensitive to outlier points and suggests that a filtering of the light curves be applied before usage of this method in the search for variability in light curves.

Amplitude: Dip and Burst

Our last scatter-based index is the amplitude of the light curves in respect to the mean magnitude value. We employ the **burst amplitude** (hereforth A_{burst}),

$$A_{burst} = \max m_i - \bar{m} \tag{5.6}$$

and the **dip amplitude** (hereforth A_{dip}),

$$A_{dip} = \bar{m} - \min m_i \tag{5.7}$$

where again, $\bar{m}$ is given by equation 5.2.

- Strengths: Easy to compute and interpret. Units are brightness and can point to the sources with largest increases and decreases in their average brightness.
- Limitations: This method is very sensitive to outliers.
- Requirements: one data set.

5.1.2 Correlation-based indices

Welch-Stetson I

Welch and Stetson (1993) proposed a variability selection method (hereforth, WSI) that analyzes how correlated n independent, quasi-simultaneous pairs of measurements are. For this method to work, it is required that a stellar source have measurements in two different filters, let us call them b and v. Following Sokolovsky et al. (2017), the WSI is given by:

$$I = \sqrt{\frac{1}{n(n-1)}} \sum_{i=1}^{n} \left(\frac{b_i - \bar{b}}{\sigma_{b_i}} \right) \left(\frac{v_i - \bar{v}}{\sigma_{v_i}} \right) \tag{5.8}$$

where, again, $\bar{v}$ and σ_v are the mean value of the set of measurements (see equation 5.2) in the v filter and its associated uncertainty, respectively; the same is analogously true for the b filter. The I index is sensitive to the detection of variability in time-scales much longer than the sampling rate of observations (i.e. time interval between two measurements). The WSI may take on negative values due to pairs of measurements appearing anti-correlated instead of uncorrelated. We find the sources with negative WSI values variable, so for this method we chose two *cut-off* values, a minimum and a maximum. This is our most robust and accurate index for variability.

- Strengths: Accurate and robust; takes into account the temporal sequence of the data
- Limitations: Longer computation times; some sources can show anti-correlation in the two bands and have negative WSI values.
- Requirements: Two data sets. Pairs of measurements must be quasi-simultaneous.

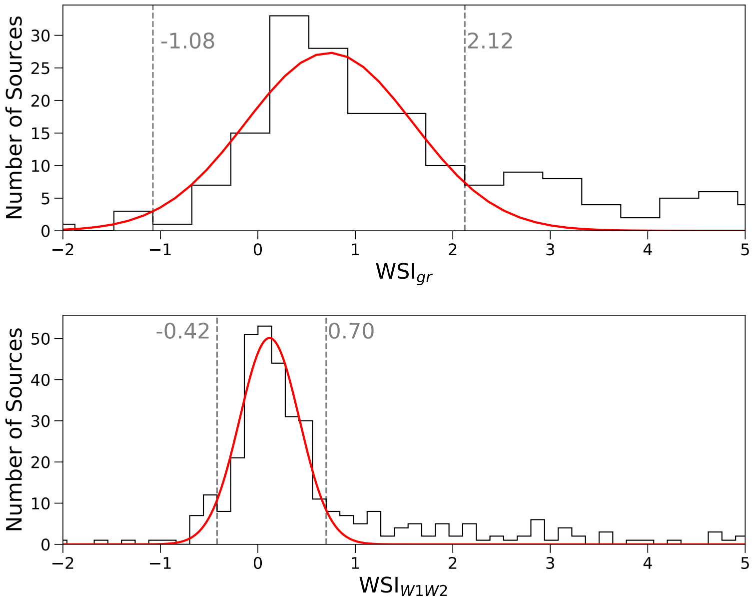

Figure 5.1: *WSI for ZTF and AllWISE light curves. The vertical dashed lines represent the chosen cut-off values and thus indicate the separation from variable to non-variable and the red curve is the fit Gaussian to the distribution.*

Stetson J

In addition to the WSI we also employ the J index proposed by Stetson in 1996 (Stetson, 1996) which only requires one band:

$$J = \frac{\sum_{k=1}^{n} w_k \operatorname{sgn}(P_k) \sqrt{|P_k|}}{\sum_{k=1}^{n} w_k} \tag{5.9}$$

where

$$P_k = \frac{n_v}{n_v - 1} \left(\frac{v_i - \bar{v}}{\sigma_{v_i}} \right)^2 - 1 \tag{5.10}$$

We employ this method because many of our optical light curves do not have quasi-simultaneous data in different bands and thus the Stetson J in conjunction with the aforementioned scatter-based indices will serve to classify variables with information in only one band, as well as for those sources which are excluded as variables in the WSI index.

- Strengths: most accurate index for only one data set.
- Requirements: one data set .
- Limitations: consecutive measurements must be as close in time as possible.

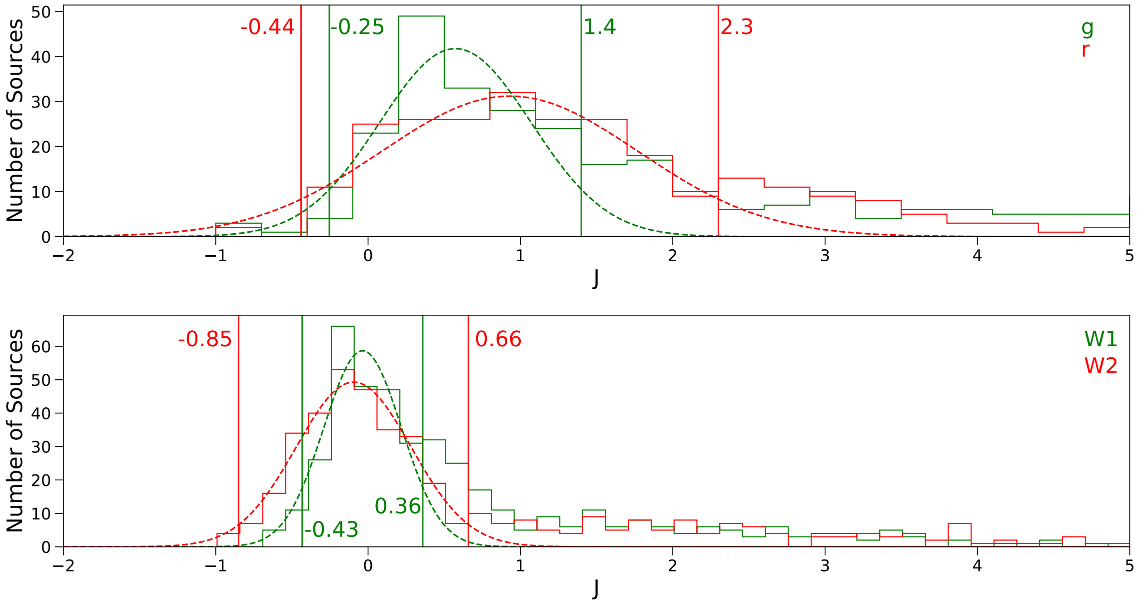

Figure 5.2: *Distribution of Stetson J for the ZTF (top) and AllWISE (bottom) data in their respective individual bands (g (green), r (red) and W1 (green), W2 (red)). Plotted in dashed lines is the Gaussian distribution which fits the center of the histogram bins and the vertical line refers to the chosen cut-off.*

5.2 Variability indices results

To create the set of variables we calculate the aforementioned variability indices for all sources in the ZTF and AllWISE data. From this table we aim to compute histograms of the variability indices, fit a Gaussian function (except for χ^2_{red} in which we should compare the distribution to the expected χ^2_{red} distribution) and determine from which bin on the distribution starts to present an excess of sources compared to the Gaussian. For the correlation-based indices (WSI and Stetson J), the non-variable sources should cluster near zero and form a Gaussian curve. Looking at Figures 5.1-5.2 we find that the distribution for both WSI and Stetson J form a nice curve from which we can fit a Gaussian function and make a good determination of the *cut-off* as stated above. For the other indices this is not as straightforward. Variables will have high values for every scatter-based index, be it χ^2, σ_w or A_{dip}/A_{burst}. The non-variables will group towards the lower values and we can see that in Figures 5.4-5.6. Because the variability in the Taurus YSOs is irregular in nature, we find that this should cause the scatter based indices to also form a Gaussian like peak near the small values, which we identify as being due to the non-variable population in our sample. In the following discussion we look at the histograms and Gaussian fit for each scatter-based index.

$\chi^2_{\mathbf{red}}$

χ^2_{red} is a specific case where we must compare the distribution with the expected χ^2_{red} function, however, because ZTF light curves have a quite variable number of epochs (see Figure 4.2) we must use an average number of observations to compute the expected χ^2_{red} distribution; in Figure 5.3 the solid black curve corresponds to this average in the g-band in the top plot and W1 in the bottom plot (the differences in the numbers of observations from one band to the other are negligible for the case of choosing a *cut-off* value from the distribution). Other distributions are plotted for different degrees of freedom which represent subsets of ZTF data. In Figure 5.3 we

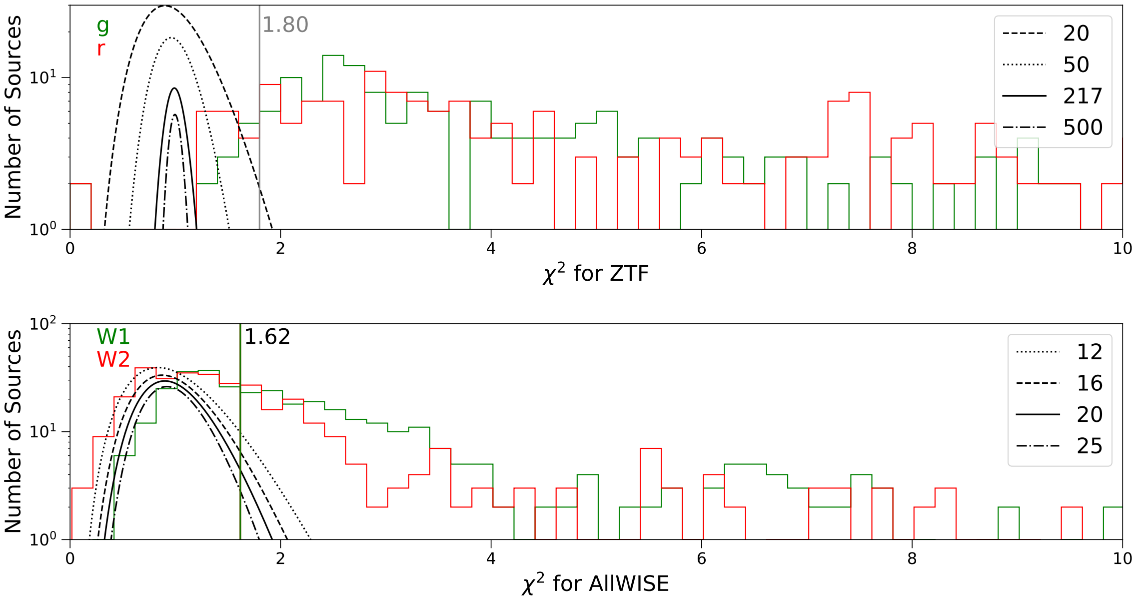

Figure 5.3: *Distribution of the* χ^2_{red} *values for the ZTF (top) and AllWISE (bottom) data in their respective individual bands (g (green), r (red) and W1 (green), W2 (red)). The function plotted in black is the expected distribution for different degrees of freedom k normalized to the total number of sources, which differs from band to band (i.e. g and r have different number of detected sources unlike W1/W2) and the vertical line refers to the chosen cut-off. For the ZTF data, which spans 3 years, it is found that the non-variable population seems low because there are few sources inside the area of the expected* χ^2_{red} *distribution. For the AllWISE data we find a peak near the smaller* χ^2_{red} *values which seems to follow the expected distribution.*

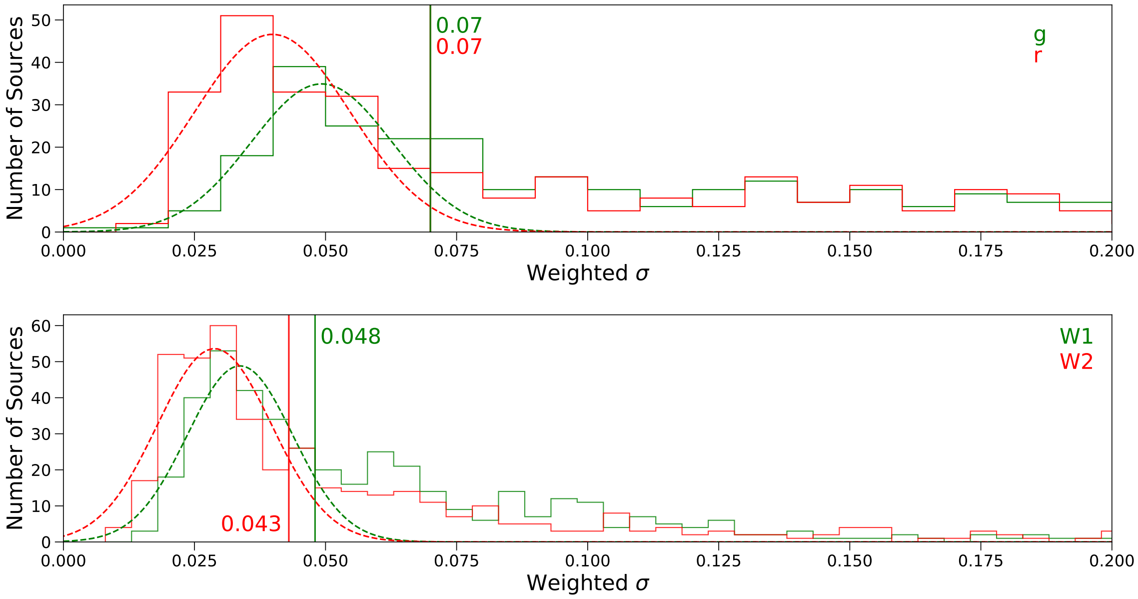

Figure 5.4: *Distribution of the* σ_w *values for the ZTF (top) and AllWISE (bottom) data in their respective individual bands (g (green), r (red) and W1 (green), W2 (red)). Plotted in dashed lines is the Gaussian distribution which fits the center of the histogram bins and the vertical line refers to the chosen cut-off. This index seems to work in the ZTF data as well as in the AllWISE data.*

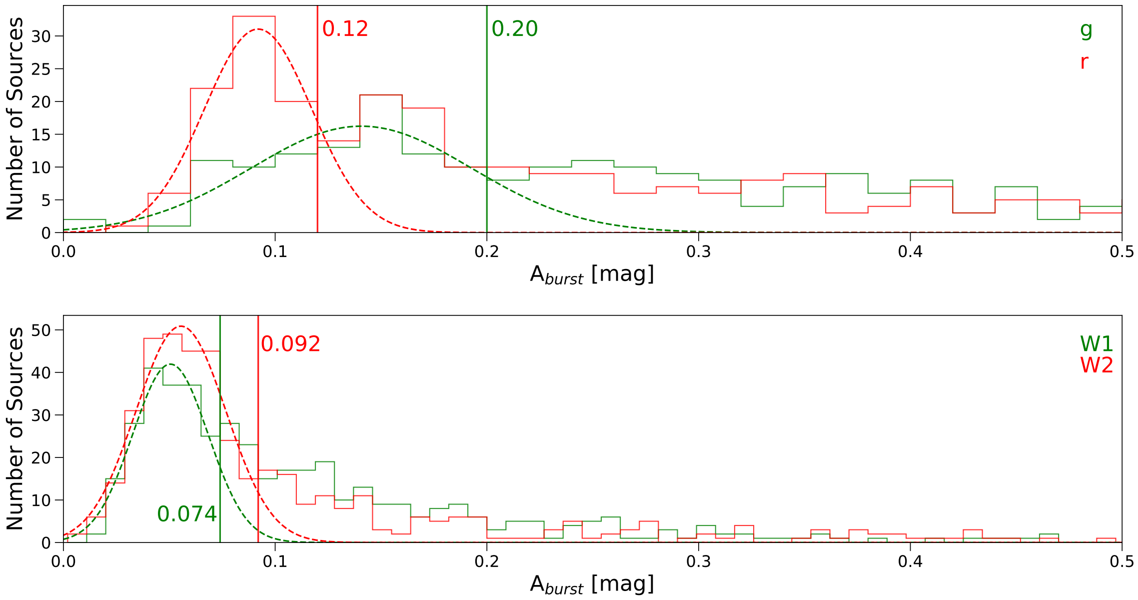

Figure 5.5: *Distribution of the A_{burst} for the ZTF (top) and AllWISE (bottom) data in their respective individual bands (g (green), r (red) and W1 (green), W2 (red)). Plotted in dashed lines is the Gaussian distribution which fits the center of the histogram bins and the vertical line refers to the chosen cut-off. It is clear that the ZTF data present more bursters than the AllWISE data. Additionally, for the ZTF data set, the r-band seems to have more low amplitude bursts when compared to the g-band, indicating that sources have larger bursts in the g band; this is seem in the WISE data with W2, but much less pronounced.*

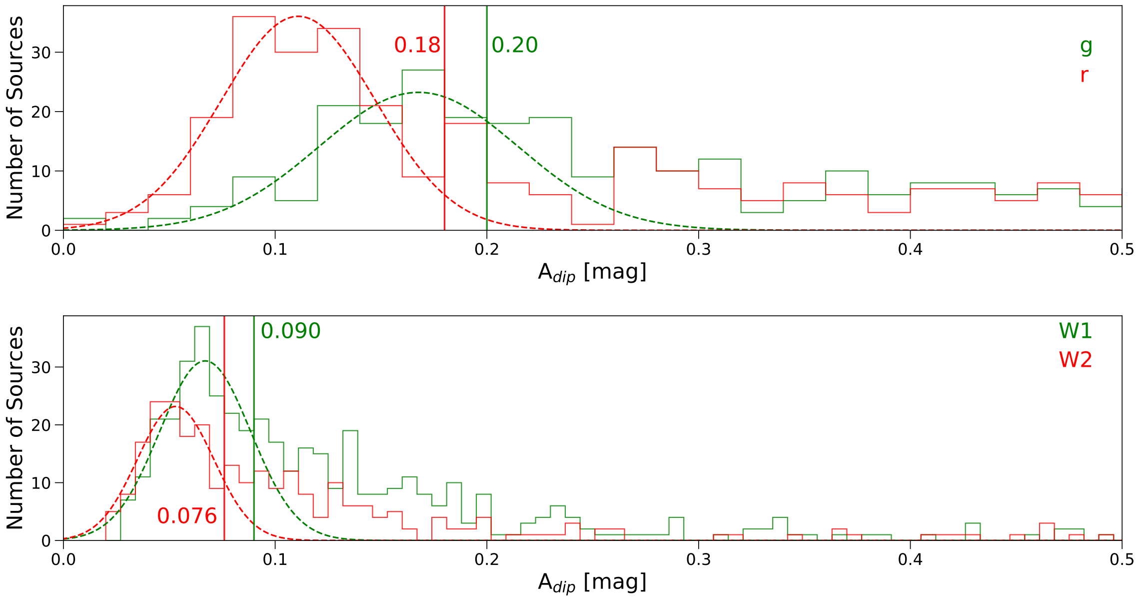

Figure 5.6: *Distribution of the A_{dip} for the ZTF (top) and AllWISE (bottom) data in their respective individual bands (g (green), r (red) and W1 (green), W2 (red)). Plotted in dashed lines is the Gaussian distribution which fits the center of the histogram bins and the vertical line refers to the chosen cut-off.*

can see that the ZTF data produces very few low χ^2_{red} values and that no clear peak is present at the expected location. In comparison, for the AllWISE data on the same plot the expected distribution fits quite well to the distribution. Because of this we chose the *cut-off* for χ^2_{red} for each survey with a different methodology than the rest of the indices. For the ZTF data we attributed the lack of a clear peak near the small values to the fact that due to the high cadence and time span of the data, most variable sources should be picked up by this index, along with a possible subset of non-variables which can have high χ^2_{red} values because of outliers. Because our catalog of sources is composed of confirmed YSOs, we expect a larger number of variables than non-variables (see Chapters 2-3) . Because χ^2_{red} is sensitive to outliers few sources have low ($<$5) values and the expected χ^2_{red} will not follow our χ^2_{red} distribution. Thus, because we expect the sources with low χ^2_{red} to be accurate non variables, we chose the *cut-off* where the expected χ^2_{red} distribution for a low number of measurements (20, dashed line in Figure) reaches zero. For the AllWISE data, the distribution in the bottom panel of Figure 5.3 fits the expected χ^2_{red} distribution much better and we do have a much larger number of possible non-variables. Because of this we visually chose the *cut-off* from the bin in which more than about half of its constituents should be due to the expected distribution. Because the AllWISE data has a lesser cadence and time span than the ZTF data, in addition to the MIR being less sensitive to a number of variability inducing phenomena (see previous Section 2.2 and Section 6.1 in the following chapter), we find that more sources will have low χ^2_{red} values and thus our χ^2_{red} distribution follows the expected one much better than for the ZTF data.

$\sigma_\mathbf{w}$

The σ_w measures the spread in the light curves so it is expected that the population of stars which have light curves with small amplitudes will cluster towards the smaller values whilst high amplitude variables will cluster towards the large values. Figure 5.4 shows that the non-variables do cluster in a Gaussian like curve towards the smaller values, being more pronounced in the AllWISE data in the bottom panel. Because of this we are able to fit a Gaussian and choose the *cut-off* value from the bin in which there starts to exist an excess of sources when compared to the Gaussian.

$\mathbf{A_{dip}/A_{burst}}$

Finally, the amplitude indices, A_{dip} and A_{burst}, measure the displacement in magnitude from the determined mean brightness. A_{burst} measures this maximum brightening displacement and the A_{dip} measures the maximum fading displacement. Figures 5.5-5.6 show that the distribution peaks towards smaller values in both cases. We find that in the ZTF data this peak is less clear, specially in the g band, but for both W1 and W2 the peak is very clear. In all cases, the Gaussian can be fit and thus we are able to choose the *cut-off* value from the bin in which there starts to exist an excess of sources when compared to the Gaussian.

Table 5.1: *Cut-off points and corresponding number of variables (and percentages in parenthesis) for each variability index employed in this study.*

	Survey	Band	χ^2_{red}	σ_w	A$_{dip}$	A$_{burst}$	J	WSI
cut-off	*ZTF*	g	1.80	0.070	0.20	0.20	-0.25; 1.4	-1.08; 2.12
		r	1.80	0.070	0.18	0.12	-0.44; 2.3	
	AllWISE	W1	1.62	0.048	0.090	0.074	-0.43; 0.36	-0.42; 0.70
		W2	1.62	0.043	0.076	0.092	-0.85; 0.66	
Variables	ZTF	g	327 (95%)	232 (68%)	236 (69%)	251 (73%)	178 (52%)	179 (58%)
		r	331 (94%)	186 (53%)	193 (55%)	270 (77%)	151 (43%)	
	AllWISE	W1	287 (64%)	223 (50%)	245 (55%)	254 (57%)	205 (46%)	190 (42%)
		W2	228 (51%)	201 (45%)	145 (32%)	160 (36%)	144 (32%)	

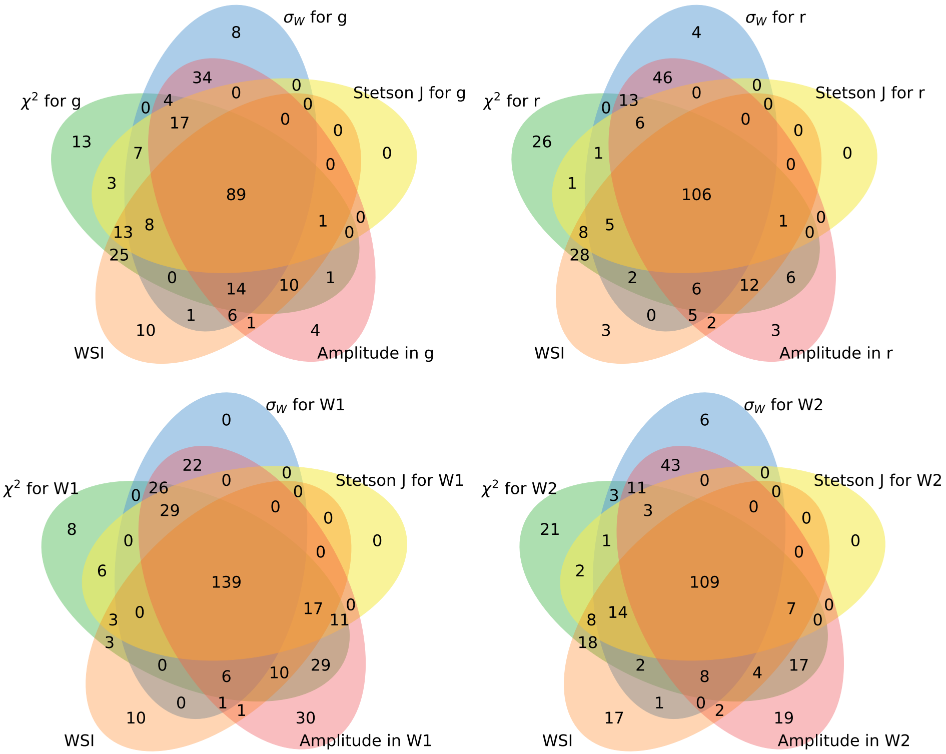

Figure 5.7: *Venn diagrams of the sources flagged as variable by the different variability indices in the ZTF data. Top left, g; top right, r; bottom left, W1; bottom right, W2. To be able to show all the indices in one Venn diagram with 5 associations we create a more simple amplitude index which is computed as follows: if a source is flagged as variable by either the A_{dip}* ***or*** *the A_{burst}. In all the Venn diagrams it is possible to see that most of the sources selected as variable in the WSI are also selected as variable in all other indices.*

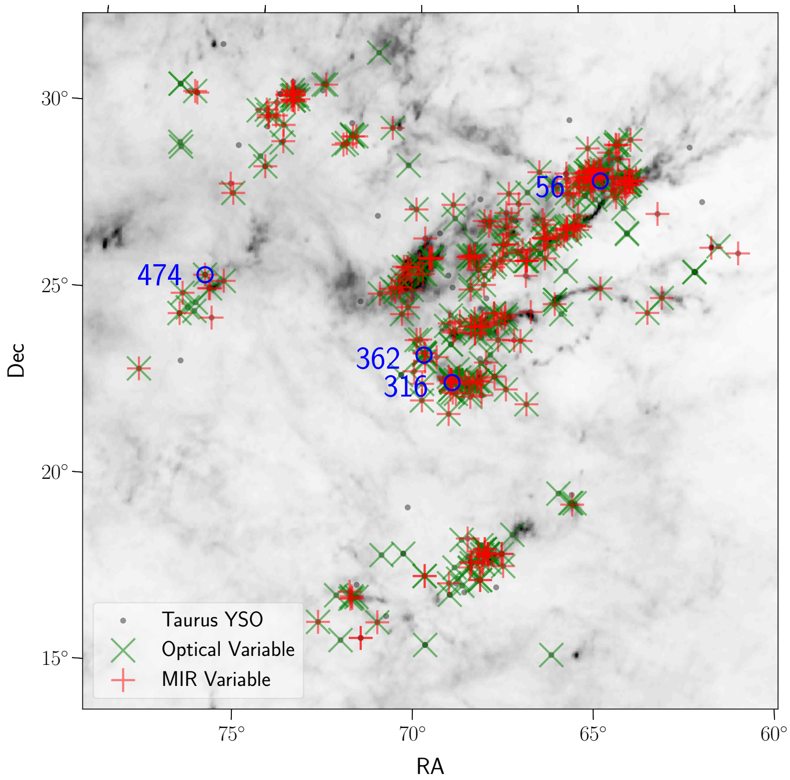

Figure 5.8: *Sky distribution of the MIR and optical variables on top of a Planck HFI 857GHz dust map with of the Taurus Molecular Clouds (Planck Collaboration, 2016). The sources presented in Figure 4.1.2 are marked in blue circles.*

5.3 Sets of Variable Stars

Figure 5.7 presents the associations between all the different indices for each available band. In each of the Venn diagrams presented we can see that most of the stars selected by the WSI are also selected by all other indices (Stetson J and the scatter indices), which confirms that this is the most robust and accurate of our employed variability indices. Table 5.1 shows the *cut-off* values for all employed variability indices and the number of selected variables from the cut for each of them. We see that all scatter indices select a larger fraction of sources in comparison with the correlation based indices. This is possibly due to all scatter indices being very sensitive to outliers, which are common in the light curves of the Taurus sources due to the irregular nature of their variations. Table 5.1 also shows that all indices selected a higher fraction of variables in the ZTF data than in the AllWISE data. Following the discussion of the performance of the χ^2_{red} index, this could be due to the same reasoning, which is that due to the optical being more sensitive for most origins of variability in YSOs and the fact that the cadence and time span of the ZTF data are much larger than in the AllWISE data, more variable sources will be selected in the optical.

Using ZTF DR6 and AllWISE data we determine two sets of stars: visible variables and infrared variables. To be selected as variable, YSOs must obey the following rules:

1. If the source has data in two available bands then it must be flagged as variable in the WSI. We choose this because the WSI is by far the best variability index that we have at our disposal and should have a high accuracy in separating variables from non-variables.

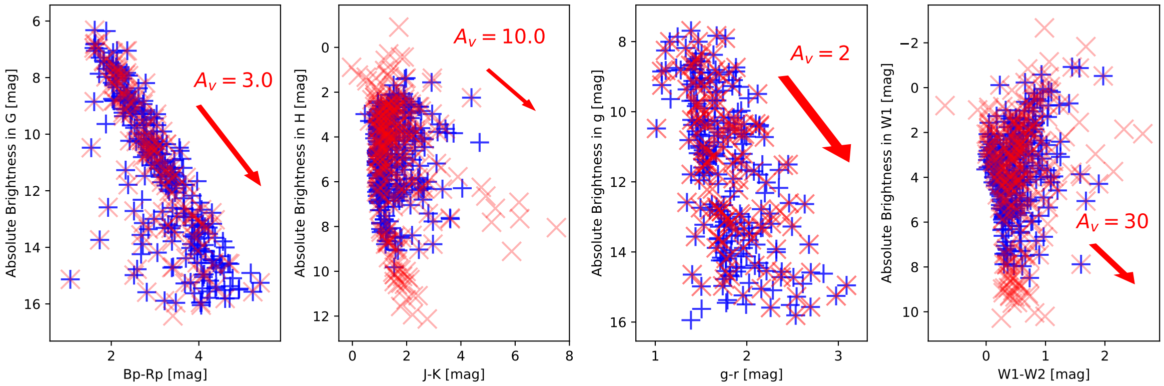

Figure 5.9: *CMD with the absolute mean brightness, computed from the Gaia eDR3 parallaxes, of the MIR (red plus sign) and optical (blue crosses) variables for the available photometry from Gaia eDR3, the NIR photometry from Esplin and Luhman (2019), the mean g/r photometry from ZTF and the mean W1/W2 photometry from AllWISE.*

2. If the star is flagged as non-variable in the WSI then it must be flagged as variable by at least 5 of the available 10 remaining indices (Stetson J, χ^2_{red}, σ_w, burst and dip, for each of the two band). We choose this cut because sources not selected as variable in the WSI have a flat distribution of the number of indices which flag them as variable, so we choose the mean value.

3. If the star does not have data in both bands, then it must be flagged by at least 3 indices in that band. This cut was chosen because, for the sources with data in only one band, the distribution of the number of indices which flag them as variable shows a clear drop in the number of sources from 2 indices to 3.

Figure 5.8 shows the sky distribution of the selected optical (green crosses) and MIR variables (red plus signs) on top of a Planck HFI 857GHz dust map with of the Taurus Molecular Clouds. We see that this distribution does not change much from the full distribution of the Taurus YSOs in our catalog (see Figure 3.1), with most of the clouds having either optical or MIR variables in them. Figure 5.9 shows the CMD for the available photometry from Gaia eDR3, the NIR catalog from Esplin and Luhman (2019), the ZTF mean g/r and the AllWISE mean W1/W2. In all of these CMDs we do not find either the MIR or optical variables to be located in specific regions of the CMD. In the following discussion we present a brief analysis of each set of variables.

5.3.1 Optical Variables

Using the methodology described above we find that 79% (304/386) of the sources are variable in the ZTF DR6 data. Of these 304, 115 have spectral type later or equal to M6, which means that they are candidate brown dwarfs (see Chapter 3). Figure 5.10 shows how the A_{dip} and A_{burst} values change with the mean absolute brightness of the source in that respective band, computed from the Gaia eDR3 parallaxes. From these plots we find that, in the g band, 10 sources - [#22, #316, #465, #335, #197, #188, #465, #415, #272, #252], sorted by decreasing A_{dip} - have A_{dip} larger than 2 and 7 sources - [#235, #128, #405, #250, #186, #340, #126] - have A_{burst} larger than 2. Of these objects, source #235 presents the A_{burst} with an amplitude of 3 g magnitudes and is the only source with a A_{burst} larger than 2 magnitudes in the r-band. This source, 2MASS J04322329+2403013, is of spectral type M7.75 and is not classified in GCSV

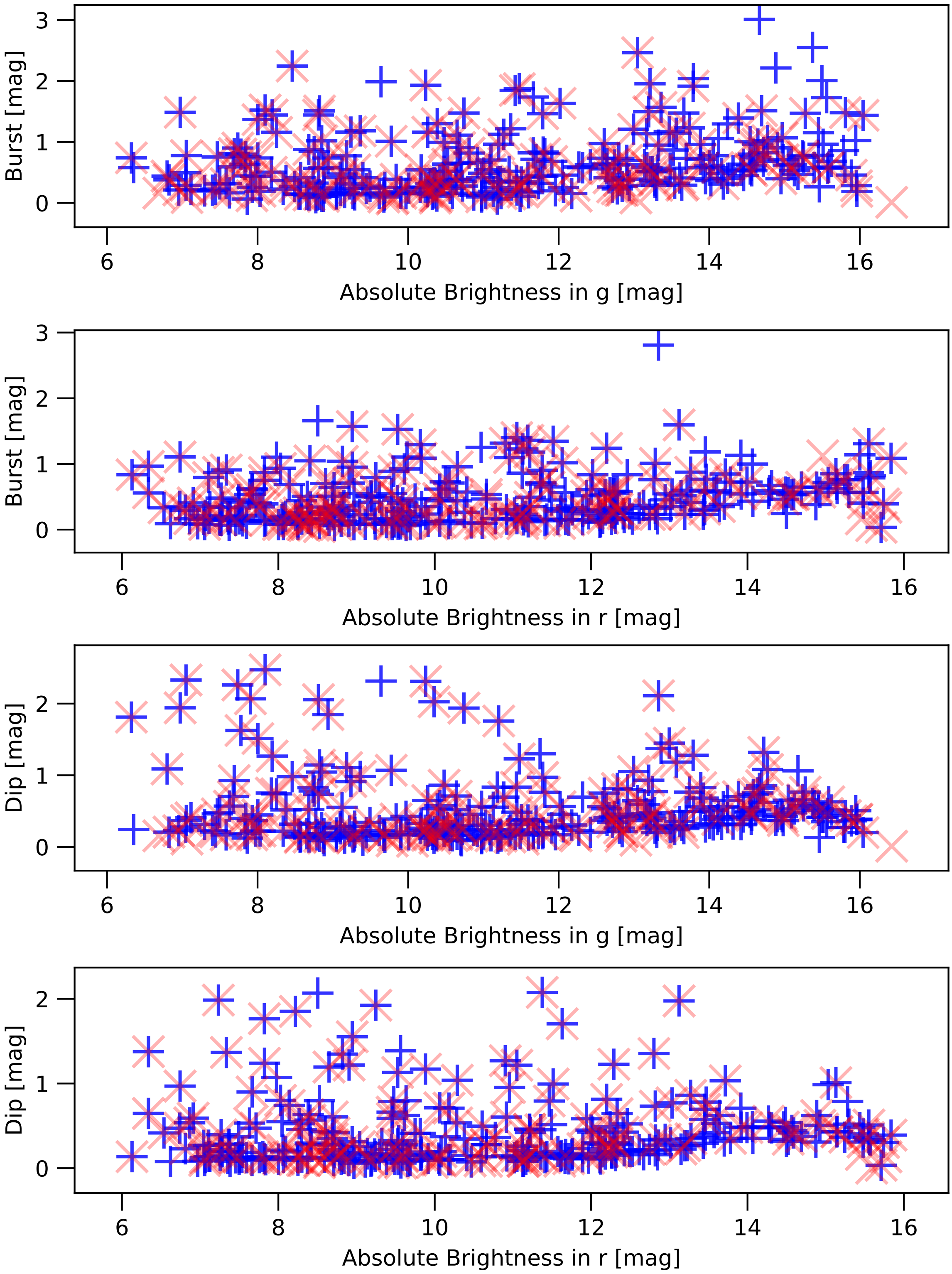

Figure 5.10: *A_{burst}/A_{dip} as a function of the mean absolute magnitude computed from the Gaia eDR3 parallaxes in ZTF g/r. MIR variables are red crosses and optical variables are blue plus signs.*

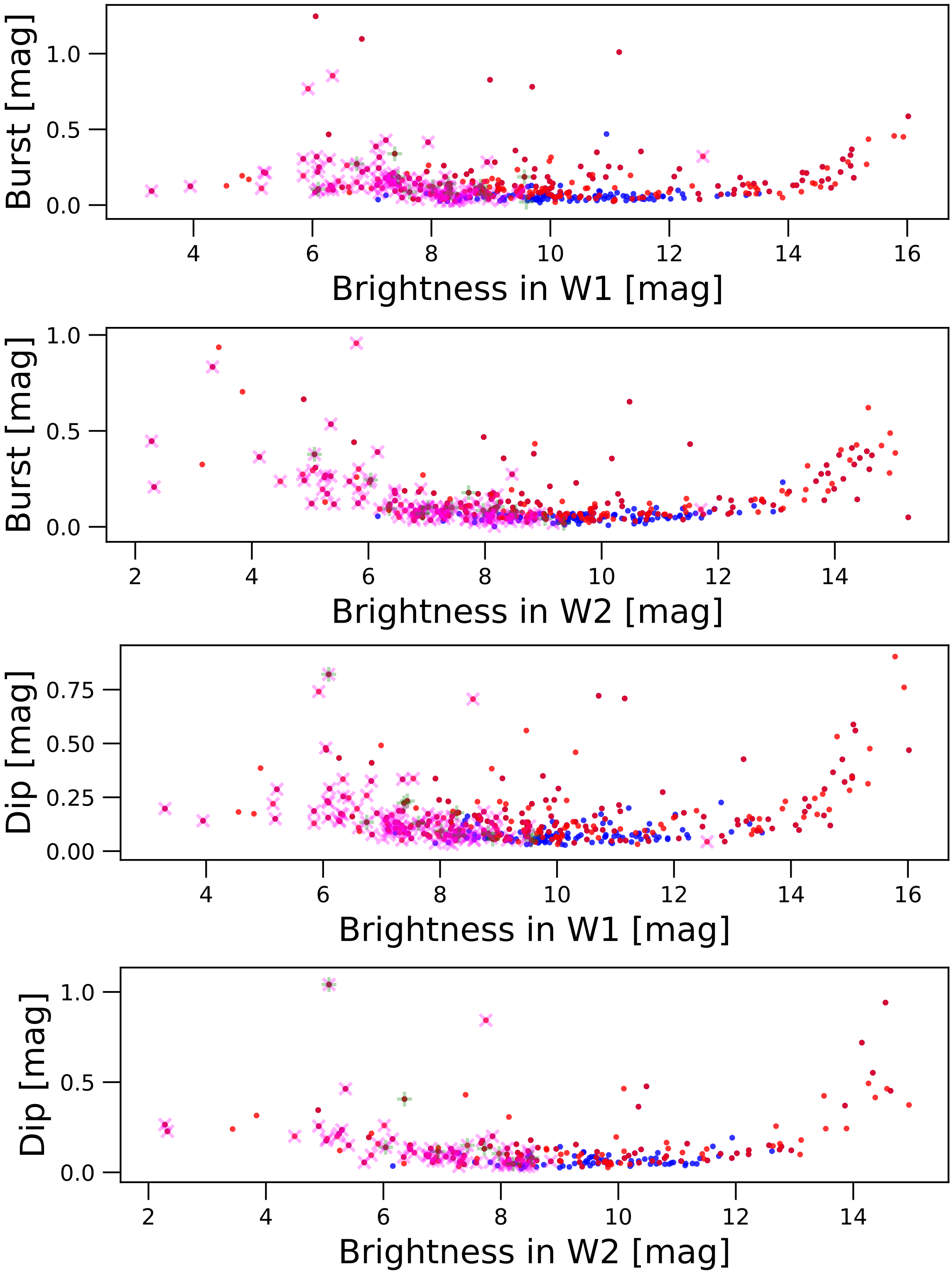

Figure 5.11: *A_{burst}/A_{dip} as a function of the mean absolute magnitude computed from the Gaia eDR3 parallaxes in AllWISE W1/W2. MIR variables are red crosses and optical variables are blue plus signs.*

while clearly showing high amplitude, fast and irregular increases in brightness. On the other hand, the largest A_{dip} value in the ZTF data belongs to source #22, CW Tau, which is a K3 stochastic variable not presenting any clear features in its light curve. The second largest A_{dip} value in the ZTF data belongs to source #316, also known as HQ Tau, a K2 star whose light curve is shown in Figure 4.7. This source is classified in GCVS as INS, which can explain the fast lower amplitude VDs that it presents along the time span of the ZTF light curve, however not the large VD that was picked up by the A_{dip}.

5.3.2 MIR Variables

Using the methodology described above we find that 62% (279/448) of the sources are variable in the AllWISE data. 5.11 shows how the A_{dip} and A_{burst} values change with the mean absolute brightness in W1 and W2. In comparison with the ZTF data, the values of A_{burst} and A_{dip} are much smaller, as is expected from the fact that the AllWISE survey covers a relatively small timescale and that many of the origins for variability are less sensitive in the MIR (see the previous Section 2.2 and Section 6.1 in the following Chapter). Regardless, we still find some high amplitudes sources. Source #321, HP Tau, is a K4 source which has the largest burst dip amplitude in W1 of this data set. It is a T Tauri star (R. Koehler, priv communication) and is classified as INB in the GCVS. Source #316, HQ Tau is the source with the largest A_{dip} value for AllWISE, indicating that this source might have a tendency towards presenting VDs. The second largest VD belongs to source #325 which is known as UGCS J043555.45+225313.5 and does not appear in any of the variability catalogs nor Gaia DR2. This source was found from the works of Esplin and Luhman (2019) and Luhman (2018) and is a L0.5 type brown dwarf. The largest VD in the W1 band is also attributed to another brown dwarf, source #249 or UGCS J043242.95+181742.3, which is of L2 type.

Chapter 6

Variable Set Analysis

Now that we have determined our sets of both optical and mid-infrared variables we want to study their properties. To start the chapter we study the expected amplitudes in brightness and color due to the different physical mechanisms presented in Section 2.2 and explain how these can create unique properties in the data that point to the origin of variability. Then we present the general properties of our sets of variables, the color and color-magnitude changes and finally the changes in the determination of the YSO class (see Section 2.1.2).

6.1 Toy models for the possible origins of variability

We know from Chapters 2-3 (specially Section 2.2) that the variability in our sample of YSOs is expected to be caused not by one single physical mechanism, but by a range of possible phenomena. Our goal is to study the data of the sources that are determined to be either mid-infrared or optical variables and investigate the properties of each set in order to try and infer the origins of the observed variability. In this section we perform several calculations to obtain the brightness and color amplitudes expected from specific origins of variability. We do this in order to find possible unique properties of each physical phenomenon that can be identified in our optical and/or MIR data. We go over the 3 main causes for YSO variability: spots, variable extinction and variable disk properties or accretion. Table 6.1 shows the expected brightness and color amplitudes for the g/r and W1/W2 for the different chosen parameters which are presented in the discussion below.

Spots

Following Carpenter et al. (2001); Vrba et al. (1986) we determine the changes in a specific band due to changes in photospheric temperature across the stellar surface from the following expression:

$$\Delta m(\lambda)=-2.5 \log_{10}\left\{1-f\left[1.0-B_\lambda\left(T_{\text{spot }}\right) / B_\lambda\left(T_*\right)\right]\right\}, \tag{6.1}$$

where f is the fraction of the surface area covered by the spots, $B_\lambda(T)$ is the Planck function and T_{spot}, T_* refer to the temperature of the spot and the star, respectively. This expression can be used to calculate the expected amplitudes for both hot and cold spots, because they only vary in temperature and fraction of surface area.

Spots are one of the most well studied origin for variability, specially cool spots (Vrba et al.,

Table 6.1: *Expected brightness and color amplitudes for the g/r bands and W1/W2 for the different toy models for different origins of variability, using different parameter values of R_V and f*

Origin of Variability		Δg	Δr	ΔW1	ΔW2	Δ(g-r)	Δ(W1-W2)
Hot Spot	$f = 1\%$	0.40	0.17	0.018	0.016	0.23	<0.010
	$f = 5\%$	1.20	0.67	0.089	0.077	0.53	0.012
Cold Spot	$f = 10\%$	0.11	0.11	0.084	0.077	<0.010	<0.010
	$f = 30\%$	0.39	0.39	0.27	0.25	<0.010	0.020
Extinction ($A_V = 1$ mag)	$R_V = 3.1$	1.21	0.85	0.058	0.035	0.36	0.023
	$R_V = 5.0$	1.13	0.88	0.066	0.040	0.25	0.026

1989; Bertout and Bouvier, 1989; Herbst et al., 1994; Carpenter et al., 2001; Scholz et al., 2009). The parameters of the coverages and temperatures are well constrained through observations with cool spots rarely presenting differences in temperature larger than 1500K-2000K (Carpenter et al., 2001) and coverages larger than 30%. Cool spots are also stable and periodic (Carpenter et al., 2001).

Hot spots, on the other hand, are not stable and only for some cases have periods been determined (Carpenter et al., 2001; Vrba et al., 1993). The parameter values for these spots are less constrained, with some authors using coverages similar to cool spots (Wolk et al., 2013) whilst others claim they should be much smaller (1%-10%) (Carpenter et al., 2001). Bouvier et al. (1993) studied spots in the Taurus YSO population and found coverages for cold spots up to 25% and for hot spots up to 30%[1], however this latter value is an outlier being that all other coverage determinations for hot spots are not larger than 15% and most are lower than 5%; additionally the hotter the hot spot, the lower the coverage determination. The temperature of hot spots inferred from optical observations is usually lower than 8000K (Carpenter et al., 2001) but can plausibly be higher (>10 000K).

For our toy model we take the temperature of our star to be 4000K, which is the temperature for a $0.5M_\odot$ star at 1Myrs of age according to the model from D'Antona and Mazzitelli (1997). We find this value to represent our stellar population well from the analysis of the properties of Taurus SFR 3. Taking the hot spot temperature to be $T_{spot} \sim 8000K$ and varying the fraction f from 1% to 5% we find that g should be the most sensitive of our bands for this type of phenomenon with amplitudes from $\Delta g = 0.40$ mag to $\Delta g = 1.2$ mag (from $f = 1\%$ and $f = 5\%$, respectively), followed by r with amplitudes up to $\Delta r = 0.67$ mag for $f = 5\%$. W1/W2 have very low amplitudes even for larger coverages and thus hot spots are not expected to be the primary origins for MIR variability. Assuming a cold spot temperature of 2000K and $f = 30\%$ both the g and r bands have the same maximum amplitude of $\sim \Delta 0.39 mag$. W1 and W2, on the other hand, have maximum amplitudes of $\Delta W1 \sim 0.27$ mag and $\Delta W2 \sim 0.25$. Variations due to cold spots are colorless in both optical and MIR while hot spots induce significant color changes even for $f = 1\%$, but only in the optical.

Variable Extinction

When the starlight we observe travels through some ISM or circumstellar material it will be reddened due to shorter wavelength light being more scattered (than the longer wavelengths)

---

[1] This source is GK Tau which is source #273 in this work.

and because the dust absorbs and re-emits at longer wavelengths. Equation 1.2 can be modified to incorporate the extinction A_λ as follows:

$$M_\lambda = m_\lambda - 5\log\left(d_{pc}\right) + 5 - A_\lambda. \tag{6.2}$$

The properties of the clouds in which YSOs form, in addition to the possible presence of an envelope and/or disk components, may suggest variable extinction be one of the primary sources of brightness variability, at least in the optical. This is because in the MIR, scattering is much less common and the effects of interstellar reddening are much lesser. To investigate this, we employ the extinction law from Cardelli et al. (1989) and determine the expected magnitude changes for the ZTF and AllWISE bands assuming $R_V = 3.1$ and $R_V = 5.0$. These values represent typical properties of the ISM in the Milky Way and abnormal properties such as higher density or/and grain growth in circumstellar environments, respectively (Froebrich et al., 2018; Mathis, 1990; van den Ancker et al., 1997).

We find that extinction causes much larger brightness and color changes than any spot activity. By changing the A_V from 0 to 1 we find very significant and similar changes in g and r for either value of R_V. The MIR bands however show a detectable but low amplitude value which is larger for $R_V = 5.0$. This increase in R_V causes the extinction vector to become steeper in a CMD, thus making the slope of the vector a probe of obscuration due to larger sized particles than the ISM average. Finally we find that variable extinction can create lower color change for the MIR variables than in the optical. The values in Table 6.1, the values for the extinction amplitudes (and thus colors) are presented for changes of $\Delta A_V = 1$, however this change can be much higher and cause larger variations.

Variable Accretion and other disk related phenomena

Due to the complexity of accretion processes, creating even a simple toy model requires detailed knowledge and analysis of stellar-disk interaction models. Such an amount of work is beyond the scope of this thesis and could not be performed within the project's timeframe. Nevertheless, we are aware of the importance of accretion as a dominant source of variability for some objects. We expect the effect of accretion to be more prominent in our optical data, primarily due to the expected increase in the intensity of Balmer emission lines. One would expect the r band observation to be more sensitive to changes in accretion rate due to the presence of H_α in this band. Carpenter et al. (2001) and Wolk et al. (2013) used the models created by Meyer et al. (1997) to show that many of the features in the 2MASS light curves can be explained by changes in the accretion rate with a factor of 30. Change in accretion rate causes the source to become bluer when fainter. Hillenbrand et al. (2019) also found a YSO whose W1, (W1-W2) CMD variability slope was shallower than the determined W1, (W1-W2) slope for the extinction vector and attributed this, in part, to accretion episodes; thus we find that the MIR can also be sensitive to variability induced by accretion processes but in this work we focus on their effects in the optical (see Section 6.5).

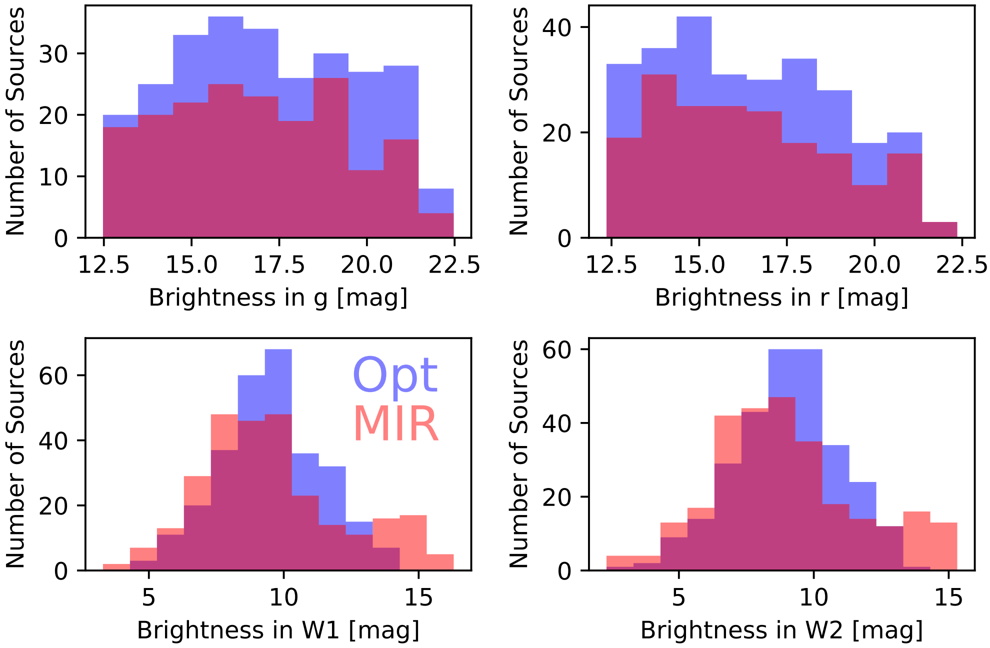

Figure 6.1: *Mean brightness for the set of optical (blue) and mid-infrared (red) variables.*

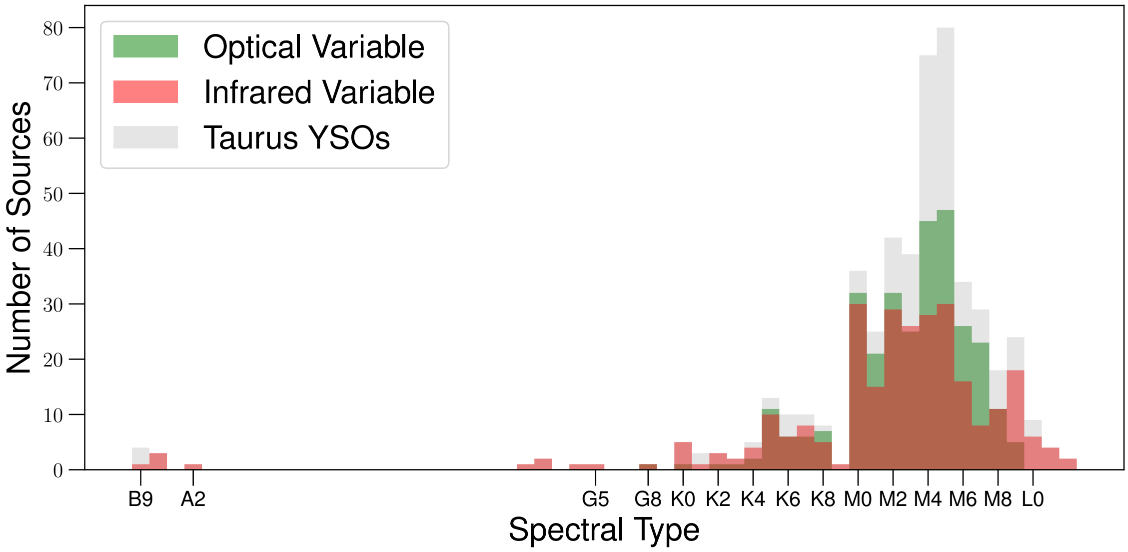

Figure 6.2: *Spectral type distribution for all the Taurus YSOs in Esplin and Luhman (2019), our sample of optical variables (green) and our set of mid-infrared variables (red).*

6.2 General Properties of Variable YSOs in Taurus

First, we look into the distribution of brightness and spectral type; see Figures 6.1-6.2. In Fig 6.1 we can see the brightness distribution of both sets of variables and it is possible to conclude that, at least for the ZTF bands (g and r) there is no single clear peak, unlike in the AllWISE bands (W1 and W2). Upon comparing with the same plot but for the whole sample distribution, Figure 4.5, we find that the flat peak in the g band plot from $g = 16$ to $g = 19$ has turned into two separate peaks at those same magnitudes; this is the same for both sets of variables. In the r plot we find peaks in the distribution at $r = 15$, $r = 18$ and $r = 21$, the latter not being present in the full sample distribution. We find that the distribution, although slightly changed, does not seem to present a preference towards brighter or fainter stars. In the AllWISE case, the distribution for both sets of variables closely resembles the full distribution. In Figure 6.2 we see the distribution of the spectral type for all YSOs, MIR variables and optical variables. We find that the shape of the distribution of the optical variables is very similar to the full distribution, with the peak being in the same bin (M5). In the case of the MIR variables, the distribution is somewhat flat in the M dwarf range. The bin with most amount of sources is M0, which is 5 subtypes away from the peak of the full distribution. Our final set of variables, either optical or MIR, covers all existing spectral types in the Taurus Clouds and ranges from B9 type to L2 type, showing that variability is not restricted to only some spectral types.

6.3 Color Variations

Because both ZTF and AllWISE provide data in at least 2 different bands, we calculate the color over the time span of the photometric data and then determine color statistics: the mean color, maximum color, the minimum color and from the last two the amplitude in color (MAX(color)-MIN(color)). Color variability can directly point to some origins of YSO variability. From the calculations in Section 6.1 we know that cold spot variability is mostly colorless in both the optical and MIR while still presenting significant brightness changes in all of our bands. Hot spots also cause colorless variability in the MIR but due to the changes in brightness being quite undetectable. High color amplitudes can then be related to hot spots in the optical and also related to extinction and disk related phenomena such as a variable accretion rate and variable inner disk radii in both the optical and MIR.

In Figure 6.3 we can observe how the brightness amplitudes (MAX(brightness)-MIN(brightness)) change in respect to the mean color (first and second panel from the top) and the color amplitude (third and fourth panel from the top) for our optical and MIR bands. In the top panel we see that both sources with the largest amplitudes in g, #335 and #465, have g-r colors lower than 2.0, similar to most high-amplitude variables in g. There are, however, some sources with high amplitudes and colors greater than 2.0, although clearly less than for the bluer sources. The source with the highest amplitude in g with g-r color greater than 2.5 is #265, which presents clear VBs. These high amplitude sources are usually associated with fast high amplitude variability which causes very irregular light curves with almost no discernible features. Source #465 (M1.5) is an exception, being

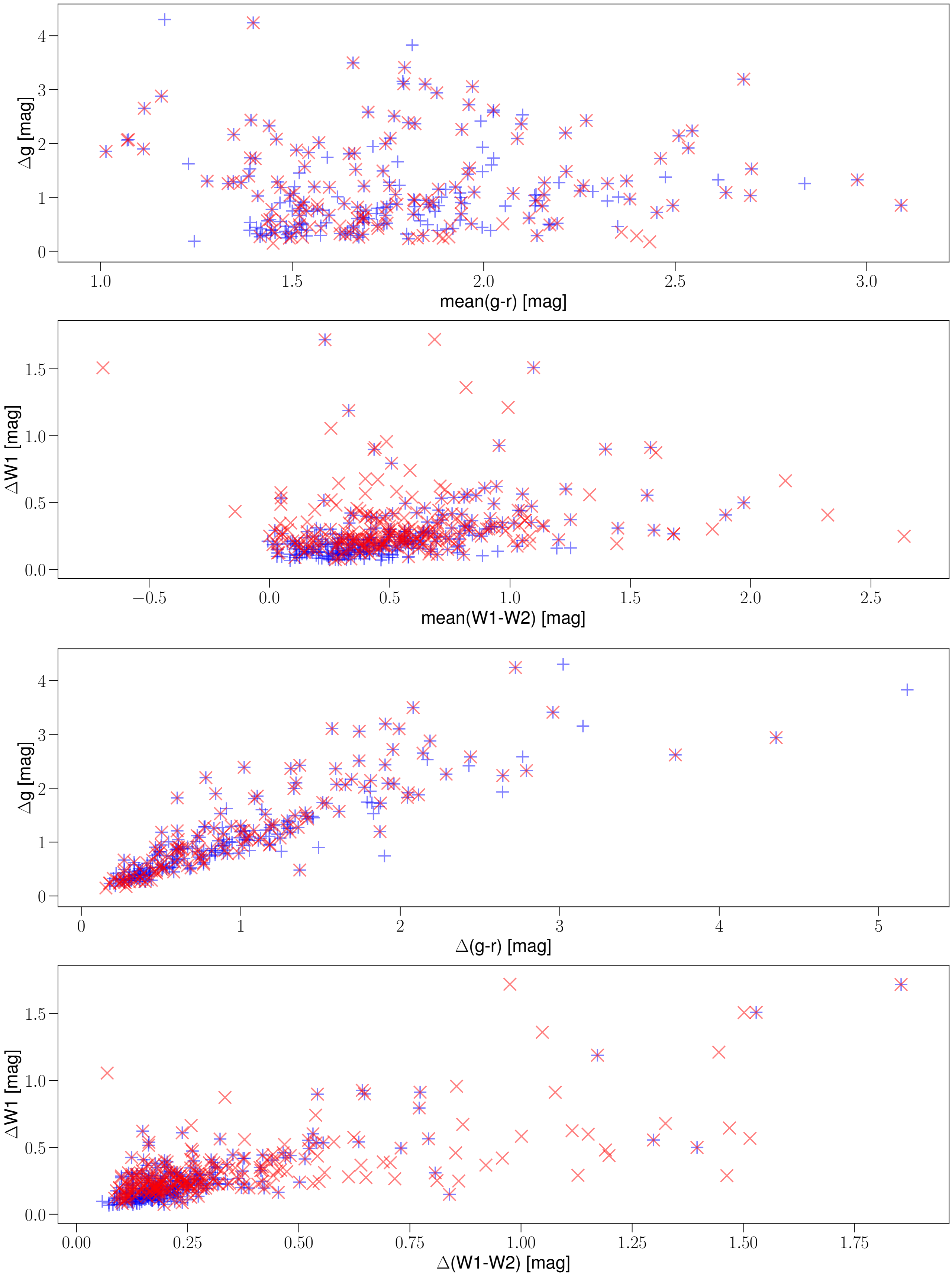

Figure 6.3: *Amplitudes in g and W1 as a function of mean color (top two plots) and the amplitude in color over the light curves (bottom two plots). MIR variables are red crosses and optical variables are blue plus signs.*

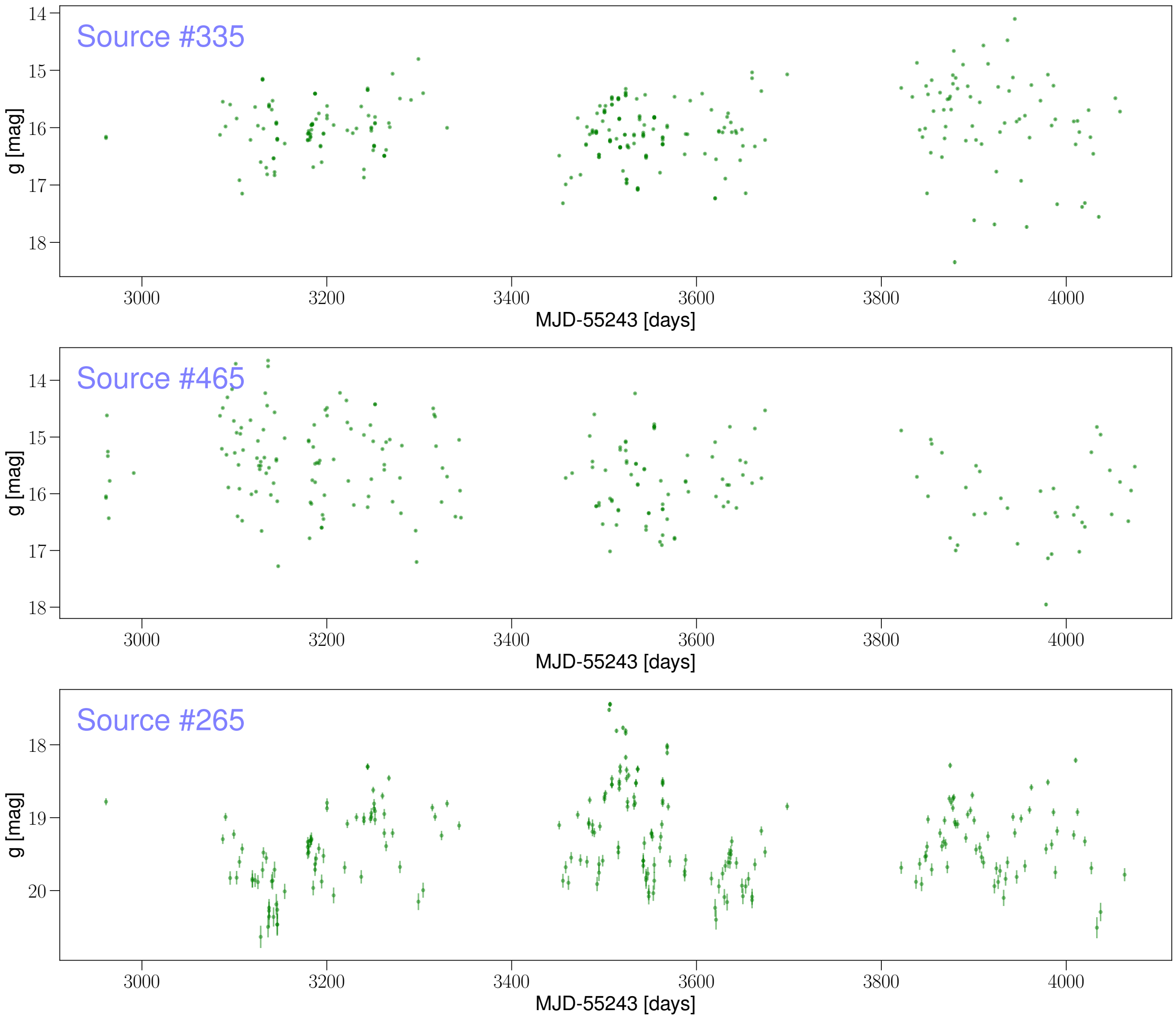

Figure 6.4: *g light curves for the two sources -#335 (top panel) #465 (middle panel)- with the highest amplitude in g and the reddest source with an amplitude in g larger than 3 magnitudes -#265 - (bottom panel).*

that it which shows a decrease in brightness over the 3 years of ZTF data (long timescale phenomenon). Figure 6.4 shows the ZTF light curves for sources #465, #335 and #265.

In the second panel from the top in Figure 6.3, the brightness amplitude for W1 is shown as a function of the mean W1-W2 color. In the redder part of the plot (W1-W2$\gtrsim$ 1 mag) we see some medium amplitude variables but only one very low amplitude ($W1$ $\lesssim$0.2 mag) variable - #89. Most of the lower amplitude variables are found with colors $\lesssim$1.0 mag The three reddest sources are K type stars which have no ZTF data and are undetected in Gaia eDR3: #3, #16 and #210. These are most probably very young embedded sources that have not yet become optically detectable given that sources #3, #16 are classified as flat spectrum sources and #210 as class I (see Section 6.4 in this Chapter).
The bottom two panels in Figure 6.3 show how the amplitude in brightness changes with the amplitude in color. We see a correlation which is clearer in the ZTF plot and seems to imply that the sources with a larger amplitude in color are also the sources with the largest amplitude in the g-band. The three sources with amplitudes in color larger than 3.5 mag in the ZTF

plot are #223, #235 and #347. Sources #223 (M2.5) and #347 (M5) have fast variability high amplitude light curves which show no feature and the latter is classified in GCVS as INS (presents fast variability). Source #235 is a source presenting very fast VBs that are not well sampled in the light curves (see Figure 6.5). For the AllWISE plot we see the same behaviour but for smaller amplitudes, be it in brightness or color. The source with the highest color amplitude in this plot is #321, also known as HP Tau. It is a known T Tauri in GCVS of type K4 that shows dips of different magnitudes over the time span of the ZTF light curve. ZTF Light curves for the four aforementioned sources are shown in Figure 6.5.

Regarding colorless variations, which compose most of the set of NIR variables presented in Carpenter et al. (2001), in Figure 6.3 we see that there are very few such sources in either set of variables. In ZTF there is no source with an amplitude in color smaller than 0.1 mag while in AllWISE there are 22. Colorless variations are expected for cold spots (Carpenter et al., 2001) but in ZTF variable extinction and hot spots may dominate the light curves according to the calculations in Section 6.1 and only sources with no disk might be candidates for observing variability because of hot spots. Using the expected color amplitudes for a cold spot coverage of 30% (Table 6.1) we find that none of the sources in ZTF or AllWISE should be variable **only** because of cold spots. This will be further discussed in Section 6.5.

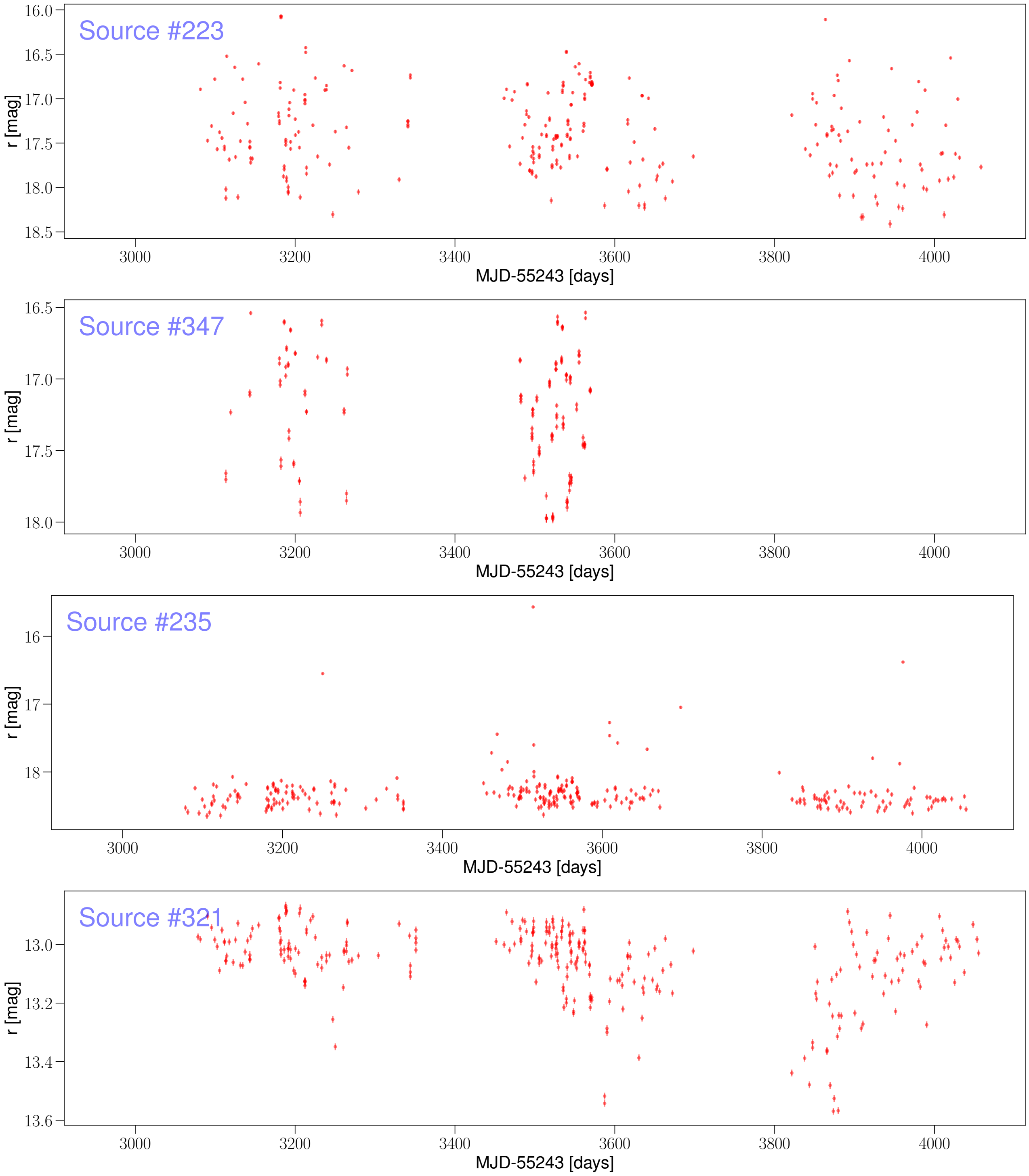

Figure 6.5: *ZTF g light curves for the sources with highest color amplitude in ZTF and AllWISE data. Top to bottom, #223, #347, #235 and #321.*

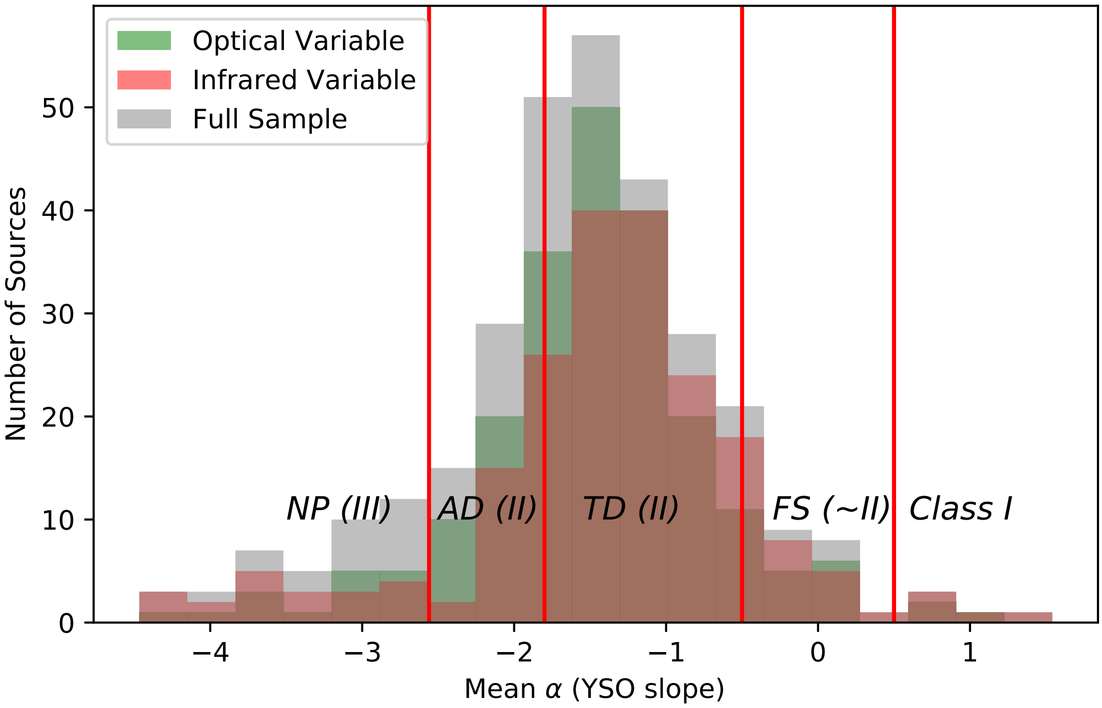

Figure 6.6: *Distribution of the YSO Teixeira et al. (2012) classes for all sources with available measurements (grey), MIR variables (red) and optical variables (green). The vertical red lines represent the limits for the different classes from Teixeira et al. (2012) which were introduced to the reader in Section 2.1.2 and the black text identifies them (from left to right: Naked Photosphere, Anaemic Disk, Thick Disk, Flat Spectrum and Class I).*

6.4 Protostellar Class variations

Using the four WISE bands, it is possible to determine the slope α (see Section 2.1.2; hereafter, YSO classification slope) to classify YSOs. Teixeira et al. (2012) use the 4 IRAC bands from the Spitzer Space Telescope (Werner et al., 2004) to get a determination of the YSO classification slope. We employ the 4 WISE bands due to the similarity between the instruments and their photometric properties [2] Authors find that NIR and MIR surveys such as 2MASS and Spitzer are powerful tools to detect YSOs in most star forming regions, including Taurus (Teixeira et al., 2012; Rebull et al., 2010; Luhman et al., 2010; Robitaille et al., 2006). AllWISE should thus be able to correctly measure the YSO classification slope and some authors have already used the W1-W4 bands to classify YSOs (Luhman et al., 2017; Esplin and Luhman, 2019; Koenig et al., 2012; Wolk et al., 2013). The classifications we employ are those defined by Teixeira et al. (2012), which have been introduced and explained in Section 2.1.2.

In this section we present the results of how the YSO classification slope determination changes over the few epochs we do have in all four AllWISE bands. We first find, for each source, all available epochs with measurements in all four WISE bands and for each set of measurements we perform Monte Carlo simulation, in which we generate random values from the Gaussian distribution defined by the brightness measurement (μ) and its error (σ). We generate 100 random values for each WISE band and then determine slopes for each realization

---

[2] On axis filter transmission plots for Spitzer can be found in the VSO website through: `http://svo2.cab.inta-csic.es/theory/fps/index.php?mode=browse&gname=Spitzer&asttype=`. The plot for the WISE bands is in Figure 4.11.

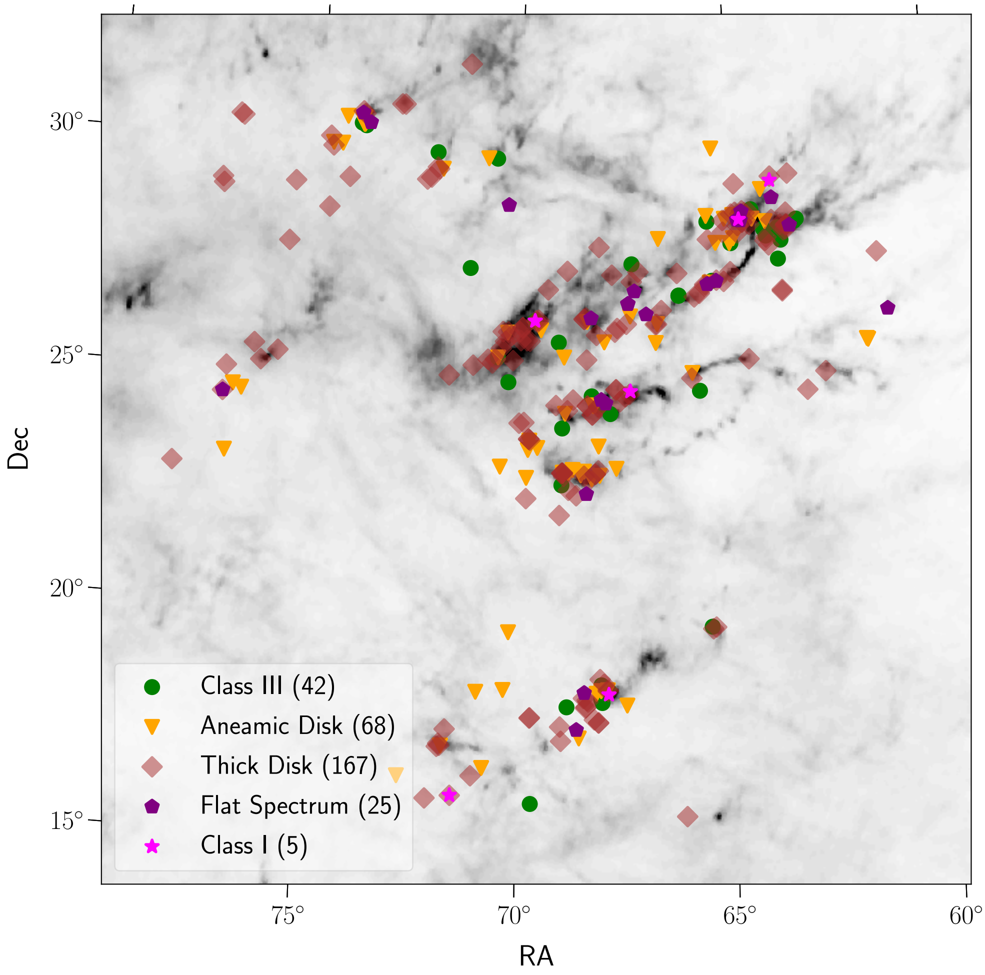

Figure 6.7: *Planck HFI 857GHz dust map with the distribution of the YSO classes as defined in Teixeira et al. (2012) (see Section 2.1.2) determined from the mean YSO classification slope. The symbols related to the different classifications (with the number of sources within that specific class in parentheses)*

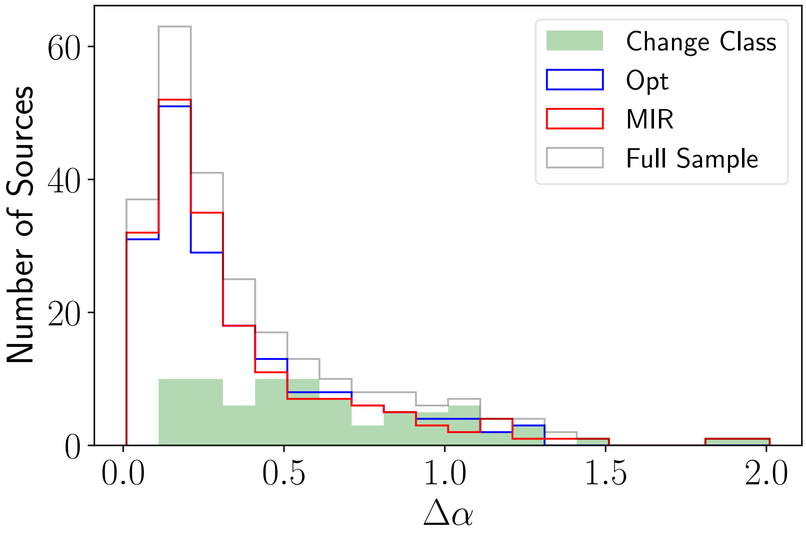

Figure 6.8: *Histogram of the amplitudes (MAX-MIN) of the YSO classification slope determinations over the available epochs for all sources with data on the 4 WISE bands in more than 1 epoch.*

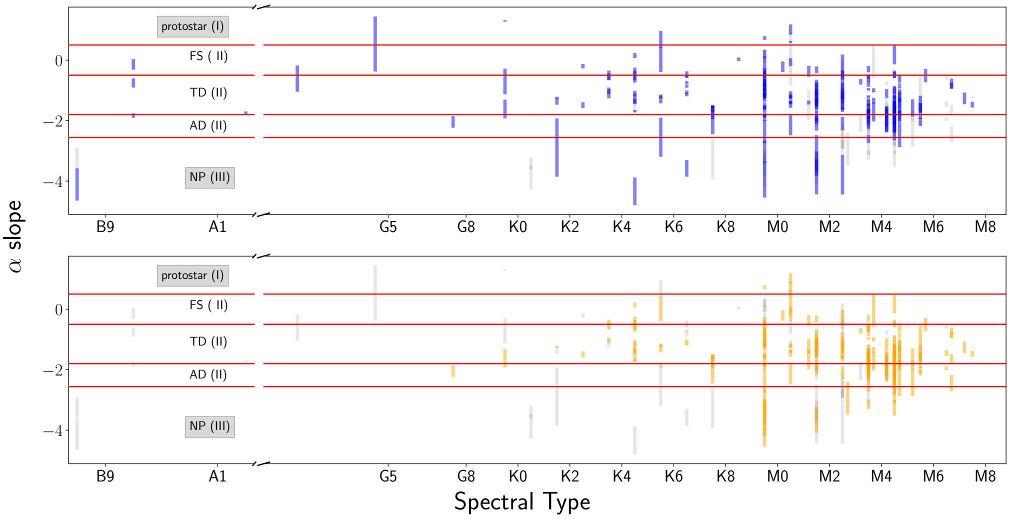

Figure 6.9: *Amplitude of the changes in the YSO classification slope using the 4 AllWISE bands W1-W4 as a function of the Spectral Type from Esplin and Luhman (2019).*

(set of random Gaussian distributed W1-W4 values) and get the mean YSO classification slope and the standard deviation. From this we can study how the YSO classification slope determinations change over the time span of the data and then get the average YSO classification slope and the amplitude (MAX(α)-MIN(α)) of these variations. Doing this enabled the classification of 307 sources, of which only 248 have data in more than one epoch. Because of this we only have amplitude values for the YSO classification slope for these 248 sources, but all 307 have classifications.

The distribution of the mean YSO classification slope is plotted in Figure 6.6. The vertical red lines represent the limits for the different classes. In this plot there is a slight decrease in the fraction of variables, both MIR and optical, in the tail of the distribution towards the **more evolved classes**. This points to thick disk, flat spectrum and class I classes presenting more sources with variability in the optical and MIR when compared to anaemic disk and naked photosphere classes. Figure 6.7 shows the sky distribution of the YSO classification attributed to the mean YSO classification slope derived for each source. Class I are found in almost all dense clouds in the complex; sources with thick or anaemic disks are found throughout the complex, with thick disk sources being the most common. Figure 6.7 also shows the total amount of sources within a specific class, with thick disk being the most abundant of the 5 classes with 167 sources.

We also found that the classifications presented in Figure 6.7 are not all constant in time, as the slope determinations change for all sources throughout the time span of AllWISE data. These changes in the YSO classification slope can be small and not change the class determination for that source, however 80 sources (32%) do change the class over the time span of the data. This number of sources which change classification is quite important as it can impact the determination of physical parameters such as the star formation rate (SFR; Chomiuk and Povich 2011). The SFR can be determined by a wide range of methods, all of which use different

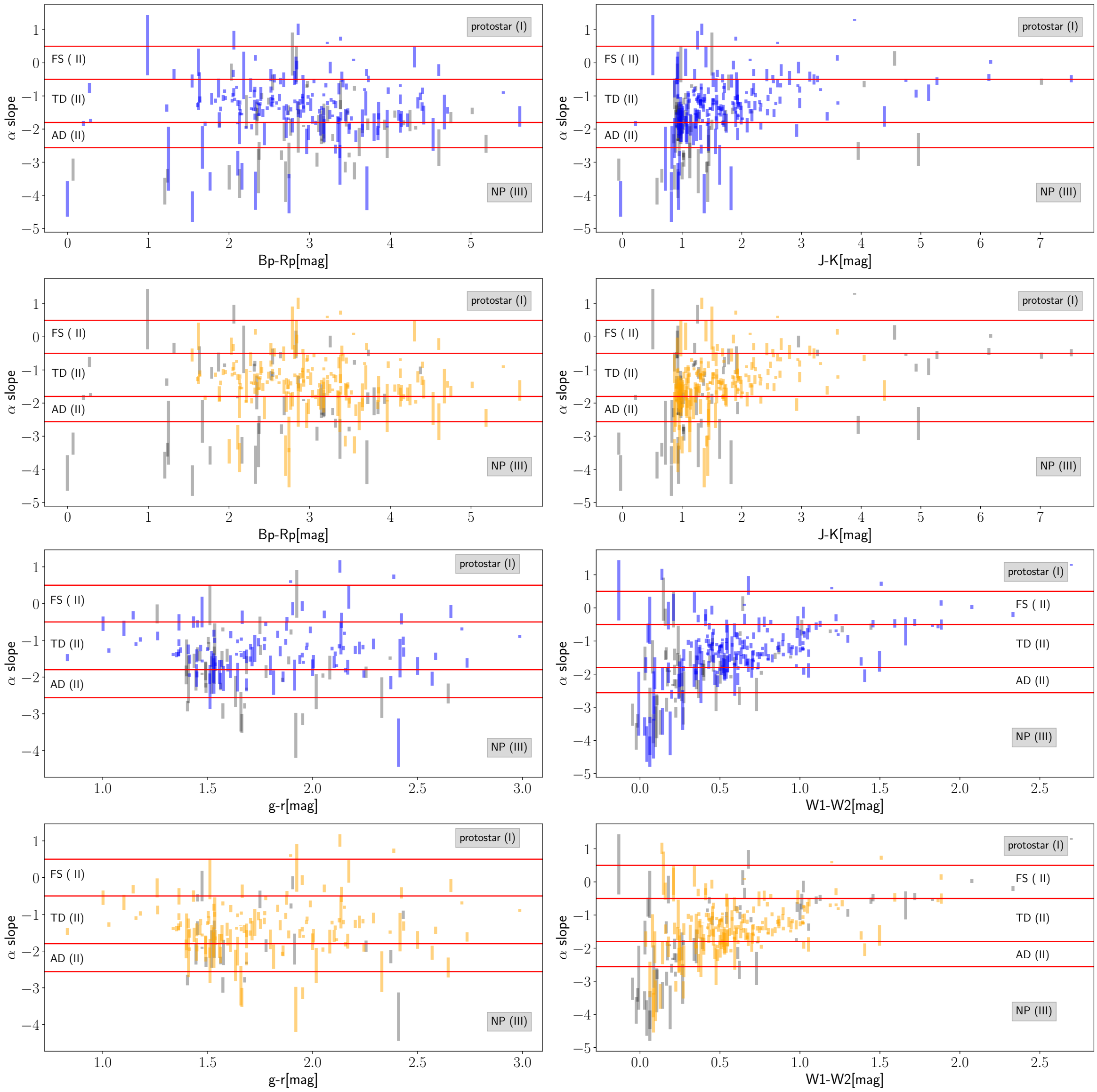

Figure 6.10: *Amplitude of the changes in the YSO classification slope determination using the 4 AllWISE bands W1-W4 as a function of the colors from the Gaia, ZTF and AllWISE surveys, plus the NIR photometry from Esplin and Luhman (2019). Blue bars are optical variables and the orange bar are the MIR variables while the full sample with measurements is plotted in grey. Red horizontal lines mark the limits of YSO classifications as defined in Teixeira et al. (2012) and explained in Section 2.1.2*

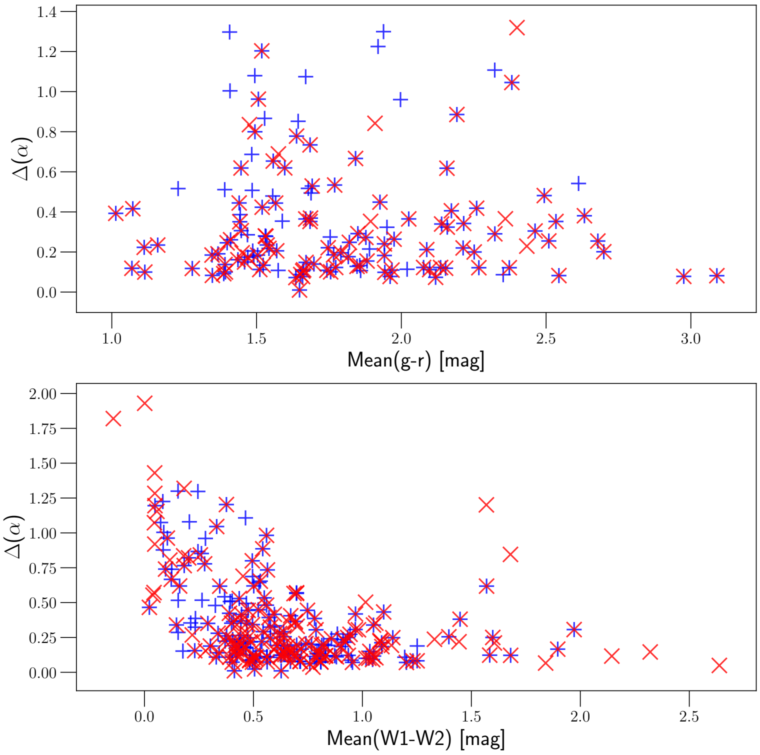

Figure 6.11: *Change of the YSO classification slope variations amplitude (MAX-MIN) as a function of the ZTF (g/r) and AllWISE (W1/W2) colors for the MIR and optical variables with data in W1-W4 in more than 1 epoch of data.*

ways to probe light resulting from star formation. In the Milky Way, because we can resolve YSOs, it is possible to estimate the SFR by counting YSOs (eg. Robitaille and Whitney 2010). The methodology employed for identifying YSOs is either through their NIR to MIR colours (Robitaille and Whitney 2010 use Spitzer colors) or through the slope of the stellar SED in the MIR, both of which are found to be affected by stellar variability in the YSOs in this work. This can change the number of determined YSO per class from one epoch of observations to the other, thus affecting the results from proto stellar counting.

Figure 6.8 shows the distribution of the amplitude (MAX(α)-MIN(α)) of the YSO classification slope which causes the change in class determination. The Figure also shows the distribution of α amplitudes for the MIR variables, the optical variables and the set of sources which change their classification over the time span of the data. We find that even small variations in the YSO classification slope can cause different determinations of the classes from Teixeira et al. (2012) and that the distributions is similar for both sets of variables. Most sources with high amplitudes do change their class.

To better present the changes in class determinations for our sources, we created Figures 6.9-6.10, in which we can observe each source represented by a vertical bar corresponding to the span between the maximum and the minimum YSO classification slope, which is centered around the mean α, as a function of the available colors and spectral type. Figure 6.9 shows that both large and small amplitudes in the YSO classification slope determination seem to be independent of the spectral type. In Figure 6.10, the NIR (first and second panel from the top, right column) and MIR plots (third and fourth panel from the top, right column) show that the reddest sources have lower amplitudes while the large amplitudes are towards the bluer colors, but in the Gaia (first and second panels from the top left column) and ZTF (third and fourth panels from the top left column) plots we see large amplitude sources being more scattered throughout the color space. Figure 6.11 shows the amplitude of the YSO classification slope itself, only for the MIR and optical variables, as a function of the g-r and W1-W2 colors. In the top panel (ZTF colors) we can see that most of the variables with high YSO classification slope amplitudes have $1.4 \lessapprox g - r \lessapprox 2.5$. This is the same color range in which most of the high brightness amplitude variables in g are located (see Figure 6.3). For the bottom panel in Figure 6.11 we see most of the large amplitudes in the determination of the YSO classification slope have $W1 - W2 \lessapprox 0.6$ mag, which is interesting being that most sources with high brightness amplitudes in W1 have $0.4 \lessapprox W1 - W2 \lessapprox 1.5$ (see Figure 6.3). Because we find that the primary origins for MIR variability should be primarily related to either variable extinction or variable accretion, we conclude that both of these phenomenon can significantly affect the YSO class determinations.

6.5 Color-Magnitude Variations

The way parameters such as temperature, mass or age are determined is by fitting theoretical models which relate the measurements (color, brightness) with the physical parameters. Variability can have an important influence on the determination of the aforementioned physical parameters. In this section we focus on discussing what the trajectories mapped by the source in a CMD due to its variability can tell us about the physical origin of these variations. We study the trajectories mapped by these sources using the concept of the CMD variability slope, which is the slope determined from the variations in the CMD of each source.

From Section 6.1 we know that the different possible origins of variability in YSOs can induce

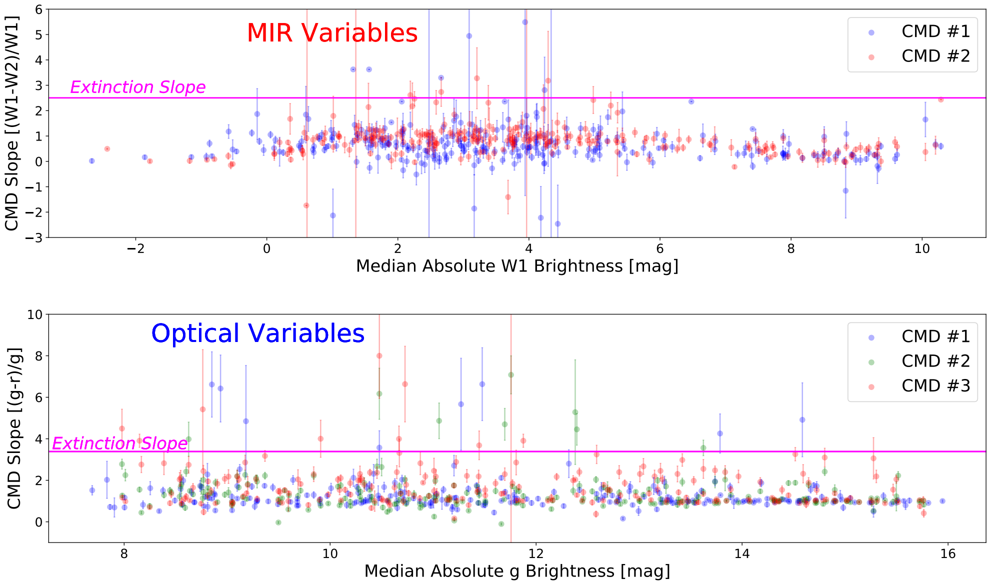

Figure 6.12: *CMD slopes for MIR and optical variables as a function of their absolute brightness, calculated from the Gaia eDR3 inverted parallaxes. The measurements for the different CMD are in different colors as indicated in the legend and the magenta horizontal line refers to the expected slope for the extinction. For the ZTF data, numbering for 1 to 3 refers to each year of ZTF data and for AllWISE numbering from 1 to 2 refers to the pre-cryo and post cryo data, respectively.*

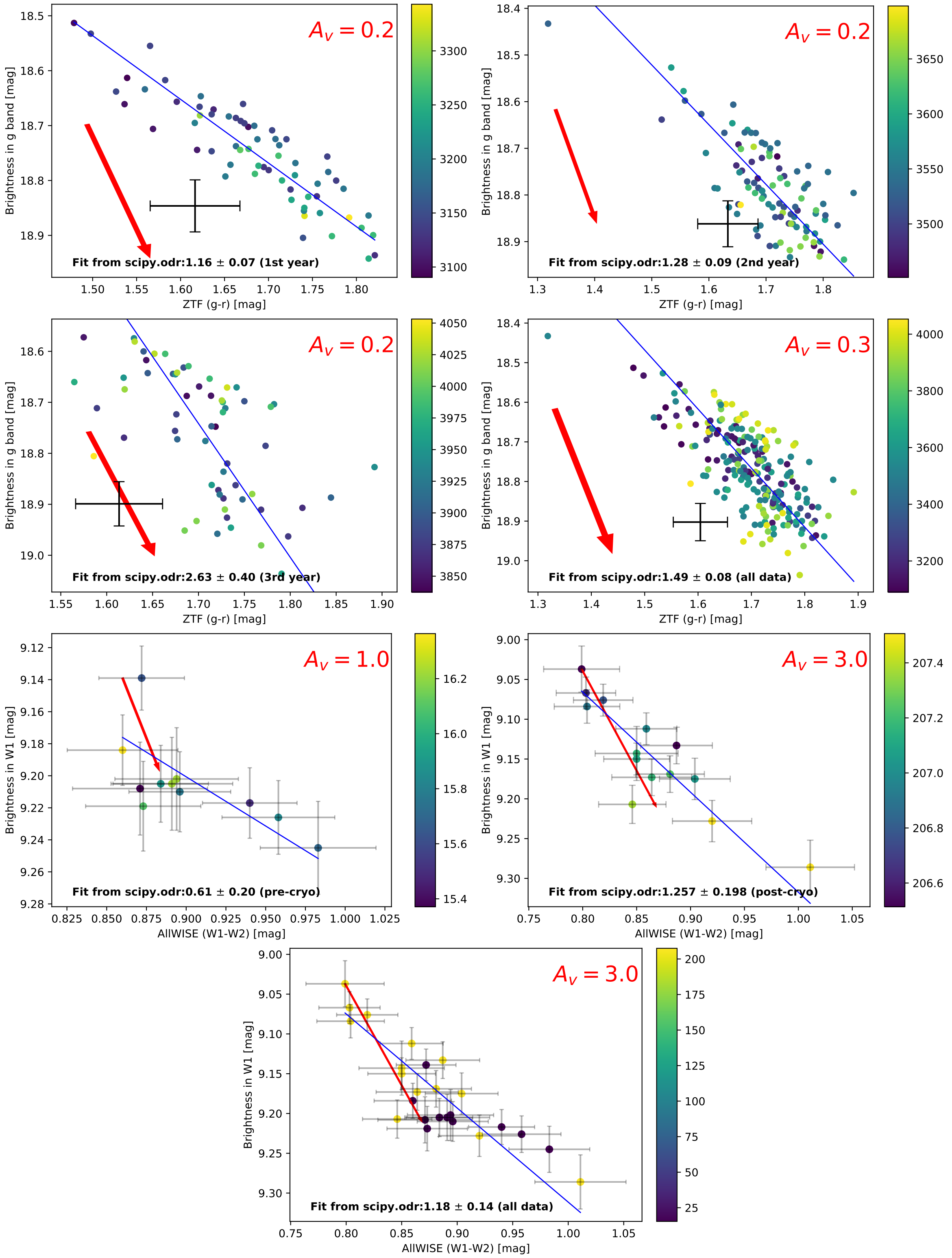

Figure 6.13: *Color-magnitude diagrams for the ZTF data of source #362 and AllWISE data of source #474. The blue line is the determined CMD variability slope, which is written in black at the bottom of each plot. An extinction vector is also drawn on each plot in red to contrast with the fit. In the ZTF plots (two top rows), the average error bars are plotted in the lower left corner to make the colored data more visible to the reader.*

CMD Slope	Variables	CMD	Number of Sources
$>A_V$	Opt	1	0 (-)
		2	1 (<1%)
		3	1 (<1%)
		full	4 (∼1%)
	MIR	1	3 (<1%)
		2	0 (-)
		full	0 (-)
$\sim A_V$	Opt	1	23 (∼8%)
		2	21 (∼7%)
		3	61 (∼21%)
		full	28 (∼10%)
	MIR	1	35 (∼8%)
		2	31 (∼7%)
		full	53 (∼12%)
$<A_V$	Opt	1	270 (∼92%)
		2	271 (∼92%)
		3	231(∼79%)
		full	261 (∼89%)
	MIR	1	402 (∼91%)
		2	409 (∼93%)
		full	387 (∼88%)

Table 6.2: *Number of sources with CMD slopes steeper, shallower or in agreement with the extinction vector within 3 σ. There is a clear preference for slopes shallower than the extinction in both sets of variables. For the ZTF data, numbering for 1 to 3 refers to each year of ZTF data and for AllWISE numbering from 1 to 2 refers to the pre-cryo and post cryo data, respectively.*

different properties in the light curves. Variable extinction should make the position of the source in a CMD change along the slope of the extinction vector. This can be easily studied by fitting a line to the CMD variations and comparing it to the extinction slope. Cold spots should produce colorless variability so their effect on CMD would be to imprint an almost vertical feature in which only the brightness changes. From the analysis in Section 6.3 we find that cold spots should not be the primary origin for variability in our optical and MIR variables due to no sources having the colorless variability we would expect (see Section 6.1). The other possibilities are hot spots and variable accretion/changes to the inner radii of the disk. The former will imprint changes along a specific slope in the CMD which is shallower than the extinction but still is "redder when fainter",the latter, however, will imprint changes that are "bluer when fainter".

To determine the CMD variability slope, we make use of the 2 available bands in ZTF, g and r, and in AllWISE during both days of observations, W1 and W2. For each epoch there are quasi simultaneous measurements in the previous photometric bands, thus for each epoch we have a measurement of both the g-r and W1-W2 colors. From here we get a color curve: information on how the color changes over the time span of the data. This information is then used along with the g and W1 measurements at that same time to create a position in the CMD. For ZTF we created a CMD for each yearly set of data in addition to the CMD with the whole 3 years of data as long as there are at least 10 data points; for AllWISE we created two

CMD, for the sets of data before and after the cryogen tank had depleted, plus the CMD with all of the available data, as long as there are at least 3 data points. To get the CMD variability slope we use the least squares linear regression method implemented in the Python package scipy.odr to get a slope determination taking into account the errors on both axis. We find that most of the YSOs in Taurus have variations in both optical and MIR CMDs that have determined CMD variability slopes shallower than the extinction vector (R_V=3.1) in those same CMDs. The numbers and percentages of sources which have a slope within 3σ of the extinction slope in the ZTF and AllWISE data are presented in Table 6.2 and the data in shown in Figure 6.12.

Figure 6.5 shows all the ZTF CMDs for source #362 (top two rows) which is a possible brown dwarf (spectral type M7.5) exhibiting quasi-periodical variations in its 3rd year of data (see Figure 4.8). From this example, we can see that even for a single star we may observe quite different sorts of behaviours. In the CMD for the first year of ZTF data (first panel from the top, left column) the source shows a CMD variability slope shallower than that of the extinction vector; in the second year of ZTF data (first panel from the top, right column) again we see a shallower CMD variability slope than that of the extinction vector, but this time it is slightly steeper than in the previous year of data. In the third year of ZTF data (second panel from the top, left column) we observe much more scatter in the CMD variations than in previous years and the CMD variability slope is now in agreement with the extinction vector, possibly pointing to variable extinction as the origin for the quasi-periodical variations. The CMD with all epochs of data for ZTF (second panel from the top, right column) reinforces that the overall CMD variations have a shallower CMD variability slope than that of the extinction

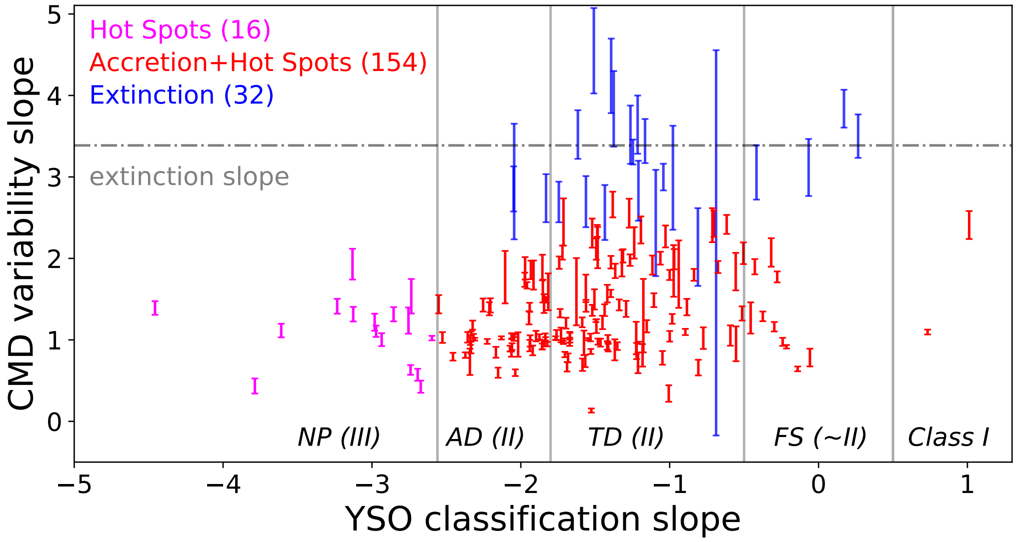

Figure 6.14: *Slope in the g vs g-r CMD plotted against the YSO classification slope determinations with the vertical grey lines marking the limits for the different classifications. In red we see the sources with slopes shallower than the extinction by 3σ that have disks, be it thick or anaemic ones; in magenta we see the sources with shallower slopes that do not have disks; in blue we see the sources which have CMD variability slopes in agreement with or steeper than the extinction. Dot-dashed horizontal grey line is the determined extinction vector slope in a g, (g-r) CMD. 5 sources with CMD variability slopes larger than 5 are left outside of the plot for better presentation and all of those sources are located within the TD class.*

vector.
The AllWISE CMDs (bottom two rows) in Figure 6.5 all show a CMD variability slope that is shallower than the extinction vector slope for the star presenting various VBs also featured in Figure 4.12, #474. Because this source shows VBs in its ZTF light curve and has a YSO classification from this work of thick disk it is possible that these shallower CMD variability slope are indicative of accretion phenomena. Source #362 does not have a classification from this work because its W4 measurements do not have associated uncertainties, however it is classified as class III in Esplin and Luhman (2019) (which is an equivalent classification to naked photosphere from the definitions in Teixeira et al. (2012)).

In Fig. 6.14 we show the relation between the YSO classification slope and the CMD variability slope calculated from all ZTF data points for each source. In this plot, we can try to pin-point the areas occupied by the sources sharing a common physical origin for variability. For the sources with the CMD variability slopes in agreement with or steeper than the extinction vector (in blue), even though accretion and hot spot activity may play a role, extinction should be the primary origin for their variability in the ZTF light curves. The variability in sources with CMD variability slopes shallower than the extinction vector may arise from both hots spots, or accretion. However, accretion is not expected to play a role in sources without an indication for the presence of a disk, so we separate the sources with shallower CMD variability slopes in the g vs g-r CMD by the determined YSO disk and disk-less classes. In red we see the sources which have CMD variability slopes shallower than the extinction vector slope by 3σ and also have disks according to our determinations of the YSO classification slope; the variability in these sources points to a mixed primary origin of hot spot activity and variable accretion. In magenta we see the disk-less sources which also had a CMD variability slope shallower than the extinction; for these sources accretion should not play a role due to the absence of an accretion disk. From this analysis we find that most sources in the ZTF data should have a primary origin for their variability in hot spots or accretion phenomena.

Chapter 7

Summary and Conclusions

In this thesis we present a study of long-term variability in the Taurus star forming region (SFR). We selected Taurus as one of the closest ($\sim$ 140pc) and youngest ($\sim$ 3Myr) star forming regions in the vicinity of the Sun. We created a catalogue of 491 spectroscopically confirmed members from the literature. These members might be related to different kinematic populations inside the Taurus clouds. The members of the Taurus SFR are also found to have a range of different classifications from the General Catalog of Variable Stars, from irregular variability to periodic variability.

For the sources in our catalog of confirmed members, we collect the optical multi-epoch data in g- and r-bands from ZTF and mid-infrared (W1 to W4) data from AllWISE. The two data sets do not overlap in time and therefore the analysis was done separately, however, information on variability and other properties from different wavelength regimes can be combined to draw conclusions about the physical mechanisms behind the observed variations. We then studied the shape of the optical light curves and noticed some emergent patterns. The light curves were divided into four observational classes: visual bursts (239 sources), visual dips (139 sources), quasi-periodicity (5 sources) and long timescale variability (11 sources). Some light curves defy simple classification either because of very fast variations, or simply because several possible origins for variability can affect the light curve **simultaneously**, thus creating irregular patterns difficult to classify. We find that visual bursts are the most common visual feature in the ZTF light curves. For the mid-infrared light curves we looked into how many sources have brightness jumps larger than 0.5 mag in W1 and W2, from the pre-cryo phase to the post-cryo phase, and find 7 and 4 such sources, respectively.

In order to select variable candidates, we apply five different statistical indices. We used χ^2_{red}, σ_w, A_{burst}, A_{dip}, and the Stetson J separately on photometry from each of the available bands and Welch-Stetson I on combined data from each survey. The number of selected candidates differs between the indices, due to the limitations in application and sensitivity of particular index or the data itself. We therefore combined the results by creating and applying additional rules:

- All sources selected as variable in the Welch-Stetson I are identified as variable.
- All sources not selected as variable in the Welch-Stetson I but selected as variable by at least 5 of the 10 available indices are also identified as variable.
- For sources with data in only one band (optical or mid-infrared), they are identified variable if they are selected by at least 3 of the 5 available indices.

Overall, we identify 304 variables in the optical (79% of the entire population) and 279 variables in the mid-infrared (62%); 188 YSO are classified as variable in both. By studying both sets of variables we find that neither show a preference towards specific brightness ranges or spectral types.

Several effects are imprinted in the light curves, from change of extinction, spot activity and accretion phenomena. To try to infer the possible primary origins for the variability observed in our sets of optical and mid-infrared variables, we inspect their brightness, colors, YSO class properties and the correlation between those. By studying the color variations, we find that neither set of variables shows evidence for a primary origin due to cold spots. We then look at the possible changes in the determination of the YSO classes as defined in Teixeira et al. (2012) and find that 80 (32%) do change class over the time span of the AllWISE data. We conclude that these changes should be primarily due to either extinction or accretion related phenomena. We see that along with the observed changes in brightness the sources also present color changes, which can be mapped in a color-magnitude diagrams (CMD). We examined the trajectories of our variable source on CMDs and apply least squares linear regression to measure the slope. By comparing the observed behaviour of the slope with analogous slopes obtained from toy models for spots and extinction and using the disk class determinations from AllWISE, we infer about the most probable origin of the variability in our sample. We find that:

- 32 sources with disks have slopes in the g vs g-r CMD in agreement with, or steeper, than the expected slope for the extinction. These sources should have a primary origin of variability due to **variable extinction**.
- 16 sources without disks have slopes in the g vs g-r CMD shallower than the extinction slope. We conclude that these sources should have a primary origin in variability due to **hot spots**.
- 154 sources with disks have slopes in the g vs g-r CMD which are shallower than the extinction slope. We conclude that these sources should have an origin for their variability due to both **hot spots** and **accretion**.

Our work presents the most complete study of long-term optical and MIR variability in the Taurus SFR, providing evidence for multiple origins in variability. Most members of the Taurus SFR show evidence for the presence of disks, which in addition to the aforementioned CMD properties point to accretion being the primary source for variability in these sources. We also find that the observed variability induces changes in the determination of the YSO classes that can impact physical parameters such as the star formation rate, which is crucial for our overall understanding of how star formation works.

References

Allard, F., Hauschildt, P. H., Alexander, D. R., Tamanai, A., and Schweitzer, A. (2001). The Limiting Effects of Dust in Brown Dwarf Model Atmospheres. *ApJ*, 556(1):357–372.

Allard, F., Homeier, D., and Freytag, B. (2011). Model Atmospheres From Very Low Mass Stars to Brown Dwarfs. In Johns-Krull, C., Browning, M. K., and West, A. A., editors, *16th Cambridge Workshop on Cool Stars, Stellar Systems, and the Sun*, volume 448 of *Astronomical Society of the Pacific Conference Series*, page 91.

Ambartsumian, V. A. (1954). On the Origin of Stars. In *Liege International Astrophysical Colloquia*, volume 5 of *Liege International Astrophysical Colloquia*, page 293.

Andrae, R., Schulze-Hartung, T., and Melchior, P. (2010). Dos and don'ts of reduced chi-squared. *arXiv e-prints*, page arXiv:1012.3754.

André, P. (1995). Low-Mass Protostars and Protostellar Stages. *Ap&SS*, 224(1-2):29–42.

Barenfeld, S. A., Carpenter, J. M., Ricci, L., and Isella, A. (2016). ALMA Observations of Circumstellar Disks in the Upper Scorpius OB Association. *APJ*, 827(2):142.

Beck, T. L., Schaefer, G. H., Guilloteau, S., Simon, M., Dutrey, A., Di Folco, E., and Chapillon, E. (2020). On the Nature of the T Tauri Triple System. *ApJ*, 902(2):132.

Beck, T. L. and Simon, M. (2001). The Variability of T Tauri, RY Tauri, and RW Aurigae from 1899 to 1952. *AJ*, 122(1):413–417.

Bellm, E. (2014). The Zwicky Transient Facility. In Wozniak, P. R., Graham, M. J., Mahabal, A. A., and Seaman, R., editors, *The Third Hot-wiring the Transient Universe Workshop*, pages 27–33.

Bertout, C., Basri, G., and Bouvier, J. (1988). Accretion Disks around T Tauri Stars. *ApJ*, 330:350.

Bertout, C. and Bouvier, J. (1989). T Tauri disk models. In *European Southern Observatory Conference and Workshop Proceedings*, volume 33 of *European Southern Observatory Conference and Workshop Proceedings*, pages 215–232.

Bouvier, J., Cabrit, S., Fernandez, M., Martin, E. L., and Matthews, J. M. (1993). COYOTES I : the photometric variability and rotational evolution of T Tauri stars. *A&A*, 272:176–206.

Bouvier, J., Chelli, A., Allain, S., Carrasco, L., Costero, R., Cruz-Gonzalez, I., Dougados, C., Fernández, M., Martín, E. L., Ménard, F., Mennessier, C., Mujica, R., Recillas, E., Salas, L., Schmidt, G., and Wichmann, R. (1999). Magnetospheric accretion onto the T Tauri star AA Tauri. I. Constraints from multisite spectrophotometric monitoring. *A&A*, 349:619–635.

Bouvier, J., Grankin, K. N., Alencar, S. H. P., Dougados, C., Fernández, M., Basri, G., Batalha, C., Guenther, E., Ibrahimov, M. A., Magakian, T. Y., Melnikov, S. Y., Petrov, P. P., Rud, M. V., and Zapatero Osorio, M. R. (2003). Eclipses by circumstellar material in the T Tauri star AA Tau. II. Evidence for non-stationary magnetospheric accretion. *A&A*, 409:169–192.

Bressan, A., Marigo, P., Girardi, L., Salasnich, B., Dal Cero, C., Rubele, S., and Nanni, A. (2012). Parsec: stellar tracks and isochrones with the padova and trieste stellar evolution code. *M. N. R. A. S.*, 427:127–145.

Burnham, S. W. (1890). Note on Hind's Variable Nebula in Taurus. *MNRAS*, 51:94.

Cardelli, J. A., Clayton, G. C., and Mathis, J. S. (1989). The Relationship between Infrared, Optical, and Ultraviolet Extinction. *ApJ*, 345:245.

Carpenter, J. M., Hillenbrand, L. A., and Skrutskie, M. F. (2001). Near-Infrared Photometric Variability of Stars toward the Orion A Molecular Cloud. *AJ*, 121(6):3160–3190.

Chandrasekhar, S. (1931). Xlviii. the density of white dwarf stars. *The London, Edinburgh, and Dublin Philosophical Magazine and Journal of Science*, 11(70):592–596.

Chomiuk, L. and Povich, M. S. (2011). Toward a Unification of Star Formation Rate Determinations in the Milky Way and Other Galaxies. *AJ*, 142(6):197.

Clark, D. H. and Stephenson, F. R. (1982). The Historical Supernovae. In Rees, M. J. and Stoneham, R. J., editors, *Supernovae: A Survey of Current Research*, volume 90 of *NATO Advanced Study Institute (ASI) Series C*, pages 355–370.

Cunningham, C. J. (2020). 'Dark stars' and a new interpretation of the ancient Greek stellar magnitude system. *Journal of Astronomical History and Heritage*, 23(2):231–256.

Cutri, R. M., Wright, E. L., Conrow, T., Fowler, J. W., Eisenhardt, P. R. M., Grillmair, C., Kirkpatrick, J. D., Masci, F., McCallon, H. L., Wheelock, S. L., Fajardo-Acosta, S., Yan, L., Benford, D., Harbut, M., Jarrett, T., Lake, S., Leisawitz, D., Ressler, M. E., Stanford, S. A., Tsai, C. W., Liu, F., Helou, G., Mainzer, A., Gettngs, D., Gonzalez, A., Hoffman, D., Marsh, K. A., Padgett, D., Skrutskie, M. F., Beck, R., Papin, M., and Wittman, M. (2021). VizieR Online Data Catalog: AllWISE Data Release (Cutri+ 2013). *VizieR Online Data Catalog*, page II/328.

D'Antona, F. and Mazzitelli, I. (1997). Evolution of low mass stars. *MmSAI*, 68:807–822.

Dodin, A. V. (2015). Non-LTE modeling of the structure and spectra of hot accretion spots on the surface of young stars. *Astronomy Letters*, 41(5):196–210.

Esplin, T. L. and Luhman, K. L. (2017). A Survey For Planetary-mass Brown Dwarfs in the Taurus and Perseus Star-forming Regions. *AJ*, 154(4):134.

Esplin, T. L. and Luhman, K. L. (2019). A Survey for New Members of Taurus from Stellar to Planetary Masses. *AJ*, 158(2):54.

Fleming, G. D., Kirk, J. M., Ward-Thompson, D., and Pattle, K. (2019). Revealing the Two 'Horns' of Taurus with GAIA DR2. *arXiv e-prints*, page arXiv:1904.06980.

Flores, C., Reipurth, B., and Connelley, M. S. (2020). Is T Tauri North a "Classical" T Tauri Star? *ApJ*, 898(2):109.

Froebrich, D., Campbell-White, J., Scholz, A., Eislöffel, J., Zegmott, T., Billington, S. J., Donohoe, J., Makin, S. V., Hibbert, R., Newport, R. J., Pickard, R., Quinn, N., Rodda, T., Piehler, G., Shelley, M., Parkinson, S., Wiersema, K., and Walton, I. (2018). A survey for variable young stars with small telescopes: First results from HOYS-CAPS. *MNRAS*, 478(4):5091–5103.

Gaia Collaboration, Brown, A. G. A., Vallenari, A., Prusti, T., de Bruijne, J. H. J., Babusiaux, C., and Bailer-Jones, C. A. L. (2018). Gaia Data Release 2. Summary of the contents and survey properties. *A&A*, 616:A1.

Gaia Collaboration, Brown, A. G. A., Vallenari, A., Prusti, T., de Bruijne, J. H. J., Babusiaux, C., Biermann, M., Creevey, O. L., Evans, D. W., Eyer, L., Hutton, A., Jansen, F., Jordi, C., Klioner, S. A., Lammers, U., Lindegren, L., Luri, X., Mignard, F., Panem, C., Pourbaix, D., Randich, S., Sartoretti, P., Soubiran, C., Walton, N. A., Arenou, F., Bailer-Jones, C. A. L., Bastian, U., Cropper, M., Drimmel, R., Katz, D., Lattanzi, M. G., van Leeuwen, F., Bakker, J., Cacciari, C., Castañeda, J., De Angeli, F., Ducourant, C., Fabricius, C., Fouesneau, M., Frémat, Y., Guerra, R., Guerrier, A., Guiraud, J., Jean-Antoine Piccolo, A., Masana, E., Messineo, R., Mowlavi, N., Nicolas, C., Nienartowicz, K., Pailler, F., Panuzzo, P., Riclet, F., Roux, W., Seabroke, G. M., Sordo, R., Tanga, P., Thévenin, F., Gracia-Abril, G., Portell, J., Teyssier, D., Altmann, M., Andrae, R., Bellas-Velidis, I., Benson, K., Berthier, J., Blomme, R., Brugaletta, E., Burgess, P. W., Busso, G., Carry, B., Cellino, A., Cheek, N., Clementini, G., Damerdji, Y., Davidson, M., Delchambre, L., Dell'Oro, A., Fernández-Hernández, J., Galluccio, L., García-Lario, P., Garcia-Reinaldos, M., González-Núñez, J., Gosset, E., Haigron, R., Halbwachs, J. L., Hambly, N. C., Harrison, D. L., Hatzidimitriou, D., Heiter, U., Hernández, J., Hestroffer, D., Hodgkin, S. T., Holl, B., Janßen, K., Jevardat de Fombelle, G., Jordan, S., Krone-Martins, A., Lanzafame, A. C., Löffler, W., Lorca, A., Manteiga, M., Marchal, O., Marrese, P. M., Moitinho, A., Mora, A., Muinonen, K., Osborne, P., Pancino, E., Pauwels, T., Petit, J. M., Recio-Blanco, A., Richards, P. J., Riello, M., Rimoldini, L., Robin, A. C., Roegiers, T., Rybizki, J., Sarro, L. M., Siopis, C., Smith, M., Sozzetti, A., Ulla, A., Utrilla, E., van Leeuwen, M., van Reeven, W., Abbas, U., Abreu Aramburu, A., Accart, S., Aerts, C., Aguado, J. J., Ajaj, M., Altavilla, G., Álvarez, M. A., Álvarez Cid-Fuentes, J., Alves, J., Anderson, R. I., Anglada Varela, E., Antoja, T., Audard, M., Baines, D., Baker, S. G., Balaguer-Núñez, L., Balbinot, E., Balog, Z., Barache, C., Barbato, D., Barros, M., Barstow, M. A., Bartolomé, S., Bassilana, J. L., Bauchet, N., Baudesson-Stella, A., Becciani, U., Bellazzini, M., Bernet, M., Bertone, S., Bianchi, L., Blanco-Cuaresma, S., Boch, T., Bombrun, A., Bossini, D., Bouquillon, S., Bragaglia, A., Bramante, L., Breedt, E., Bressan, A., Brouillet, N., Bucciarelli, B., Burlacu, A., Busonero, D., Butkevich, A. G., Buzzi, R., Caffau, E., Cancelliere, R., Cánovas, H., Cantat-Gaudin, T., Carballo, R., Carlucci, T., Carnerero, M. I., Carrasco, J. M., Casamiquela, L., Castellani, M., Castro-Ginard, A., Castro Sampol, P., Chaoul, L., Charlot, P., Chemin, L., Chiavassa, A., Cioni, M. R. L., Comoretto, G., Cooper, W. J., Cornez, T., Cowell, S., Crifo, F., Crosta, M., Crowley, C., Dafonte, C., Dapergolas, A., David, M., David, P., de Laverny, P., De Luise, F., De March, R., De Ridder, J., de Souza, R., de Teodoro, P., de Torres, A., del Peloso, E. F., del Pozo, E., Delbo, M., Delgado, A., Delgado, H. E., Delisle, J. B., Di Matteo, P., Diakite, S., Diener, C., Distefano, E., Dolding, C., Eappachen, D., Edvardsson, B., Enke, H., Esquej, P., Fabre, C., Fabrizio, M., Faigler, S., Fedorets, G., Fernique, P., Fienga, A., Figueras, F., Fouron, C., Fragkoudi, F., Fraile, E., Franke, F., Gai, M., Garabato, D., Garcia-Gutierrez, A., García-Torres, M., Garofalo, A., Gavras, P., Gerlach, E., Geyer, R., Giacobbe, P., Gilmore, G., Girona, S., Giuffrida, G., Gomel, R., Gomez, A., Gonzalez-Santamaria, I., González-Vidal, J. J., Granvik, M., Gutiérrez-Sánchez, R., Guy, L. P., Hauser, M., Haywood, M., Helmi, A., Hidalgo, S. L., Hilger, T., Hładczuk, N., Hobbs, D., Holland, G., Huckle, H. E., Jasniewicz, G., Jonker, P. G., Juaristi Campillo, J., Julbe, F., Karbevska, L., Kervella, P., Khanna, S., Kochoska, A., Kontizas, M., Kordopatis, G., Korn, A. J., Kostrzewa-Rutkowska, Z., Kruszyńska, K., Lambert, S., Lanza, A. F., Lasne, Y., Le Campion, J. F., Le Fustec, Y., Lebreton, Y., Lebzelter, T., Leccia, S., Leclerc, N., Lecoeur-Taibi, I., Liao, S., Licata, E., Lindstrøm, E. P., Lister, T. A., Livanou, E., Lobel, A., Madrero Pardo, P., Managau, S., Mann, R. G., Marchant, J. M., Marconi, M., Marcos Santos, M. M. S., Marinoni, S., Marocco, F., Marshall, D. J., Martin Polo, L., Martín-Fleitas, J. M., Masip, A., Massari, D., Mastrobuono-Battisti, A., Mazeh, T., McMillan, P. J., Messina, S., Michalik, D., Millar, N. R., Mints, A., Molina, D., Molinaro, R., Molnár, L., Montegriffo, P., Mor, R., Morbidelli, R., Morel, T., Morris, D., Mulone, A. F., Munoz, D., Muraveva, T., Murphy, C. P., Musella, I., Noval, L., Ordénovic, C., Orrù, G., Osinde, J., Pagani, C., Pagano, I., Palaversa, L., Palicio, P. A., Panahi, A., Pawlak, M., Peñalosa Esteller, X., Penttilä, A., Piersimoni, A. M., Pineau, F. X., Plachy, E., Plum, G., Poggio, E., Poretti, E., Poujoulet, E., Prša, A., Pulone, L., Racero, E., Ragaini, S., Rainer, M., Raiteri, C. M., Rambaux, N., Ramos, P., Ramos-Lerate, M., Re Fiorentin, P., Regibo, S., Reylé, C., Ripepi, V., Riva, A., Rixon, G., Robichon, N., Robin, C., Roelens, M., Rohrbasser, L., Romero-Gómez, M., Rowell, N., Royer, F., Rybicki, K. A., Sadowski, G., Sagristà Sellés, A., Sahlmann, J., Salgado, J., Salguero, E., Samaras, N., Sanchez Gimenez, V., Sanna, N., Santoveña, R., Sarasso, M., Schultheis, M., Sciacca, E., Segol, M., Segovia, J. C., Ségransan, D., Semeux, D., Shahaf, S., Siddiqui, H. I., Siebert, A., Siltala, L., Slezak, E., Smart, R. L., Solano, E., Solitro, F., Souami, D., Souchay, J., Spagna, A., Spoto, F., Steele, I. A., Steidelmüller, H., Stephenson, C. A., Süveges, M., Szabados, L., Szegedi-Elek, E., Taris, F., Tauran, G., Taylor, M. B., Teixeira, R., Thuillot, W., Tonello, N., Torra, F., Torra, J., Turon, C., Unger, N., Vaillant, M., van Dillen, E., Vanel, O., Vecchiato, A., Viala, Y., Vicente, D., Voutsinas, S., Weiler, M., Wevers, T., Wyrzykowski, Ł., Yoldas, A., Yvard, P., Zhao, H., Zorec, J., Zucker, S., Zurbach, C., and Zwitter, T. (2021). Gaia Early Data Release 3. Summary of the contents and survey properties. *A&A*, 649:A1.

Galli, P. A. B., Loinard, L., Bouy, H., Sarro, L. M., Ortiz-León, G. N., Dzib, S. A., Olivares, J., Heyer, M., Hernandez, J., Román-Zúñiga, C., Kounkel, M., and Covey, K. (2019). Structure and kinematics of the Taurus star-forming region from Gaia-DR2 and VLBI astrometry. *A&A*, 630:A137.

Goodricke, J. (1786). Ii. a series of observations on, and a discovery of, the period of the variation of the light of the star marked δ by bayer, near the head of cepheus. in a letter from john goodricke, esq. to nevil maskelyne, d.d. f. r. s. *Philosophical Transactions of the Royal Society of London*, 76:48–61.

Greene, T. P. and Lada, C. J. (2002). Spectroscopic Detection of a Stellar-like Photosphere in an Accreting Protostar. *AJ*, 124(4):2185–2193.

Grinin, V. P., Rostopchina, A. N., and Shakhovskoi, D. N. (1998). On the nature of cyclic light variations in UX Ori stars. *Astronomy Letters*, 24(6):802–807.

Hartmann, L., Hewett, R., and Calvet, N. (1994). Magnetospheric Accretion Models for T Tauri Stars. I. Balmer Line Profiles without Rotation. *ApJ*, 426:669.

Hayashi, C. (1966). Evolution of Protostars. *ARA&A*, 4:171.

Herbig, G. H. (1962). The Properties and Problems of T Tauri Stars and Related Objects. *Advances in Astronomy and Astrophysics*, 1:47–103.

Herbig, G. H. (1977). Eruptive phenomena in early stellar evolution. *ApJ*, 217:693–715.

Herbst, W., Herbst, D. K., Grossman, E. J., and Weinstein, D. (1994). Catalogue of UBVRI Photometry of T Tauri Stars and Analysis of the Causes of Their Variability. *AJ*, 108:1906.

Herczeg, G. J. and Hillenbrand, L. A. (2014). An Optical Spectroscopic Study of T Tauri Stars. I. Photospheric Properties. *ApJ*, 786(2):97.

Hertzsprung, E. (1911). Ueber die Verwendung photographischer effektiver Wellenlaengen zur Bestimmung von Farbenaequivalenten. *Publikationen des Astrophysikalischen Observatoriums zu Potsdam*, 63.

Hillenbrand, L. A., Reipurth, B., Connelley, M., Cutri, R. M., and Isaacson, H. (2019). Gaia 19ajj: A Young Star Brightening Due to Enhanced Accretion and Reduced Extinction. *AJ*, 158(6):240.

Hind, J. R. (1864). Note on the Variable Nebula in Taurus. *MNRAS*, 24:65.

Hoffleit, D. (1997). History of the Discovery of Mira Stars. *Journal of the American Association of Variable Star Observers (JAAVSO)*, 25(2):115–136.

Jetsu, L., Porceddu, S., Lyytinen, J., Kajatkari, P., Lehtinen, J., Markkanen, T., and Toivari-Viitala, J. (2013). Did the Ancient Egyptians Record the Period of the Eclipsing Binary Algol—The Raging One? *ApJ*, 773(1):1.

Joy, A. H. (1945). T Tauri Variable Stars. *ApJ*, 102:168.

Koenig, X. P., Leisawitz, D. T., Benford, D. J., Rebull, L. M., Padgett, D. L., and Assef, R. J. (2012). Wide-field Infrared Survey Explorer Observations of the Evolution of Massive Star-forming Regions. *ApJ*, 744(2):130.

Koenigl, A. (1991). Disk Accretion onto Magnetic T Tauri Stars. *ApJL*, 370:L39.

Köhler, R. (2021). The 3-dimensional structure of the prototypical young system T Tauri. In *The 20.5th Cambridge Workshop on Cool Stars, Stellar Systems, and the Sun (CS20.5)*, Cambridge Workshop on Cool Stars, Stellar Systems, and the Sun, page 313.

Krolikowski, D. M., Kraus, A. L., and Rizzuto, A. C. (2021). Gaia EDR3 Reveals the Substructure and Complicated Star Formation History of the Greater Taurus-Auriga Star Forming Complex. *arXiv e-prints*, page arXiv:2105.13370.

Köhler, R. and Kubiak, K. (2020). Photometric variability of t tauri s as a probe for circumstellar material. *Research Notes of the AAS*, 4(5):73.

Lada, C. J. (1987). Star formation: from OB associations to protostars. In Peimbert, M. and Jugaku, J., editors, *Star Forming Regions*, volume 115, page 1.

Lada, C. J. and Lada, E. A. (2003). Embedded Clusters in Molecular Clouds. *ARA&A*, 41:57–115.

Lada, C. J., Muench, A. A., Luhman, K. L., Allen, L., Hartmann, L., Megeath, T., Myers, P., Fazio, G., Wood, K., Muzerolle, J., Rieke, G., Siegler, N., and Young, E. (2006). Spitzer Observations of IC 348: The Disk Population at 2-3 Million Years. *AJ*, 131(3):1574–1607.

Lawrence, A., Warren, S. J., Almaini, O., Edge, A. C., Hambly, N. C., Jameson, R. F., Lucas, P., Casali, M., Adamson, A., Dye, S., Emerson, J. P., Foucaud, S., Hewett, P., Hirst, P., Hodgkin, S. T., Irwin, M. J., Lodieu, N., McMahon, R. G., Simpson, C., Smail, I., Mortlock, D., and Folger, M. (2007). The UKIRT Infrared Deep Sky Survey (UKIDSS). *MNRAS*, 379(4):1599–1617.

Liu, J., Fang, M., Tian, H., Liu, C., Yang, C., and Xue, X. (2021). The Old Moving Groups in the Field of Taurus. *ApJS*, 254(1):20.

Long, F., Herczeg, G. J., Harsono, D., Pinilla, P., Tazzari, M., Manara, C. F., Pascucci, I., Cabrit, S., Nisini, B., Johnstone, D., Edwards, S., Salyk, C., Menard, F., Lodato, G., Boehler, Y., Mace, G. N., Liu, Y., Mulders, G. D., Hendler, N., Ragusa, E., Fischer, W. J., Banzatti, A., Rigliaco, E., van de Plas, G., Dipierro, G., Gully-Santiago, M., and Lopez-Valdivia, R. (2019). Compact Disks in a High-resolution ALMA Survey of Dust Structures in the Taurus Molecular Cloud. *ApJ*, 882(1):49.

Long, F., Pinilla, P., Herczeg, G. J., Harsono, D., Dipierro, G., Pascucci, I., Hendler, N., Tazzari, M., Ragusa, E., Salyk, C., Edwards, S., Lodato, G., van de Plas, G., Johnstone, D., Liu, Y., Boehler, Y., Cabrit, S., Manara, C. F., Menard, F., Mulders, G. D., Nisini, B., Fischer, W. J., Rigliaco, E., Banzatti, A., Avenhaus, H., and Gully-Santiago, M. (2018). Gaps and Rings in an ALMA Survey of Disks in the Taurus Star-forming Region. *ApJ*, 869(1):17.

Luhman, K. L. (2018). The Stellar Membership of the Taurus Star-forming Region. *AJ*, 156(6):271.

Luhman, K. L., Allen, P. R., Espaillat, C., Hartmann, L., and Calvet, N. (2010). The Disk Population of the Taurus Star-Forming Region. *ApJS*, 186(1):111–174.

Luhman, K. L., Mamajek, E. E., Shukla, S. J., and Loutrel, N. P. (2017). A Survey for New Members of the Taurus Star-forming Region with the Sloan Digital Sky Survey. *AJ*, 153(1):46.

Mainzer, A., Bauer, J., Grav, T., Masiero, J., Cutri, R. M., Dailey, J., Eisenhardt, P., McMillan, R. S., Wright, E., Walker, R., Jedicke, R., Spahr, T., Tholen, D., Alles, R., Beck, R., Brandenburg, H., Conrow, T., Evans, T., Fowler, J., Jarrett, T., Marsh, K., Masci, F., McCallon, H., Wheelock, S., Wittman, M., Wyatt, P., DeBaun, E., Elliott, G., Elsbury, D., Gautier, T., I., Gomillion, S., Leisawitz, D., Maleszewski, C., Micheli, M., and Wilkins, A. (2011). Preliminary Results from NEOWISE: An Enhancement to the Wide-field Infrared Survey Explorer for Solar System Science. *ApJ*, 731(1):53.

Marrese, P. M., Marinoni, S., Fabrizio, M., and Altavilla, G. (2019). Gaia Data Release 2. Cross-match with external catalogues: algorithms and results. *A&A*, 621:A144.

Masci, F. J., Laher, R. R., Rusholme, B., Shupe, D. L., Groom, S., Surace, J., Jackson, E., Monkewitz, S., Beck, R., Flynn, D., Terek, S., Landry, W., Hacopians, E., Desai, V., Howell, J., Brooke, T., Imel, D., Wachter, S., Ye, Q.-Z., Lin, H.-W., Cenko, S. B., Cunningham, V., Rebbapragada, U., Bue, B., Miller, A. A., Mahabal, A., Bellm, E. C., Patterson, M. T., Jurić, M., Golkhou, V. Z., Ofek, E. O., Walters, R., Graham, M., Kasliwal, M. M., Dekany, R. G., Kupfer, T., Burdge, K., Cannella, C. B., Barlow, T., Van Sistine, A., Giomi, M., Fremling, C., Blagorodnova, N., Levitan, D., Riddle, R., Smith, R. M., Helou, G., Prince, T. A., and Kulkarni, S. R. (2019). The Zwicky Transient Facility: Data Processing, Products, and Archive. *PASP*, 131(995):018003.

Mathis, J. S. (1990). Interstellar dust and extinction. *ARA&A*, 28:37–70.

Matt, S. and Böhm, K.-H. (2003). The Enigmatic HH 255. *PASP*, 115(805):334–341.

Meyer, M. R., Calvet, N., and Hillenbrand, L. A. (1997). Intrinsic Near-Infrared Excesses of T Tauri Stars: Understanding the Classical T Tauri Star Locus. *AJ*, 114:288–300.

Muench, A. A., Lada, C. J., Luhman, K. L., Muzerolle, J., and Young, E. (2007). A Spitzer Census of the IC 348 Nebula. *AJ*, 134(1):411–444.

Mužić, K., Scholz, A., Geers, V., Fissel, L., and Jayawardhana, R. (2011). Substellar Objects in Nearby Young Clusters (SONYC). III. Chamaeleon-I. *ApJ*, 732(2):86.

Pettersson, B. (2008). Young stars and dust clouds in puppis and vela. *The Handbook of Star forming Regions*, Vol II: The Southern Sky:p. 43.

Planck Collaboration (2016). Planck 2015 results. XI. CMB power spectra, likelihoods, and robustness of parameters. *AAP*, 594:A11.

Pogson, N. (1856). Magnitudes of Thirty-six of the Minor Planets for the first day of each month of the year 1857. *MNRAS*, 17:12–15.

Rebull, L. M., Cody, A. M., Covey, K. R., Günther, H. M., Hillenbrand, L. A., Plavchan, P., Poppenhaeger, K., Stauffer, J. R., Wolk, S. J., Gutermuth, R., Morales-Calderón, M., Song, I., Barrado, D., Bayo, A., James, D., Hora, J. L., Vrba, F. J., Alves de Oliveira, C., Bouvier, J., Carey, S. J., Carpenter, J. M., Favata, F., Flaherty, K., Forbrich, J., Hernandez, J., McCaughrean, M. J., Megeath, S. T., Micela, G., Smith, H. A., Terebey, S., Turner, N., Allen, L., Ardila, D., Bouy, H., and Guieu, S. (2014). Young Stellar Object VARiability (YSOVAR): Long Timescale Variations in the Mid-infrared. *AJ*, 148(5):92.

Rebull, L. M., Padgett, D. L., McCabe, C. E., Hillenbrand, L. A., Stapelfeldt, K. R., Noriega-Crespo, A., Carey, S. J., Brooke, T., Huard, T., Terebey, S., Audard, M., Monin, J. L., Fukagawa, M., Güdel, M., Knapp, G. R., Menard, F., Allen, L. E., Angione, J. R., Baldovin-Saavedra, C., Bouvier, J., Briggs, K., Dougados, C., Evans, N. J., Flagey, N., Guieu, S., Grosso, N., Glauser, A. M., Harvey, P., Hines, D., Latter, W. B., Skinner, S. L., Strom, S., Tromp, J., and Wolf, S. (2010). The Taurus Spitzer Survey: New Candidate Taurus Members Selected Using Sensitive Mid-Infrared Photometry. *ApJS*, 186(2):259–307.

Reipurth, B. and Heathcote, S. (1997). 50 Years of Herbig-Haro Research. From discovery to HST. In Reipurth, B. and Bertout, C., editors, *Herbig-Haro Flows and the Birth of Stars*, volume 182, pages 3–18.

Robitaille, T. P. and Whitney, B. A. (2010). The Present-Day Star Formation Rate of the Milky Way Determined from Spitzer-Detected Young Stellar Objects. *ApJL*, 710(1):L11–L15.

Robitaille, T. P., Whitney, B. A., Indebetouw, R., Wood, K., and Denzmore, P. (2006). Interpreting Spectral Energy Distributions from Young Stellar Objects. I. A Grid of 200,000 YSO Model SEDs. *ApJS*, 167(2):256–285.

Roccatagliata, V., Franciosini, E., Sacco, G. G., Randich, S., and Sicilia-Aguilar, A. (2020). A 3D view of the Taurus star-forming region by Gaia and Herschel. Multiple populations related to the filamentary molecular cloud. *A&A*, 638:A85.

Rosenberg, H. (1910). Über den zusammenhang von helligkeit und spektraltypus in den plejaden. *Astronomische Nachrichten*, 186(5):71–78.

Russell, H. N. (1914). Relations Between the Spectra and Other Characteristics of the Stars. *Popular Astronomy*, 22:275–294.

Samus', N. N., Kazarovets, E. V., Durlevich, O. V., Kireeva, N. N., and Pastukhova, E. N. (2017). General catalogue of variable stars: Version GCVS 5.1. *Astronomy Reports*, 61(1):80–88.

Scholz, A., Eislöffel, J., and Mundt, R. (2009). Long-term monitoring in IC4665: fast rotation and weak variability in very low mass objects. *MNRAS*, 400(3):1548–1562.

Schwartz, R. D. (1975). T Tauri nebulae and Herbig-Haro nebulae: evidence for excitation by a strong stellar wind. *ApJ*, 195:631–642.

Schwartz, R. D. (1983). Herbig-haro objects. *ARA&A*, 21:209–237.

Skrutskie, M. F., Cutri, R. M., Stiening, R., Weinberg, M. D., Schneider, S., Carpenter, J. M., Beichman, C., Capps, R., Chester, T., Elias, J., Huchra, J., Liebert, J., Lonsdale, C., Monet, D. G., Price, S., Seitzer, P., Jarrett, T., Kirkpatrick, J. D., Gizis, J. E., Howard, E., Evans, T., Fowler, J., Fullmer, L., Hurt, R., Light, R., Kopan, E. L., Marsh, K. A., McCallon, H. L., Tam, R., Van Dyk, S., and Wheelock, S. (2006). The Two Micron All Sky Survey (2MASS). 131:1163–1183.

Sokolovsky, K. V., Gavras, P., Karampelas, A., Antipin, S. V., Bellas-Velidis, I., Benni, P., Bonanos, A. Z., Burdanov, A. Y., Derlopa, S., Hatzidimitriou, D., Khokhryakova, A. D., Kolesnikova, D. M., Korotkiy, S. A., Lapukhin, E. G., Moretti, M. I., Popov, A. A., Pouliasis, E., Samus, N. N., Spetsieri, Z., Veselkov, S. A., Volkov, K. V., Yang, M., and Zubareva, A. M. (2017). Comparative performance of selected variability detection techniques in photometric time series data. *MNRAS*, 464(1):274–292.

Stetson, P. B. (1996). On the Automatic Determination of Light-Curve Parameters for Cepheid Variables. *PASP*, 108:851.

Strand, K. A. (1968). Ejnar Hertzsprung, 1873-1967. *PASP*, 80(472):51.

Teixeira, P. S., Lada, C. J., Marengo, M., and Lada, E. A. (2012). Spitzer observations of NGC 2264: the nature of the disk population. *A&A*, 540:A83.

van den Ancker, M. E., The, P. S., Feinstein, A., Vazquez, R. A., de Winter, D., and Perez, M. R. (1997). A multiwavelength study of star formation in the very young open cluster NGC 6530. *A&AS*, 123:63–82.

van Roestel, J., Duev, D. A., Mahabal, A. A., Coughlin, M. W., Mróz, P., Burdge, K., Drake, A., Graham, M. J., Hillenbrand, L., Bellm, E. C., Kupfer, T., Delacroix, A., Fremling, C., Golkhou, V. Z., Hale, D., Laher, R. R., Masci, F. J., Riddle, R., Rosnet, P., Rusholme, B., Smith, R., Soumagnac, M. T., Walters, R., Prince, T. A., and Kulkarni, S. R. (2021). The ZTF Source Classification Project. I. Methods and Infrastructure. *AJ*, 161(6):267.

Vrba, F. J., Chugainov, P. F., Weaver, W. B., and Stauffer, J. S. (1993). Photometric and Spectroscopic Monitoring of AA Tau, DN Tau, UX Tau A, T Tau, RY Tau, LK CA 4, and LK CA 7. *AJ*, 106:1608.

Vrba, F. J., Rydgren, A. E., Chugainov, P. F., Shakovskaia, N. I., and Weaver, W. B. (1989). Additional UBVRI Photometric Searches for Periodic Light Variability from T Tauri Stars. *AJ*, 97:483.

Vrba, F. J., Rydgren, A. E., Chugainov, P. F., Shakovskaia, N. I., and Zak, D. S. (1986). Further Evidence for Rotational Modulation of the Light from T Tauri Stars. *ApJ*, 306:199.

Welch, D. L. and Stetson, P. B. (1993). Robust Variable Star Detection Techniques Suitable for Automated searches: New Results for NGC 1866. *AJ*, 105:1813.

Werner, M. W., Roellig, T. L., Low, F. J., Rieke, G. H., Rieke, M., Hoffmann, W. F., Young, E., Houck, J. R., Brandl, B., Fazio, G. G., Hora, J. L., Gehrz, R. D., Helou, G., Soifer, B. T., Stauffer, J., Keene, J., Eisenhardt, P., Gallagher, D., Gautier, T. N., Irace, W., Lawrence, C. R., Simmons, L., Van Cleve, J. E., Jura, M., Wright, E. L., and Cruikshank, D. P. (2004). The Spitzer Space Telescope Mission. *ApJS*, 154(1):1–9.

Wolk, S. J., Rice, T. S., and Aspin, C. (2013). Near-infrared Variability among Young Stellar Objects in the Star Formation Region Cygnus OB7. *ApJ*, 773(2):145.

Wootten, A. and Thompson, A. R. (2009). The Atacama Large Millimeter/Submillimeter Array. *IEEE Proceedings*, 97(8):1463–1471.

Wright, E. L., Eisenhardt, P. R. M., Mainzer, A. K., Ressler, M. E., Cutri, R. M., Jarrett, T., Kirkpatrick, J. D., Padgett, D., McMillan, R. S., Skrutskie, M., Stanford, S. A., Cohen, M., Walker, R. G., Mather, J. C., Leisawitz, D., Gautier, Thomas N., I., McLean, I., Benford, D., Lonsdale, C. J., Blain, A., Mendez, B., Irace, W. R., Duval, V., Liu, F., Royer, D., Heinrichsen, I., Howard, J., Shannon, M., Kendall, M., Walsh, A. L., Larsen, M., Cardon, J. G., Schick, S., Schwalm, M., Abid, M., Fabinsky, B., Naes, L., and Tsai, C.-W. (2010). The Wide-field Infrared Survey Explorer (WISE): Mission Description and Initial On-orbit Performance. *AJ*, 140(6):1868–1881.

Appendices

Atlas of the variability properties of young stars and brown dwarfs in Taurus

Supplement to the thesis *Blinking Lights in Taurus: long-term variability of young stars and brown dwarfs*

Afonso Manuel Ribeiro Guerreiro do Brito Do Vale

2021

1 Introduction

Variability of a source is a general term covering a diversity of photometric behaviour with time, like periodic or aperiodic fluctuations, increasing or decreasing drifts in brightness with a return to a median value or even constant increases or decreases in brightness. These phenomena can happen on a variety of timescales from days, weeks to months and years. Historically the identification of the variable stars has been done based on the visual inspection of the images or light curves. Nowadays, this technique is no longer an efficient tool due to the enormous amount of data. We still would like to encourage the reader to admire and appreciate the idea of inspecting and comparing the light curves prepared for the single object. We also show here some behaviour of photometry for each of the sources in our sample on various plots. For obvious reasons, this material could not be presented in such an extended way in the thesis. We, therefore, decided on compiling all the material into the present atlas, which presents all the plots and results which followed from the work done in the master thesis *Blinking lights in Taurus: long-term variability of young stars and brown dwarfs.*

1.1 Catalog Information

The present sample was selected from the work of Esplin et al 2019 (hereforth, ESP19)[1] as it represents a bonafide catalog of 491 verified Young Stellar Objects (YSO) in the Taurus Molecular Clouds (TMC), all with associated spectral types (from the same authors) and most with at least one previous photometric measurement in the Near Infrared (NIR; photometry catalog from the same authors; sources with no previous NIR data , 18/491, are mostly, 15/18, secondaries in multiple systems while the remaining 3 are composed of 1 bright B9 source and 2 M dwarfs with Gaia eDR3 data). 445/491 sources matched with Gaia early Data Release 3 (eDR3; Gaia Collaboration 2021). 116/491 sources matched with the General Catalog of Variable Stars 5.1 (GCVS; Samus' et al 2017). 386/491 sources matched with the Zwicky Transient Facility (ZTF; Bellm et al 2019) Data Release 6 (DR6). Of those 386 sources, 309 have data on both g and r, 342 have data in g and 352 have data in r. 448/491 sources matched with the AllWISE (Cutri et al, 2021) Multi-epoch photometry (MEP) catalog. 448 have data in both W1 and W2 but only 321 have data in all 4 WISE bands (W1, W2, W3, W4). For more information on the catalog of Taurus YSOs please see Section 3.2 in the thesis. For more information on the optical and mid-infrared (MIR) multi-epoch photometry data employed in this work see Chapter 4 of the thesis.

2 Extinction, stellar isochrones

For all the color-magnitude diagrams (CMD) shown in this atlas we always employ the extinction law from Cardelli et al (1989) for $R_V = 3.1$. A larger R_V value causes an increase of the slope of the determined extinction vector and its physical implications are discussed in Section 6.1 of the thesis, under "Variable Extinction". The value for the A_V parameter is different depending on the specific plot and source, but is explicitly shown in all plots

---

[1] See Section 3.2 of the thesis

presenting an extinction vector.

For the reader to get a sense of the impact that the observed variability can have on the determination of astrophysical parameters from models, we plot stellar isochrones along with the CMD position changes over time, for each source. The evolutionary tracks shown in the plots contained in this atlas come from a combination of models from PARSEC (Bressan et al, 2012) ($1M_\odot < M_*$), BT-Settl (Allard et al, 2011) ($1M_\odot > M_* > 0.1M_\odot$) and AMES-Dusty (Allard et al, 2001) ($M_* < 0.1M_\odot$) for an age of 3Myr and a distance of 140pc. We simply stitched the tracks at certain mass values since we only use them for visualisation without getting mass or extinction based on them.

3 Additional information

Whenever we refer to a linear regression result we always employ the scypy.odr routine (Boggs et al, 1989), which is a least squares regression method, taking into account errors on both axis. We provide the full catalogs with source information and the results of both the optical and MIR variability analysis for further clarity. These catalogs can be found in the following GitHub location and show, among other information (see GitHub repository for complete information, after publication), references for the coordinates or the NIR photometry, results for the CMD variability slopes shown in this atlas, YSO classification slopes, etc. The repository will feature this atlas and the catalogs through the following link: `https://github.com/AfonsoDoVale/Taurus-Variability`.

4 Atlas organization

For each source, we created a separate set of 5 pages. Each set is organised in the same way. Each source was numbered from 1 to 491 sorted by ascending Right Ascension. For each set, this identification number is written at the very top of each page in bold. In the case of missing data, we present an empty figure with a note. In the following itemization we describe the information contained in each of the 5 pages that composes the set for each star.

4.1 Page 1

- Top left bold text: source name which can be queried in the SIMBAD database [2]; if there is none this field is empty.
- Top right bold text: optical and MIR variable (var) and non-variable (non-var) classification as explained in section 5.3 of the thesis. If there is not data for a classification in either set, this field reads "no data".
- Top left black text:
  - J2000 coordinates (Right Ascension, Declination) from Gaia eDR3, 2MASS (Skrutskie et al, 2006) or UKIDSS (Lawrence et al, 2007). References for the coordinates for each star are present in all catalogs available in the GitHub repository in the column {rPos}. eDR3, 2MASS and UKIDSS are the keywords which associate the coordinates to the aforementioned references, respectively.

---

[2] `https://simbad.u-strasbg.fr/simbad/`

  - Gaia eDR3 G brightness.
  - NIR photometry from ESP19 (J, H, K). Each star has data in J, H and/or K from either the 2MASS point source catalog, the UKIRT hemisphere survey (Dye et al, 2018), the UKIDSS data release 10, WFCAM photometry from ESP19 and WIRCam photometry from previous work by the same authors (see references in ESP19). References for the origin of the photometry in each band is shown in the columns {r_Jmag, r_Hmag, r_Kmag} present in the catalog "taurus_catalog_w_source_info" in the GitHub. Numbering from 1 to 5 associates the measurement with the references, respectively.
  - median g and r brightnesses calculated from ZTF data
  - median W1 and W2 brightnesses from AllWISE data
  - spectral type from ESP19
  - variable type from GCVS 5.1.

- Middle left blue/red text column: results from each statistical index employed in optical/MIR along with variable (VAR) and non-variable (nVAR) classification for each band (g VAR/nVAR, r VAR/nVAR) as determined from the methodology in section 5.2 of the thesis. These indices are discussed in Chapter 5 of the thesis and use the nomenclature there introduced. From top to bottom after optical/MIR variability: chi-squared, weighted standard deviation, burst amplitude (MEDIAN-MIN) and dip amplitude (MAX-MEDIAN), stetson J and finally the Welch-Stetson I.

- Top right plot: Sky distribution of the Taurus YSOs population (grey dots) on top of a Planck 857GHz dust map (Planck Collaboration, 2016). The position of the source corresponding to the atlas entry is marked as a red cross.

- Bottom left plot: G, (Bp-Rp) CMD of the Taurus YSOs population (grey dots) from Gaia eDR3 photometry. Blue curve is the evolutionary track and the numbering following the curve is mass in solar masses. Blue arrow is the extinction vector. The position of the source corresponding to the atlas entry is marked as a red cross. The average errors multiplied by five has been presented in the lower-left corner. When there is no data we still present the plot but without the red cross.

- Bottom right plot: H, (J-K) CMD of the Taurus YSOs population (grey dots) using the NIR photometry catalog in ESP19. Blue curve is the evolutionary track and the numbering following the curve is mass in solar masses. Blue arrow is the extinction vector. The position of the source corresponding to the atlas entry is marked as a red cross. The average errors multiplied by five has been presented in the lower-left corner. Like in the previous plot, when there is no data we still present the plot but without the red cross.

4.2 Page 2

- Top two plots: ZTF DR6 light curves for g (first from the top) and r (second from the top) bands over the 3 years of data. Error bars are plotted; when not visible they are the size of the data point itself or smaller.

- Middle left plot: g, (g-r) CMD created from the median ZTF apparent brightnesses (grey dots). Blue curve is the evolutionary track and the numbering following the curve is mass in solar masses. The average CMD position of the source corresponding to the atlas entry is marked as a red cross. CMD position changes associated with the first year of ZTF data are plotted as red open circles, with the second year as blue open circles and with the third year as green open circles. In the lower left we plot the mean errors computed from the mean standard deviation values for the ZTF data set.

- Middle right plot: g, (g-r) CMD position changes associated with the ZTF data over the full 3 years with time color coded. Black dashed line represents the results from a linear regression and the text on the plot refers to the CMD variability slope determination (a_{TOTAL}) for the 3 years of data. Blue arrow is the extinction vector.

- Bottom plots: g, (g-r) CMD position changes associated with each year of ZTF data, from the first year on the left, to the third year on the right. CMD variability slope determinations ($a_{I/II/III}$) in each plot refer to data from that specific year only. Blue arrow is the extinction vector.

4.3 Page 3

- Top to bottom plots: AllWISE light curves. The vertical cut in the plot separates the pre-cryo data from the post-cryo phase. Triangles refer to measurements with no associated uncertainty. From top to bottom, W1, W2, W3 and W4.

4.4 Page 4

- Top left plot: W1, (W1-W2) CMD created from the average AllWISE apparent brightnesses (grey dots). Blue curve is the evolutionary track and the blue arrow is the extinction vector. The average CMD position of the source corresponding to the atlas entry is marked as a red cross. CMD position changes associated with the pre-cryo data are plotted as blue open circles while post-cryo data are plotted as red open circles. In the lower left we plot the mean errors computed from the mean standard deviation values for both the pre-cryo and post-cryo AllWISE data sets.

- Top right plot: W1, (W1-W2) CMD position changes associated with the full AllWISE data with time color coded. Black dashed line represents the results from a linear regression and the text on the plot refers to the CMD variability slope determination (a_{TOTAL}) for the full data.

- Bottom plots: W1, (W1-W2) CMD position changes associated with the pre-cryo data (bottom left) and post-cryo data (bottom right) with time color coded. Each CMD has the linear regression results for that specific data set ($a_{I/II}$).

4.5 Page 5

- Top plot: Linear regression results of α_{WISE}, the YSO classification slope, in the spectral energy distribution of the source, for all epochs in which there is data with associated uncertainties in W1, W2, W3 and W4. Data for the different epochs is plotted in different colors and have error bars (when they are not visible the error is of the size of the data point or smaller). Colored dashed lines are the results from the different fits. Text in blue corresponds to the mean YSO classification slope determined from all available epochs and also the range of the YSO classification slope determined from the amplitude of all slope calculations. For more information on the YSO classification slope determination methodology see Section 6.4 of the thesis.

- Bottom plot: YSO classification slopes in all available epochs (colored dashed lines in top plot) as a function of time; error bars are plotted and when not visible are the size of the data point or smaller. Red horizontal lines mark the different classes. From top to bottom: Class I (I), Flat Spectrum (FS), Thick Disk (TD), Anaemic Disk (AD) and Naked Photosphere or Class III (NP). The vertical cut in the plot separates the pre-cryo data from the post-cryo AllWISE data.

References[3]

Allard et al (2001). The Limiting Effects of Dust in Brown Dwarf Model Atmospheres. *ApJ*, 556(1):357–372.

Allard et al (2011). Model Atmospheres From Very Low Mass Stars to Brown Dwarfs. In Johns-Krull, C., Browning, M. K., and West, A. A., editors, *16th Cambridge Workshop on Cool Stars, Stellar Systems, and the Sun*, volume 448 of *Astronomical Society of the Pacific Conference Series*, page 91.

Bellm et al (2019). The Zwicky Transient Facility: System Overview, Performance, and First Results. *PASP*, 131(995):018002.

Boggs et al (1989). Orthogonal distance regression.

Bressan et al (2012). PARSEC: stellar tracks and isochrones with the PAdova and TRieste Stellar Evolution Code. *MNRAS*, 427(1):127–145.

Cardelli et al (1989). The Relationship between Infrared, Optical, and Ultraviolet Extinction. *ApJ*, 345:245.

Cutri et al (2021). VizieR Online Data Catalog: AllWISE Data Release (Cutri+ 2013). *VizieR Online Data Catalog*, page II/328.

Dye et al (2018). The UKIRT Hemisphere Survey: definition and J-band data release. *MNRAS*, 473(4):5113–5125.

Esplin et al (2019). A Survey for New Members of Taurus from Stellar to Planetary Masses. *AJ*, 158(2):54.

Gaia Collaboration (2021). Gaia Early Data Release 3. Summary of the contents and survey properties. *A&A*, 649:A1.

---

[3] References are in APA style but have been truncated to "first author et al" format to reduce length of bibliography.

Lawrence et al (2007). The UKIRT Infrared Deep Sky Survey (UKIDSS). *MNRAS*, 379(4):1599–1617.

Planck Collaboration (2016). Planck 2015 results. XI. CMB power spectra, likelihoods, and robustness of parameters. *AAP*, 594:A11.

Samus' et al (2017). General catalogue of variable stars: Version GCVS 5.1. *Astronomy Reports*, 61(1):80–88.

Skrutskie et al (2006). The Two Micron All Sky Survey (2MASS). 131:1163–1183.